TOR VERGATA UNIVERSITY, ROME, ITALY

CIVIL AND COMPUTER ENGINEERING DEPT.

GEOINFORMATION PHD PROGRAMME

CYCLE XXIII

ACTIVE AND PASSIVE REMOTE SENSING TECHNIQUES AND ARTIFICIAL NEURAL NETWORKS IN SUPPORT OF BUILDINGS SEISMIC VULNERABILITY ASSESSMENT

MENTORS

FABIO DEL FRATE, PHD
FLAVIO BORFECCHIA (ENEA)

CANDIDATE

ALESSANDRO LUGARI

To Stefania, Camilla, Lorenzo

‟ولبلــــــدي لــي شـرف هو ما فــي جهلـي قبــل المتواضـــــع أنـا ولكــن ،المطلقـــة الحقيقـــــة أعرف لا أنـا‟
‟مكافــأة

"I don't know the absolute truth, but I am humble in front of my ignorance: these are my honor and my reward"

Kahlil Gibran
جــبران خليــل جــبران

Table of Contents

List of figures

List of Tables

Abstract

The extensive vulnerability assessment of the urban settlements is strictly required in many Italian regions where, despite the relevant seismic risk, the percentage of existent buildings designed without seismic prescriptions is higher than 50%. In this thesis are described the methodologies implemented for evaluating the geometrical and typological parameters of buildings in selected areas of Avellino (a seismic municipality in Southern Italy), using different data remotely acquired by means of aerospatial platforms in order to support a suitably extensive estimation of seismic vulnerability at urban level, with the goal of **creating a Vulnerability Index Map** of the built-up urban environment.

The activities have been based on integration of digital photogrammetry and laser ranging (LIDAR) techniques devoted to 3-D reconstruction (containing buildings geometrical parameters) of selected test areas. In this framework, data acquired by LIDAR sensor have allowed to obtain both the ground Digital Elevation Model and the buildings heights and shape over entire administrative area of municipality.

These results were integrated with those derived from multi/hyperspectral techniques to achieve information about the structural typology of each building in the test areas by means of "data mining" approaches.

In particular here the structural types of buildings have been estimated with good accuracy using information, coming from the different techniques, has allowed to produce, for each building within the test areas, useful information in terms of geometrical and typological parameters to be used for their extensive vulnerability assessment purpose configured Artificial Neural Network.

In such a way the integrated use of various information, coming from the different techniques, has allowed to produce, for each building within the test areas, useful information in terms of geometrical and typological parameters to be used for their extensive vulnerability assessment.

Introduction

Italy is one of the Mediterranean countries mainly susceptible to the seismic risk. In the last 2500 years, in fact, over 30.000 seismic events of intensity equal or higher to Mercalli IV-V degree have occurred in our Country. Although all the national territory has been interested by significant quakes, except the Sardinia island, the highest values of seismic strength have been recorded along the Apennine ridge. In the southern Apennines, the area including Irpinia and Benevento province represents the most stroked zone, with seismic high energy events (Magnitude between 6.5 and 7 Richter), occurred many times during the last centuries.

The consequences of a strong earthquake on the human, social, economic, cultural and historical tissue of the beaten area is enormous: in fact, besides an high number of casualties, in many cases it deeply damages the historical-cultural heritage and the economic-social structures. In Italy, the ratio between the damages produced by earthquakes and the energy released during the events is much higher compared with that of other countries subjected to relevant seismic activity, i.e. California (USA) or Japan.

As an example, the 1997 earthquake in Umbria and Marche Regions has produced severe damages (homeless: 32000; economic damage: approximately 10 billions of Euro), similar to the 1989 California one (14,5 billions of US$), but characterized by an approximately 30 timeslower energy than 1989 event.

This arise mainly from an elevated settlement density and from the remarkable fragility of our real estate patrimony. A study produced by the Italian National Seismic Service has evidenced that more than 10% of the buildings patrimony of 64% of the Italian municipalities is potentially subject to an elevated vulnerability. Over the next 100 years, in 31% of the Italian municipalities at least 10% of the edifices could made out of use after a seismic event. A rough evaluation gauges that there could be approximately 800 casualties/year and beyond 1 billion of Euros the direct damages deriving from probably earthquakes in Italy.

In this context the assessment of the vulnerability of the built-up patrimony is a problem in evidence for the most Italian territory, on which the percentage of rooms in buildings designed and realized in absence of anti-seismic prescription exceeds largely the 50%. Therefore it turns out very important to implement effective

instruments for extensive, timely and repetitive analysis of the existing urbanized areas in order to gain for each building its more meaningful geometric/typological parameters, which - joined to those of soils - allow effective estimation of vulnerability.

Such information can be used to improve prevention and mitigation methodologies, in order to efficiently support the planning policies and post-event management tasks.

ENEA was a partner, toghether with the Naples *Federico II* University and the Consorzio T.R.E., of the **TELLUS Stabilita Project**, funded by the Italian Ministry of Instruction, University and Reseach, in which technologies were tested and methodologies were developed in order to protect the built-up urban environment from earthquakes.

The activities carried out in this work ere indeed totally integrated in such a project, which lasted three years, from January 2007 to December 2009.

The study area: Avellino

In this work is described a study conducted in the area of the Municipality of Avellino (Fig. 1), in the Campania region, Italy.

Avellino (40°54′55″N 14°47′23″E, 348m m.s.l., 42Km NE of Naples, Total population: 56.700 in 2001, according with the Italian Statistics Insitute) is situated in a plain called "Conca di Avellino" and surrounded by mountains: Massiccio del Partenio (Monti di Avella, Montevergine e Pizzo d'Alvano) on NO and Monti Picentini on SE. Due to the Highway A16 and to other major roads, Avellino also represents an important hub on the road from Salerno to Benevento and from Naples. Consequently to the 1980 earthquake and trying to regulate the reconstruction activities, several specific acts, decrees, zoning laws and ordinance have been issued: the first one was the n. 219/1981 Act, that entrusted the coordination of the activities to the Campania Region and the urban planning to the damaged Municipalities.

From 2006 the urban planning issues of Avellino and neighbour areas are regulated by two instruments: P.I.C.A. (Italian acronym that stands for Integrated Project for Avellino City) and P.U.C. (Urban Plan for Avellino Municipality).
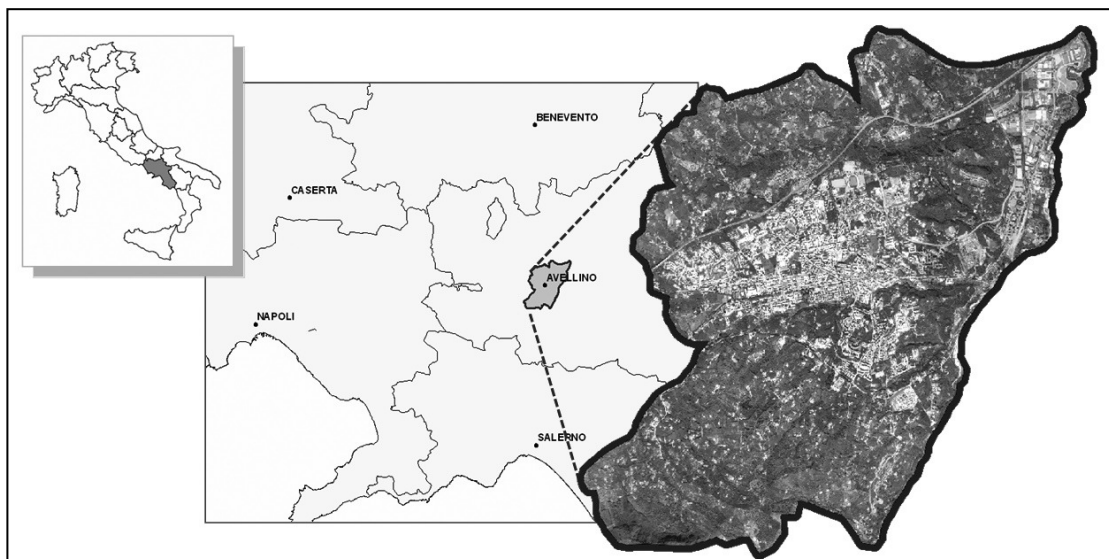
Figure 1 - Geographic location of the study area: Municipality of Avellino, Southern Italy.

Chapter 1 Technologies, Instruments and Data

In this work many technologies and methodologies were tested against the project needs: amongst them active remote rensing (LIDAR), as well as passive (Multispectral, Hyperspectral, High Resolution Panchromatic), Spectral Mixture Analysis and Artificial Neural Networks.

A very huge amount of data was actually gathered in the framework of the TELLUS Stabilita Project, as we will show later in this chapter.

Three technologies, one methodology, two instruments and a software in particular are taken into account and described in this chapter:

- LIght Detection And Ranging (LIDAR)
- Hyperspectral remote sensing
- Artificial Neural Networks (ANN)
- Spectral Mixture Analysis (SMA)
- LIDAR sensor (Optech ALTM3100),
- Hyperpectral sensor (AISA Eagle), both of them airborne, and
- Data mining suite (Tiberius)

1.1 Light Detection and Ranging (LIDAR)

The acronym LIDAR stands for Light Detection and Ranging. Light Detection and Ranging basically consists of a laser rangefinder that operates in some form of airborne platform (helicopter, plane, or satellite).

The rangefinder takes repeated measurements of the distance from the platform to the ground. The position and elevation of the platform is precisely known by way of airborne GPS along with ground control, so the elevation of the ground surface can be calculated by subtracting the laser rangefinder distance from the height of the platform.

Compensation must be made for the tilt and pitch of the airborne platform by way of gyroscopes and accelerometers in the aircraft's inertial measurement unit.

Lidar systems record thousands of highly accurate distance measurements every second (newer systems operate at frequencies up to 150 kHz; older systems 30-80 kHz) and create a very dense coverage of elevations over a wide area in a short amount of time.

Because lidar is an active sensor that supplies its own light source, it can be used at night and, thus, avoid routine air traffic, or it can be flown under some types of high cloud conditions.

Most lidar systems record multiple surface reflections, or "returns," from a single laser pulse. When a laser pulse encounters vegetation, power lines, or buildings, multiple returns can be recorded.

The first return will represent the elevation near the top of the object. The second and third returns may represent trunks and branches within a tree, or understory vegetation.

Hopefully, the last return recorded by the sensor will be the remaining laser energy reflected off the ground surface, though at times, the tree will block all the energy from reaching the ground.

These multiple returns can be used to determine the height of trees or power lines, or give indications of forest structure (crown height, understory density, etc.).

Figure 2 shows an example of first return lidar points.
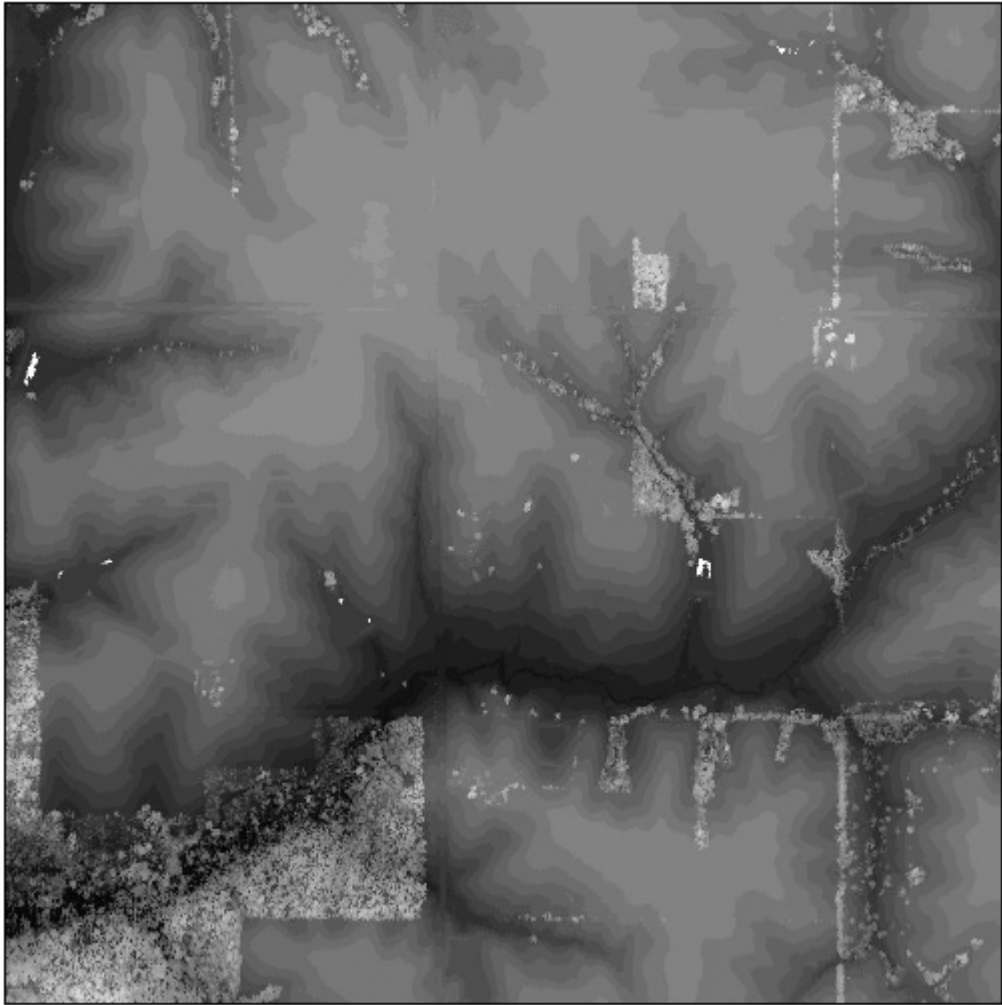
Figure 2. An example of first return lidar data

Another feature of an airborne lidar system is the use of mirrors or other technology to point the laser beam to either side of the aircraft as it moves along its path.

Depending on the scanning mechanism, the lidar scans can have a side-to-side, zigzag, sinusoidal, or wavy pattern. While the laser itself pulses many thousands of times per second, the scanning mechanism usually moves from side-to-side at around 20-40 cycles per second.

This scanning, combined with the forward motion of the aircraft, produces millions of elevations in a short distance and time. The field of view or angle the scan makes from side-to-side can be adjusted by the operator, but is usually set at 30 to 40 degrees. This creates a swath of around 1 kilometer wide or less.

Adjacent swaths overlap from 15 to 30% so that no data gaps are left between flight lines. The spacing of lidar points on the ground, called "postings," is a function of the laser pulse frequency, scan frequency, and flight height (Baltsavias, 1999).

While there is usually a nominal posting spacing specified in a lidar project, actual data points have variable spacing that are smaller and larger than the specified spacing.

Mappers need to be aware of these effects when viewing final products that were derived from the raw data. The second aspect is that, because the laser scans from side to side, it interacts with the ground in different ways, depending on the angle of incidence.

Lidar pulses at the edge of a scan will strike the sides of buildings, whereas pulses at the center of a scan will only strike the roof tops. Likewise, pulses at the edges of scans will pass through trees at an angle.

Sometimes this will create "shadows" on the other side where no lidar passes through. n addition, less energy will return to the lidar receiver as it reflects away from the aircraft.

This is evident in the intensity images created from the intensity values for each return: one can see overall darkening of the intensity at the edges of swaths. Edges of swaths appear darker than the returns at centers of swaths.

Typically a lidar system collect a first and last return from each lidar pulse. From the first and last returns, a so-called "bare earth" return is created using classification algorithms.

These classification systems try to sort out non-bare earth returns (tree tops, buildings, power lines, automobiles) from bare earth returns. To distinguish bare earth in forested areas, differences in elevation between the first and last returns, relative changes in elevation, and slope were used. Intensity data were used to identify vegetation and man-made materials.

Sometimes there are some data voids in forested areas due to non-penetration of the laser through tree canopy, but these areas are generally easily filled in by interpolation.

Leaf-on conditions and tall crops, such as corn, do not allow easy penetration of the laser beam to the ground and should be avoided.

Lidar data are supplied by the vendor in ASC text format, consisting of n x n kilometer tiles with x and y coordinates, z elevations, and intensity values. As an example, with a nominal 1 meter posting spacing, some tiles had up to 3.3 million points.

Postings near the center of the flight lines are close to the nominal 1 meter spacing (Figure 3a), while toward the ends of scans, the points converge with the start of the

next scan (Figure 3b).
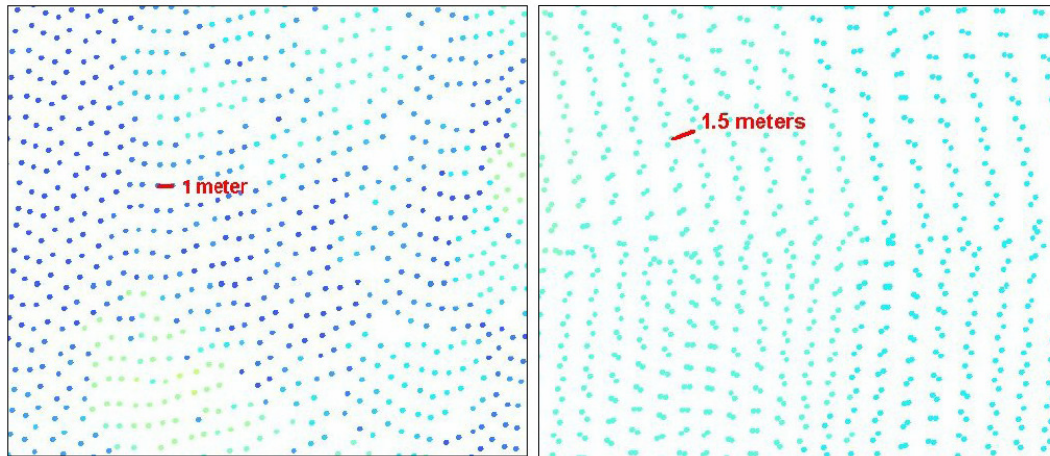
Figure 3, a and b. LIDAR data spacing

While some scans converge, others diverge. Where the scans converge, the points can be less than half of the nominal spacing, and likewise, where they diverge,

they can be twice the nominal spacing.

Because some points can be as close as 0.5 meters, the tiles are initially interpolated to create grids with 0.5 meter resolution, with the idea that no data points should be merged or averaged with any other points.

In this work we desired to create the grids as close as possible to the native resolution of the lidar data to evaluate their full potential to represent the smallest surface features.

1.1.1 The Optech LIDAR

The sensor used in this work is built from Optech Inc., Toronto, Canada.

The model name is ALTM 3100 (Figure 4); such a device is able to handle the laser multi-returns from semitransparent tree canopies, thus allowing a more reliable estimates also in urbanised areas where the buildings shape is partially occluded by trees or vegetation (Figure 5 and 6):

THE HELIOGS SYSTEM

The system that OGS operates (OPTECH 3100) is mounted on board of a helicopter (AS350 B2)

The system operates a solid state NdYAG laser (1064nm) with a mean reference power of 6.5 W and a frequency of 33.000/100.000 pulses per second

The operating range (elevation above ground level) varies from a minimum of 80 m (wide beam) to a maximum of 3200 m

Figure 4. The Optech ALTM3100 system

THE LASER SCAN SYSTEM

Optech's ALTM 3100 is able to record 1st, 2nd, 3rd, and the last laser returns, including intensity values. Data are acquired at 33, 50, 70 and 100 kHz.

First Returns

Second Returns

Third Returns

Last Returns

All Returns
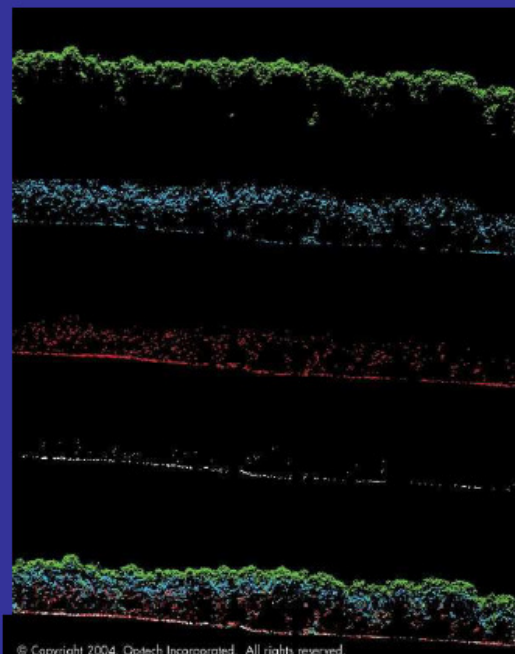
Figure 5. The scan system
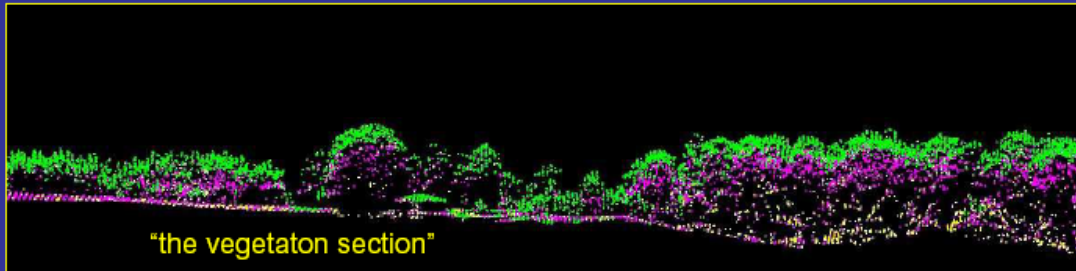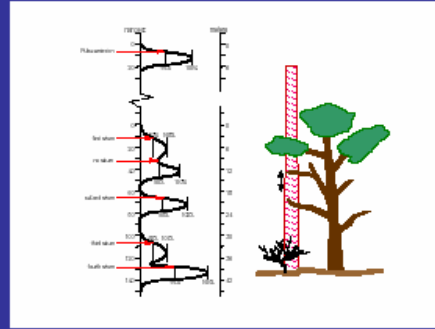
Figure 6. LIDAR Canopy penetration

In figure 7 are shown the main technical features of ALTM3100 versus other Hw sensors:

SYSTEM	ALTM 3100	ALTM 3033	ALTM 1020	TopoSys	TopoEye I
Manufacturer	**Optech**	**Optech**	**Optech**	**TopoSys**	**Saab**
Country	*Canada*	*Canada*	*Canada*	*Germany*	*Sweden*
Reflectance	Si	Si	No	No	Si
Wave lenght	1064	1064	1047 nm	1535 nm	1064 nm
Scan type	Pulse	Pulse	Pulse	Pulse	Pulse
Flight height	80-3500	265-3000	1000 m	850 m	500 m
Aircraft speed	-	-	-	70 m/s	10-25 m/s
Pulse repetition rate	33-100 Khz	33 Khz	5000 Hz	8000 Hz	6000 Hz
Scan frequency	up to 70 Hz	up to 70 Hz	50 Hz	630 Hz	650Hz
FOV	Up to 25°	Up to 20°	Up to 20°	7°	Up to 10°
Swath	up to 0.93 H	Up to 700 m	Up to 700 m	230 m	Up to 168 m
Operated on	Helicopter	Helicopter	Aircraft	Aircraft	Helicopter

Figure 7. Optech ALTM3100 Technical specifications

1.2 Hyperspectral Imagery (HSI)

1.2.1 Imaging Spectroscopy

Imaging spectroscopy is the science and art of applying the techniques of spectral analysis to a set of contiguous pixels. This set of contiguous pixels is, of course, an image. The image has been captured by a sensor, termed an imaging spectrometer, that records tens or hundreds of bands simultaneously. Each of these bands has a very small bandwidth, typically 10-20 nanometers, and is spaced such that there is a slight overlap between bands.

An example of overlap can be seen in data from the NASA/JPL Airborne Visible/Infrared Imaging Spectrometer (AVIRIS) sensor, which is shown in Figure 8 (Green 1995).
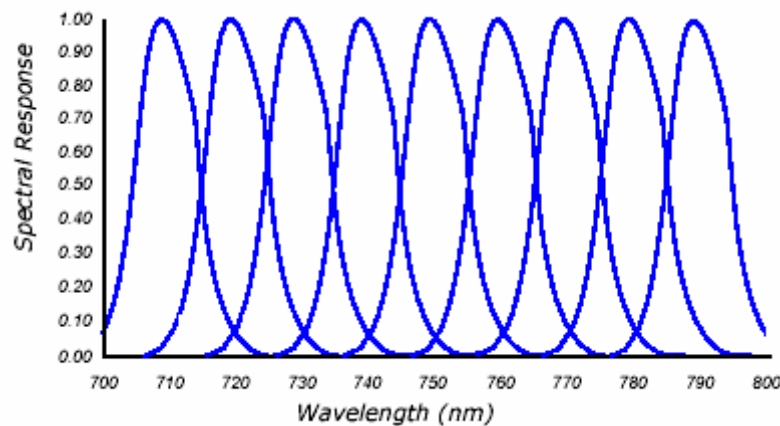
Figure 8: Spectral Response of AVIRIS Channels

Because these bands are narrow and overlapping, the data from a single pixel can be plotted to form a continuous spectral plot or profile. An example, again from AVIRIS, is shown in Figure 9. Note the parameters plotted on the X and Y axes. The X axis is the wavelength of the center of the (narrow) band. The Y axis is a physical parameter of the material(s) imaged, which is termed the reflectance.
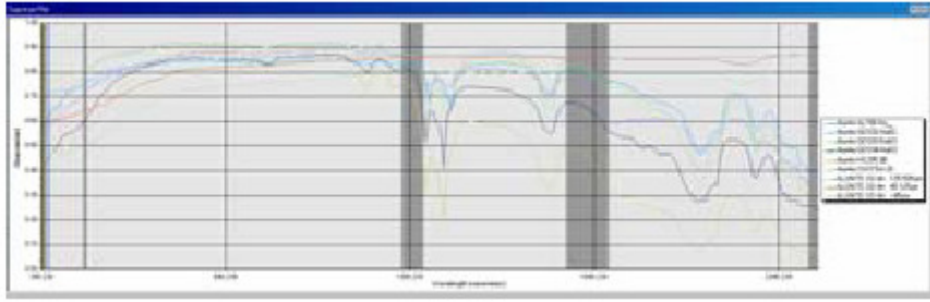
Figure 9: AVIRIS Data in the Spectrum Plot

It has, of course, always been possible to plot the data from multispectral sensors. Figure 10 shows a plot of data from the Landsat TM sensor.
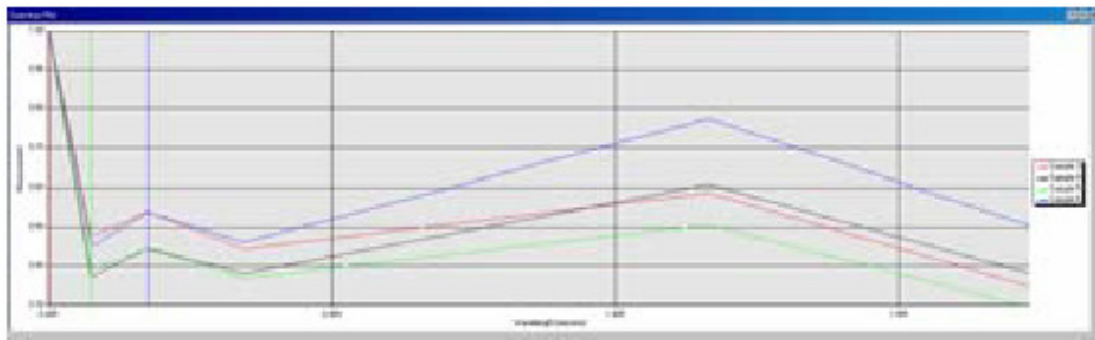
Figure 10: Landsat TM Data in the Spectrum Plot

This plot suffers from several inherent limitations.

• The X-axis shows the band number. This is a fairly meaningless designation: band 1 of the Multispectral Scanner (MSS) is different from band 1 of the Thematic Mapper (TM) sensor, and both are different from band 1 of Advanced Very High Resolution Radiometer (AVHRR) or SPOT XS sensors. There is no way to intercompare datasets using this axis designation.

• The Y-axis, digital number or DN value, is similarly meaningless. The magnitude of this value is a function of not only the particular sensor but also the time of day, day of year, cloud cover, etc. Again, we cannot intercompare datasets using this axis designation.

• Across the top of the plot in Figure 11 is the bandpass of each band. This is the range of frequencies whose intensity is measured and combined to form each band of the sensor. In comparing the bandpass widths with the width of the absorption features seen in Figure 11, it is obvious that the TM and similar sensors cannot resolve the difference between the materials as well as those seen in Figure 9.
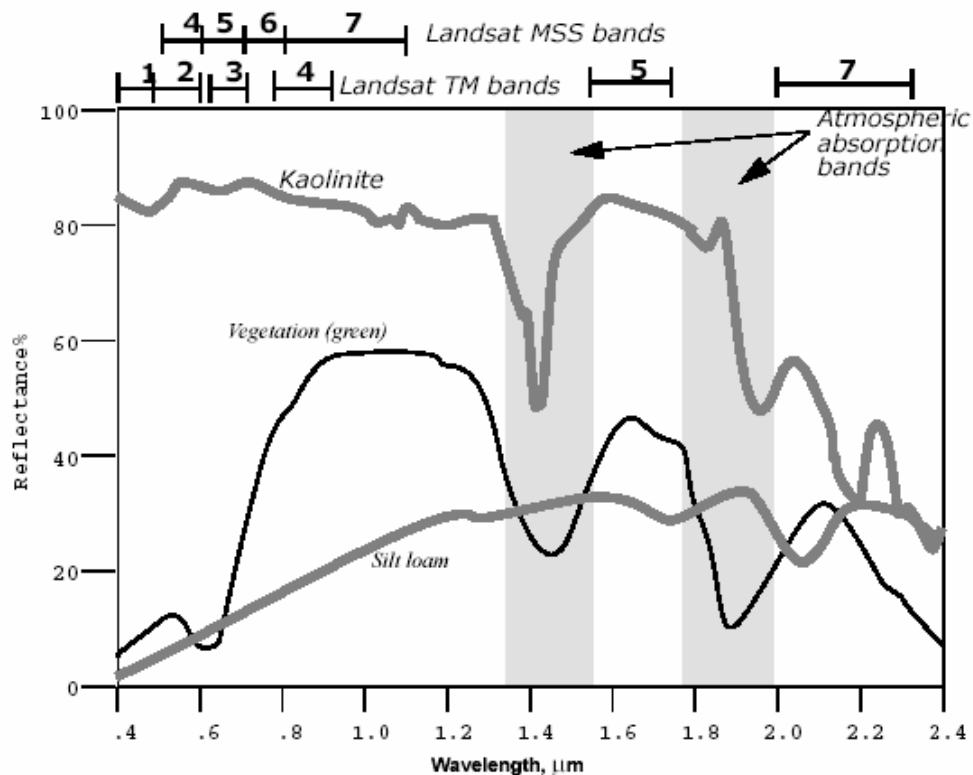
Figure 11: Reflectance Spectra

This is not to say that attempts were not made to resolve the difference between materials. Indeed, the reason that band 7 falls between bands 5 and 6 on the wavelength scale is because band 7 was added late in the TM sensor design due to the interest of geologists in that spectral region.

Similarly, the band ratios developed for quantifying various materials (TM4/TM3 for vegetation; TM5/TM7 for clay minerals) were based on the spectral shapes of the materials of interest.

However, there was a large disconnect. The broad-band sensors were collecting 10 or fewer bands while the standards being measured in the laboratory were based on hundreds of bands.

With the advent of the imaging spectrometers, it became possible to bring together, even intercompare, data from the remote sensor and the laboratory spectrometer. Imaging spectrometers also allowed intercomparison of data from different remote sensors. While the narrow bandpass characteristics of the imaging spectrometers allowed precise intercomparisons on the X-axis (frequency), the Y-axis (intensity) proved more complicated.

24

In the laboratory setting, the absorption spectrum of a material of interest is taken under tightly controlled conditions. The sample chamber, radiation source, and diffraction grating area are all flushed with dry nitrogen to remove the effects of the ambient air— particularly water vapor and carbon dioxide. A null, or empty, channel is measured simultaneously. The instrument is calibrated prior to each measurement. Under such controlled conditions, the measured intensities can be accurately converted to primary physical properties such as percent transmission, absorbance, or reflectance. Conversion to one of these physical parameters allows intercomparison of results taken on different days or in different laboratories.

Results can be compiled for universal use.

With data from the remote sensor, correction of the sensor signal to a primary physical property has proven difficult. The first step, conversion of the raw DN value to at-sensor radiance, can be accomplished using the calibration coefficients of the sensor. This step is commonly performed before the data is distributed.

Alternatively, the sensor calibration coefficients are available from the data source. At-sensor radiance, however, is affected by the factors such as: time of day and day of year (which control solar illumination), cloud cover (which causes local attenuation), and the overall content of the atmosphere. Incoming solar illumination can be modeled given knowledge of the date and time of data collection.

The other parameters are more difficult to model.

The radiation received by the remote sensor has passed through the atmosphere twice. The situation for an airborne sensor is different than for a spaceborne one. An airborne sensor is below the ozone layer, may be below the stratospheric clouds, or could be below the cumulus clouds. The components of the atmosphere have had ample opportunity to absorb and/or scatter the solar radiation. The complexity arises because the composition of the atmosphere varies seasonally (winter vs. summer), regionally (maritime vs. continental), and locally (Gao et al. 1993). Correcting (removing) these atmospheric effects from each scene is required to reduce the scene to the physical parameter reflectance. Only then can different images or images and laboratory spectra be intercompared. This requirement, Atmospheric Correction, is currently a bottleneck in imaging spectroscopy.

1.2.2 Atmospheric Correction

The goal of Atmospheric Correction is to completely remove the absorption and scattering effects of the Earth's atmosphere to allow conversion of the image data to a

primary physical parameter: reflectance. The approaches to this fall into two categories: atmospheric modeling and empirical.

1.2.2.1 Atmospheric Modeling

The atmospheric modeling approaches attempt to quantify the exact atmospheric composition at the time of data acquisition and then calculate the probable effects. These models, termed atmospheric transmission codes, have met with considerable success.

For example, the United States Air Force Geophysics Laboratory has steadily evolved its code from LOWTRAN (Low Resolution Atmospheric Transmission Code) through MODTRAN (Moderate Resolution Atmospheric Radiance and Transmittance Model) (Berk 1989) to HITRAN (High Resolution Transmission Molecular Absorption Database). A limiting factor in the use of these codes in their pure form is the requirement of accurate input of the atmospheric composition at the time of data acquisition. Given these inputs, the transmission codes have proven quite accurate in predicting the attenuation effects on the image. With the accuracy of the transmission codes demonstrated, a next step was to investigate ways to estimate the requisite input parameters and evaluate the accuracies attained using these estimates.

Evaluation of transmission code-based Atmospheric Corrections suggests that these corrections may be as good as they can get, given the inevitable variability and uncertainty of the real world. In addition, it is being recognized that (transmission code-based) Atmospheric Correction is appropriately the responsibility of the data vendor. Additionally, imagery from airborne hyperspectral sensors is less easily addressed by the transmission codes due to variations in the altitude of flight for each data acquisition.

There have been a number of correction algorithms based on the transmission codes. These algorithms attempt to estimate some of the requisite parameters either from the data itself or through interaction with the analyst. The ATmosphere REMoval program (ATREM) was developed by the Center for the Study of Earth from Space (CSES) at the University of Colorado for use with AVIRIS imagery (Gao et al. 1996). ATmospheric CORrection (ATCOR) was developed by the German Space Agency (DLR) in conjunction with ERDAS in Germany (Richter 1996). Atmospheric CORrection Now (ACORN) was developed by ImSpec, LLC using MODTRAN 4. Fast Line-of-sight Atmospheric Analysis of Spectral Hypercubes (FLAASH) was developed in part by the Air Force Geophysics Laboratory (Alder-Golden et al. 1998).

Regardless of whether the model-based correction is done by the data vendor or subsequently, given real-world variability and uncertainty, it can never be perfect. It has been clearly and eloquently shown by Roger Clark (USGS, Denver) and others that minor adjustments using ground control, applied after transmission code-based Atmospheric Correction, enable superior results.

1.2.2.2 Empirical

A second category of approaches to Atmospheric Correction is those based on ground truth inputs. These algorithms rely on the use of one or more spectral control points. A spectral control point is a pixel (or collection of pixels), identifiable in the image, for which the analyst has a library spectrum of that pixel's material composition without atmospheric effects.

The best way to get such spectral control points is to collect them in the field with a handheld field spectrometer. Alternately, the analyst may have a Spectrum Library from which an approximate spectrum can be selected if the material in the pixel is known. When the spectral control point(s) are identified, they can then be used to correct the entire image. Again, some assumptions are being made.

Several problems present themselves. Every pixel is a mixed pixel at some level and, due to sensor trade-offs (largely data volume), hyperspectral pixels tend to be relatively large: commonly 10-30 meters. At this scale, it is difficult to find pure pixels, especially of naturally occurring materials. This suggests that human-made features such as parking lots, building roofs, or golf courses should be used.

Another assumption is that the material from which the control spectrum is taken is identical to the material being imaged in the pixel. Natural materials are incredibly variable. This can greatly limit the applicability of the compiled Spectrum Libraries and also contributes to the development of specialized libraries, such as SPECMIN from Spectral International, Inc.

Once the issue of defining the spectral control points has been addressed, several similar algorithms exist.

An approach has been proposed for instances in which the analyst has absolutely no auxiliary information. This is the IARR algorithm.

This algorithm requires several major assumptions and is therefore limited to cases where those assumptions strictly apply. Use of this approach where those assumptions do not apply can lead to very erroneous results. major assumption underlying many of the imaging spectroscopy algorithms is that of linear mixing.

1.2.2.3 Linear Mixing

A major assumption underlying many of the imaging spectroscopy algorithms is that of linear mixing. This assumption postulates that the brightness (DN at each wavelength) of an image pixel is a linear combination of the percentage of each endmember and the brightness of a pure sample of that endmember or, mathematically:

$$DN_b = \sum f_n EM_{nb}$$

(Source: Adams et al. 1986)

This assumption is, perhaps, analogous to the assumption of Gaussian distribution which underlies many of the traditional classification algorithms such as Maximum Likelihood and Mahalanobis Distance. While it may be of questionable validity, without it progress is difficult.

The linear mixing model is not strictly applicable for a variety of reasons. This is particularly true in the VNIR and SWIR regions. In the TIR region, the linear assumption has been shown to be significantly more valid (Ramsey et al. 1998). Linear mixing assumes that each photon interacts with only one material. However, multiple-scattering effects in the ground environment are possible, even likely. Photon scatter between vegetation and the ground or within the vegetation layer is common. If a photon interacts with more than one material, the process becomes nonlinear (Farrand and Harsanyi 1995).

It has been shown that a system of nonlinear mixing can be linearized (Ramsey and Christensen 1998). This is commonly done by converting the at-sensor radiance to single scattering albedo (Resmini et al. 1996). Shadow introduces nonlinearity (Olsen et al. 1997) and yet shadow is so ubiquitous that it must be included as an endmember within the overall endmember list for most images.

Endmembers are not constant even within a single scene. As the endmember changes within the scene, its spectrum changes. This mismatch between the defined endmember and its actual form on the ground leads to errors within the matching algorithm. It is commonly assumed that the percent contribution of an endmember to the overall radiance of a pixel is a measure of the pixel-fill of that endmember—this is not a proven conclusion (Shipman and Adams 1987). Many analytical metrics assume that the pixel compositions are uncorrelated—this is not a strictly valid assumption.

1.2.3 Endmembers

The use of endmembers in estimating the composition of an image pixel is analogous to their use in constructing ternary (or higher order) diagrams to explain the variable composition of mixed systems. Consider the ternary system *ABC* in Figure 12.
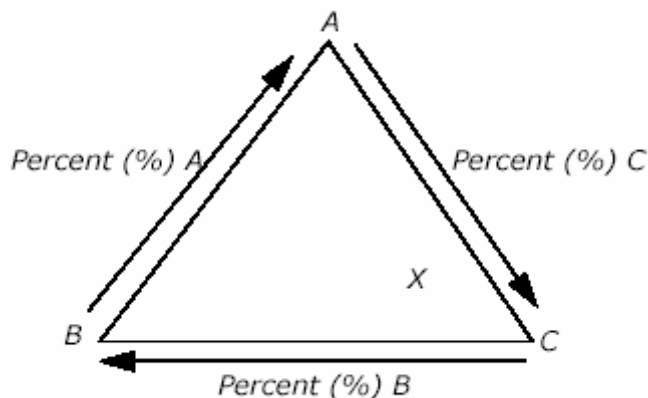
Figure 12: Ternary Model

This theoretical system is composed of three pure materials: *A, B,* and *C.* These are the endmembers of this system. A member of this system composed of 100% material *A* would plot at the apex of this pyramid; a member with 100% *B* would similarly plot at point *B.* Any mixture of these three materials, such as *X,* falls somewhere within the triangle with *%A, %B,* and *%C* determining exactly where. In Figure 12, mixture *X* is 10% endmember *A,* 20% endmember *B,* and 70% endmember *C.*

In imaging spectroscopy, we have a somewhat analogous situation. We have a number of pixels, mixtures (mixed pixels) such as *X* in Figure 12, and we would like to know some or all of the endmembers (*A, B,* and *C*) and the percentage of some or all of the endmembers in each pixel. Clearly, the identity of the endmembers is crucial to this analysis.

Selecting endmembers for natural systems is exceedingly difficult due to the inherent variability in nature. Consider a geologically oriented analysis. In theory, one would like a spectrum of each pure mineral for the endmember spectra. However, pure minerals rarely occur in nature. Cation and /or anion substitutions are common depending on the origin of the sample. Even with identical composition, the spectrum is affected by the degree of crystallinity for each sample.

Particle size distribution affects the exact shape of the absorbance curve. As the particle size decreases, the absorption bands flatten out and tend to merge with the continuum. For this reason, the USGS, Jet Propulsion Laboratories (JPL), and

Advanced Spaceborne Thermal Emission and Reflection Radiometer (ASTER) Spectrum Libraries give spectra of the same mineral at different particle sizes.

Other naturally variable factors such as associated phases and degree of weathering, presence or absence of water, and degree of transparency all affect the resultant spectrum.

A similar list of variables can be compiled for vegetation spectra.

Variables such as rainfall, presence or absence of minerals in the soil, phase of the growing cycle, sun-leaf orientation, etc. cause changes in the recorded spectrum.

In addition to the various endmember species, there is generally a dark endmember that represents the shade/shadow areas within the scene. The shade endmember is nonzero due to atmospheric scattering. This endmember is variable with terrain relief, vegetation type and density, and viewing geometry. As it has a large scattering component, the illumination is shifted toward the blue spectral range.

The central wavelength and relative depth of absorption features are the major diagnostic features in spectral analysis. However, these are not constant for given specie, but vary with a number of factors.

Band shape and depth depend on illumination and viewing geometry, particle size, and even the spectral response functions of the sensor itself. The actual signature measured by the sensor is affected by atmospheric and geometric conditions as well as noise.

Thus, the signature of a uniform material can have significant variation. Atomic substitutions in the lattice of minerals cause changes to the shape and/or position of the spectral bands. This fact is exploited to measure the distribution of cation substitutions in minerals (Roger Clark, USGS).

Because of these variations and distortions, search and detect algorithms that are highly sensitive to the target spectrum (signature) are compromised or even ineffective. Candidate endmembers must be chosen so as to ensure that their distribution is unimodal and well separated from other endmembers. In practice, it is probably best if endmembers are sampled from the dataset under analysis.

The discussion of endmembers has been largely directed toward the idea of an endmember as a single material such as a mineral (chemical compound) or distinct vegetation species. For some systems or analyses, however, a scene endmember might be a combination of singular materials. For example, in the analysis of a littoral scene, one endmember might be beach. The beach endmember could be 80% silica sand, 15% marine carbonates (sea shells), and 5% vegetable material (seaweed and algae).

For another analysis, an airport runway endmember might be defined as 85% cement, 14% tire rubber, and 1% a strong absorption band from spilled aviation fuel. Either of these compound endmembers could be defined by a single spectrum and represent a component of the system.

1.2.4 Spectrum Libraries

Spectral signatures are required for analysis of hyperspectral images. They provide the endmembers, Target Detection, and Material Mapping signatures, and input materials for Material Identification. The spectral signature is the information that is used in classifying a pixel.

Because of this primary role of spectral signatures, efforts have been made over the past decade to compile databases, termed Spectral Libraries, of the spectra of known materials (Clark et al. 1993b).

These libraries include human-made materials, pure minerals, site specific minerals, pure vegetation stands, and various mixed composition spectra. Libraries have been compiled of laboratory signatures taken with spectrometers under tightly controlled conditions, handheld field spectrometers in both natural and controlled areas, and from remote sensing images (scene-derived spectra). Many of these libraries are available to the public or selected researchers.

1.2.5 High Resolution Imagery (HRI)

To supplement the HyperSpectral Imagery (HSI) display, HSI systems usually include a high-resolution (HRI) black-and-white, or panchromatic, camera. This camera is mounted adjacent to the HSI sensor to enable both sensors to capture the same reflected light.

The HRI sensor uses a pushbroom approach just like the HSI camera. It has a similar lens and slit arrangement to limit the incoming light to a thin, wide beam. However, the HRI camera does not have a diffraction grating to disperse the incoming reflected light. Instead, the light is directed to a wider CCD to capture more image data.

Because it captures a single line of the ground image per frame, it is called a line scan camera.

An HRI CCD is usually several thousand pixels wide and one pixel high. It operates at a frame rate that is much faster than that of the HSI sensor—typically several hundred frames per second.

The combination of more imaging pixels (several thousand) and the faster frame rate

(several hundred Hz) results in a finer resolution that is on the order of a few inches per pixel.

This high resolution adds the capability for a human operator to visually evaluate detected objects on the system display.

1.2.6 An application of Hyperspectral Imagery to urban areas

Following the terrorist attacks of September 11, 2001, HSI technology was used to assess the distribution of materials and dust from the World Trade Center (WTC) in New York City. Using spectral signatures for such things as concrete, cement, and gypsum wall board, the dispersion of debris could be tracked using hyperspectral imagery.

An hyperspectral image of the WTC area is shown below in Figure 13. This image was acquired by satellite five days after the attacks.

Figure 13. Analysis of Materials from Destruction of the World Trade Center in New York City, USA

1.2.7 The AISA Hyperspectral sensor

Within this work an airborne hyperspectral sensor owned and operated by Helica Srl, an OGS spin-off firm, was used. This sensor is designed, build and sold by Spectral Imaging Ltd from Oulu, Finland.

His head is coupled with a GPS/INS unit and with an HR CCD camera (fig. 14-18)

Figure 14. The AISA Eagle Sensor Head
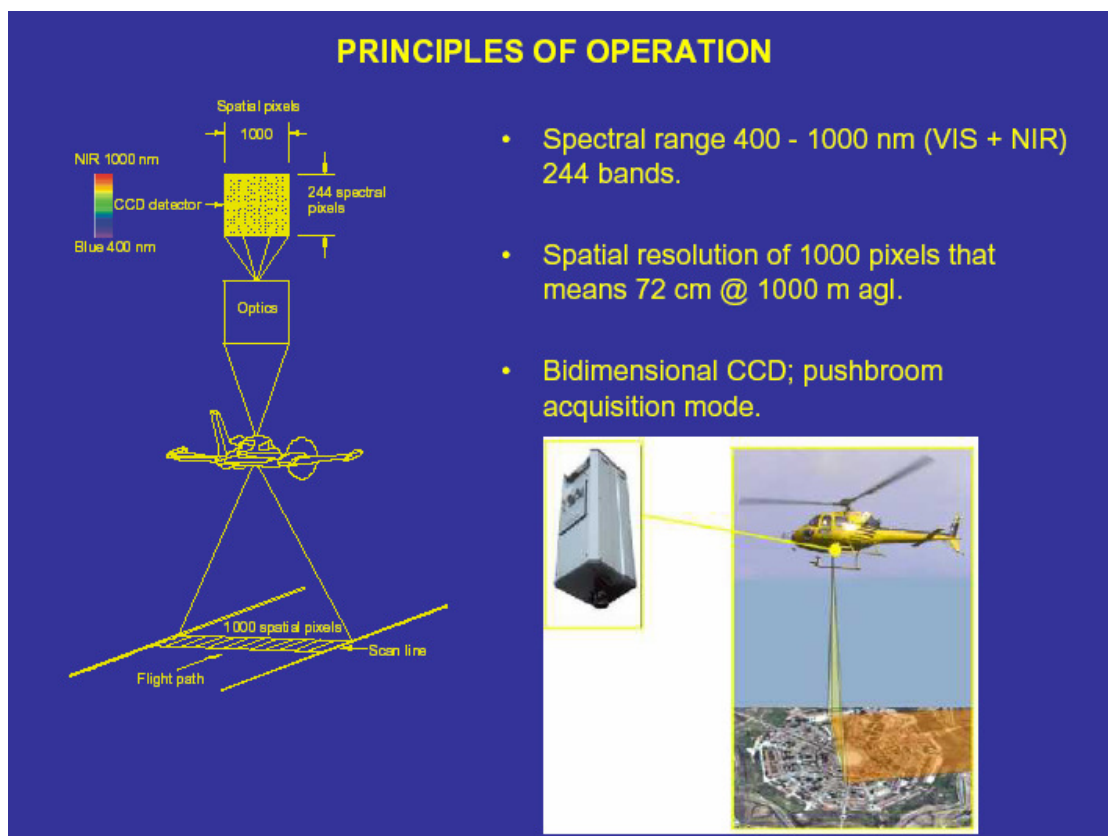
Figure 15. AISA Eagle Operation principles
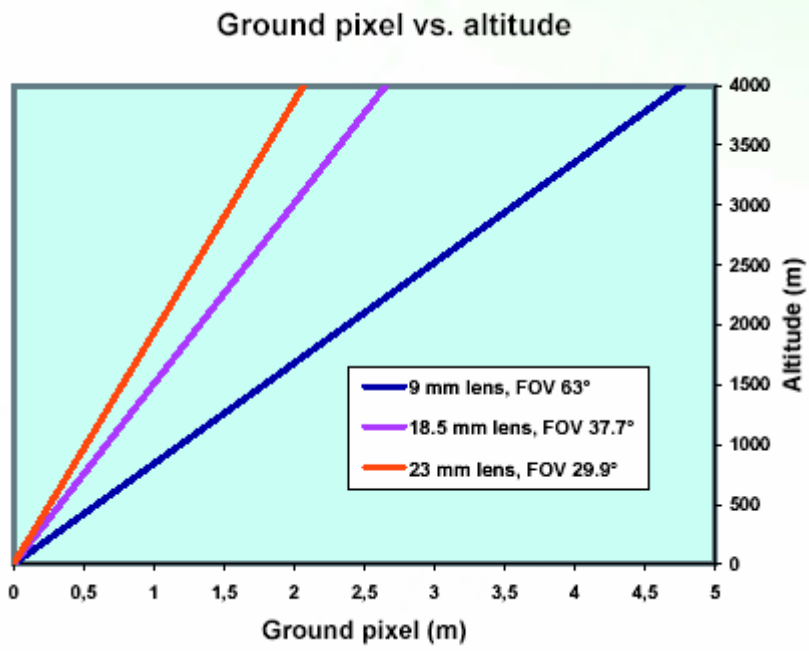
Figure 16: AISA Eagle ground pixel sampling vs flight altitude
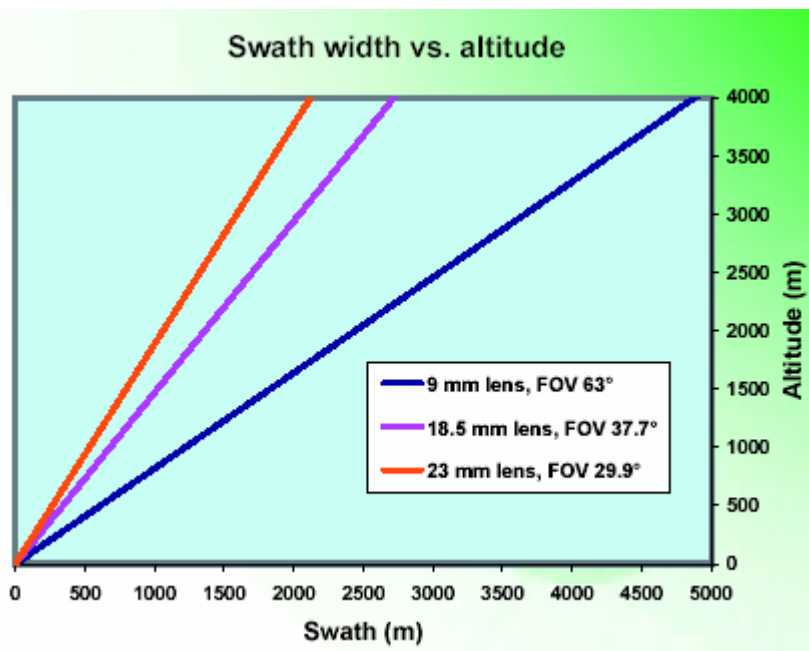
Figure 17. AISA Eagle FOV vs flight altitude

Image rate at aircraft velocity of
60 m/s (120 knots)

9 mm lens, FOV 63°
18.5 mm lens, FOV 37.7°
23 mm lens, FOV 29.9°

Altitude (m)

Image rate for square ground pixel (images/s)
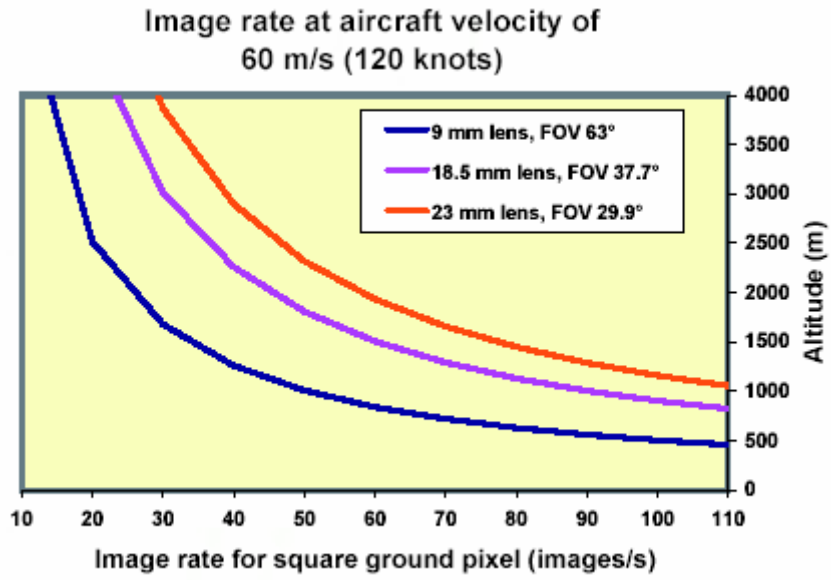
Figure 18. AISA Eagle Image rate vs flight velocity

AISA Eagle is capable to operate within a wide range of customer specifications, as shown in the following figure 19:

Sensor head	Typical specifications				
Spectrograph	High efficiency transmissive imaging spectrograph. Throughput practically independent of polarization. Smile and keystone < 2 microns.				
F/#	F/2.4				
Spectral range	400-970 nm				
Spectral resolution	2.9 nm				
Slit width	30 microns				
Spectral binning options	1x	2x	4x	8x	8x + sw2x
# of spectral bands	488	244	122	60	30
Spectral sampling/band	1,25nm	2,3nm	4.6nm	9,2nm	18,4nm
Image rate, up to	30	40	60	85	100 images/s
Spatial pixels, up to	1024, of which 70 – 80 FODIS pixels (optional)				
Fore optics options					
Focal length	23 mm		18,5 mm		9 mm
FOV	29.9 degrees		36.7 degrees		62,1 degrees
IFOV	0.029 degrees		0.036 degrees		0,060 degrees
Swath width	0.53 x altitude		0.66 x altitude		1.20 x altitude
Ground resolution @ 1000 m altitude	0,52 m		0.65 m		1,2 m
Camera	Progressive scan CCD camera				
Output	12 bits digital				
Integration time	Settable independent of image rate				
Shutter	Electromechanical shutter for dark background registration, user controllable by software.				
FODIS	Diffuse light collector and fiber optic cable (5 m standard) with SMA connector.				
Calibration	Sensor head comes with wavelength and radiometric calibration file.				

Figure. 19 AISA Eagle sensor technical specifications

36

In this work were acquired images with 30 spectral bands at about 1m ground resolution (Fig. 20)

N. band	c−λ (nm)	FWHM
1	402,01	10,1
2	417,61	10,1
3	436,61	10,1
4	455,61	10,1
5	474,61	10,1
6	493,61	10,1
7	512,61	10,1
8	531,61	10,1
9	550,61	10,1
10	569,61	10,1
11	588,61	10,1
12	607,61	10,1
13	626,61	10,1
14	645,61	10,1
15	664,61	10,1
16	683,61	10,1
17	702,61	10,1
18	721,61	10,1
19	740,61	10,1
20	759,61	10,1
21	778,61	10,1
22	797,61	10,1
23	816,61	10,1
24	835,61	10,1
25	854,61	10,1
26	873,61	10,1
27	892,61	10,1
28	911,61	10,1
29	930,61	10,1
30	949,61	10,1
31	968,61	10,1

Figure 20. AISA Eagle bands

1.3 Artificial Neural Networks (ANN)

Artificial Neural Networks, also known as "Artificial neural nets", "neural nets", or ANN for short, are a computational tool modeled on the interconnection of the neuron in the nervous systems of the human brain and that of other organisms. Biological Neural Nets (BNN) are the naturally occurring equivalent of the ANN. Both BNN and ANN are network systems constructed from atomic components known as "neurons". Artificial neural networks are very different from biological networks, although many of the concepts and characteristics of biological systems are faithfully reproduced in the artificial systems.

Artificial neural nets are a type of non-linear processing system that is ideally suited for a wide range of tasks, especially tasks where there is no existing algorithm for task completion. ANN can be trained to solve certain problems using a teaching method and sample data. In this way, identically constructed ANN can be used to perform different tasks depending on the training received. With proper training, ANN are capable of generalization, the ability to recognize similarities among different input patterns, especially patterns that have been corrupted by noise.

The term "Neural Net" refers to both the biological and artificial variants, although typically the term is used to refer to artificial systems only. Mathematically, neural nets are nonlinear. Each layer represents a non-linear combination of non-linear functions from the previous layer. Each neuron is a multiple-input, multiple-output (MIMO) system that receives signals from the inputs, produces a resultant signal, and transmits that signal to all outputs.

Practically, neurons in an ANN are arranged into layers. The first layer that interacts with the environment to receive input is known as the input layer. The final layer that interacts with the output to present the processed data is known as the output layer. Layers between the input and the output layer that do not have any interaction with the environment are known as hidden layers. Increasing the complexity of an ANN, and thus its computational capacity, requires the addition of more hidden layers, and more neurons per layer.

Biological neurons are connected in very complicated networks. Some regions of the human brain such as the cerebellum are composed of very regular patterns of neurons.

Other regions of the brain, such as the cerebrum have less regular arrangements. A typical biological neural system has millions or billions of cells, each with thousands of interconnections with other neurons. Current artificial systems cannot achieve this level of complexity, and so cannot be used to reproduce the behavior of biological systems exactly.

1.3.1 Processing Elements

In an artificial neural network, neurons can take many forms and are typically referred to as **Processing Elements** (PE) to differentiate them from the biological equivalents. The PE are connected into a particular network pattern, with different patterns serving different functional purposes. Unlike biological neurons with chemical interconnections, the PE in artificial systems are electrical only, and may be either analog, digital, or a hybrid. However, to reproduce the effect of the synapse, the connections between PE are assigned multiplicative weights, which can be calibrated or "trained" to produce the proper system output.

McCulloch-Pitts Model

Processing Elements are typically defined in terms of two equations that represent the McCulloch-Pitts model of a neuron:

$$\zeta = \sum_i w_i x_i$$
$$y = \sigma(\zeta)$$

Where ζ is the weighted sum of the inputs (the inner product of the input vector and the tap-weight vector), and $\sigma(\zeta)$ is a function of the weighted sum. If we recognize that the weight and input elements form vectors $\mathbf{w}$ and $\mathbf{x}$, the ζ weighted sum becomes a simple dot product:

$$\zeta = \mathbf{w} \cdot \mathbf{x}$$
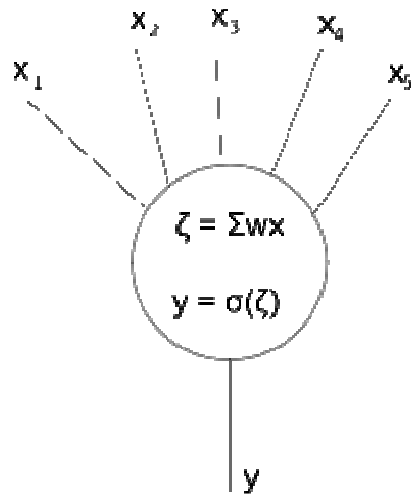
Figure 21. Activation/Transfer function

This may be called either the activation function (in the case of a threshold comparison) or a transfer function. Figure 21 shows this relationship diagrammatically. The dotted line in the center of the neuron represents the division between the calculation of the input sum using the weight vector, and the calculation of the output value using the activation function. In an actual artificial neuron, this division may not be made explicitly.

The inputs to the network, X, come from an input space and the system outputs are part of the output space. For some networks, the output space Y may be as simple as {0, 1}, or it may be a complex multi-dimensional space. Neural networks tend to have one input per degree of freedom in the input space, and one output per degree of freedom in the output space.

The tap weight vector is updated during training by various algorithms. One of the more popular of which is the backpropagation algorithm which we will discuss in more detail later.

Artificial neural nets have a number of properties that make them an attractive alternative to traditional problem-solving techniques. The two main alternatives to using neural nets are to develop an algorithmic solution, and to use an expert system.

Algorithmic methods arise when there is sufficient information about the data and the underlying theory. By understanding the data and the theoretical relationship between the data, we can directly calculate unknown solutions from the problem space. Ordinary von Neumann computers can be used to calculate these relationships quickly and efficiently from a numerical algorithm.

Expert systems, by contrast, are used in situations where there is insufficient data and theoretical background to create any kind of a reliable problem model. In these cases, the knowledge and rationale of human experts is codified into an expert system. Expert systems emulate the deduction processes of a human expert, by collecting information and traversing the solution space in a directed manner. Expert systems are typically able to perform very well in the absence of an accurate problem model and complete data. However, where sufficient data or an algorithmic solution is available, expert systems are a less than ideal choice.

Artificial neural nets are useful for situations where there is an abundance of data, but little underlying theory. The data, which typically arises through extensive experimentation may be non-linear, non-stationary, or chaotic, and so may not be easily modeled. Input-output spaces may be so complex that a reasonable traversal with an expert system is not a satisfactory option. Importantly, neural nets do not require any a priori assumptions about the problem space, not even information about statistical distribution.

Though such assumptions are not required, it has been found that the addition of such a priori information as the statistical distribution of the input space can help to speed training. Many mathematical problem models tend to assume that data lies in a standard distribution pattern, such as Gaussian or Maxwell-Boltzmann distributions. Neural networks require no such assumption. During training, the neural network performs the necessary analytical work, which would require non-trivial effort on the part of the analyst if other methods were to be used.

1.3.2 Learning

Learning is a fundamental component to an intelligent system, although a precise definition of learning is hard to produce. In terms of an artificial neural network, learning typically happens during a specific training phase. Once the network has been trained, it enters a production phase where it produces results independently. Training can take on many different forms, using a combination of learning paradigms, learning rules, and learning algorithms. A system which has distinct learning and production phases is known as a static network. Networks which are able to continue learning during production use are known as dynamical systems.

A learning paradigm is supervised, unsupervised or a hybrid of the two, and reflects the method in which training data is presented to the neural network. A method that combines supervised and unsupervised training is known as a hybrid method. A learning rule is a model for the types of methods to be used to train the system, and also a goal for what types of results are to be produced. The learning algorithm is the specific mathematical method that is used to update the inter-neuronal synaptic weights during each training iteration. Under each learning rule, there are a variety of possible learning algorithms for use. Most algorithms can only be used with a single learning rule. Learning rules and learning algorithms can typically be used with either supervised or unsupervised learning paradigms, however, and each will produce a different effect.

Overtraining is a problem that arises when too many training examples are provided, and the system becomes incapable of useful generalization. This can also occur when there are too many neurons in the network and the capacity for computation exceeds the dimensionality of the input space. During training, care must be taken not to provide too many input examples and different numbers of training examples could produce very different results in the quality and robustness of the network.

1.3.3 Network Parameters

There are a number of different parameters that must be decided upon when designing a neural network. Among these parameters are the number of layers, the number of neurons per layer, the number of training iterations, et cetera (Fig. 22). Some of the more important parameters in terms of training and network capacity are the number of hidden neurons, the learning rate and the momentum parameter.

Number of neurons in the hidden layer

Hidden neurons are the neurons that are neither in the input layer nor the output layer. These neurons are essentially hidden from view, and their number and organization can typically be treated as a black box to people who are interfacing with the system (Fig. 23). Using additional layers of hidden neurons enables greater processing power and system flexibility. This additional flexibility comes at the cost of additional complexity in the training algorithm. Having too many hidden neurons is analogous to a system of equations with more equations than there are free variables: the system is over specified, and is incapable of generalization. Having too few hidden neurons,

conversely, can prevent the system from properly fitting the input data, and reduces the robustness of the system.
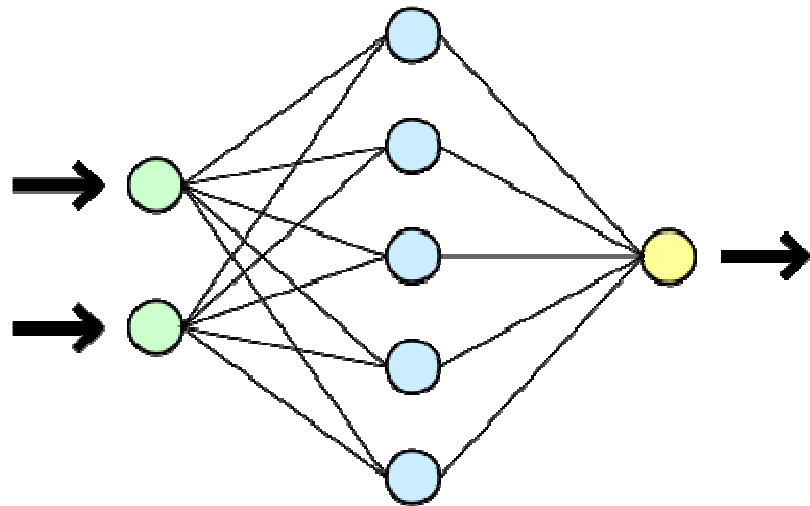
Figure 22. Neuron Network
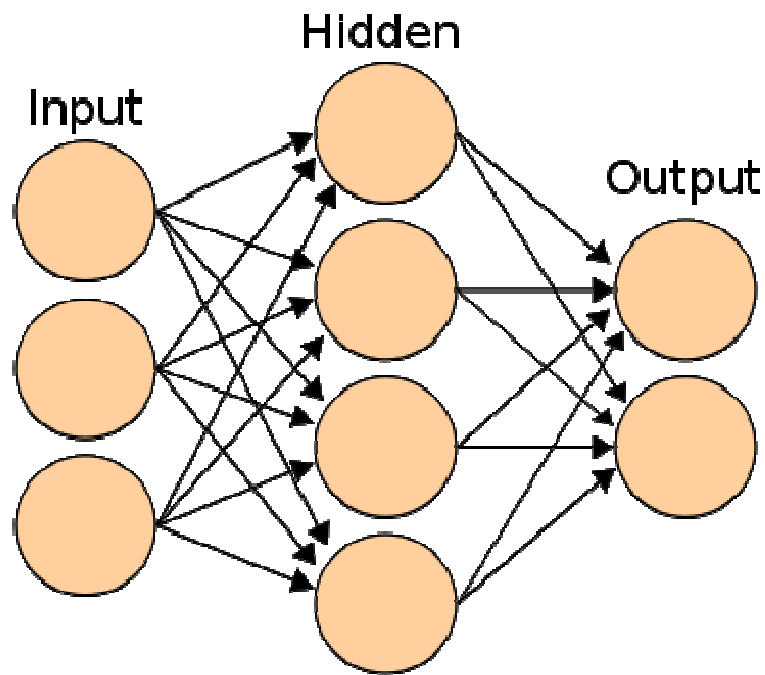
Figure 23. Hidden Layer

Learning Rate

Training parameter that controls the size of weight and bias changes during learning.

Momentum

Momentum simply adds a fraction m of the previous weight update to the current one. The momentum parameter is used to prevent the system from converging to a local minimum or saddle point. A high momentum parameter can also help to increase the

speed of convergence of the system. However, setting the momentum parameter too high can create a risk of overshooting the minimum, which can cause the system to become unstable. A momentum coefficient that is too low cannot reliably avoid local minima, and can also slow down the training of the system.

Training type

Meaning: 0 = train by epoch, 1 = train by minimum error

Epoc*h*

Determines when training will stop once the number of iterations exceeds epochs. When training by minimum error, this represents the maximum number of iterations.

Minimum Error

Minimum mean square error of the epoch. Square root of the sum of squared differences between the network targets and actual outputs divided by number of patterns (only for training by minimum error).

1.3.4 Tiberius data mining software

Tiberius is a predictive modelling software from Tiberius Data Mining, Melbourne, Australia.

It is a free of charge data modelling and visualisation tool for university staff and students all over the world and is downloadable at the following url: http://www.tiberius.biz/download.html

Some of main Tiberius main features are:

Neural Networks
Support Vector Machine
Decision Tree
Logistic Regression
Regression Splines
Automatic scorecard building algorithms
Variable Ranker
3D data visualisation
Model monitoring tools
Data recoding
Reads SAS, SPSS, SQL Server, MySQL, Oracle, Teradata, Excel, Access, text files etc.
SAS, SQL, SPSS and other model code generation

Following is shown a brief tutorial focusing on the main classification steps :

- At very first we need to create a new Model, loading data:
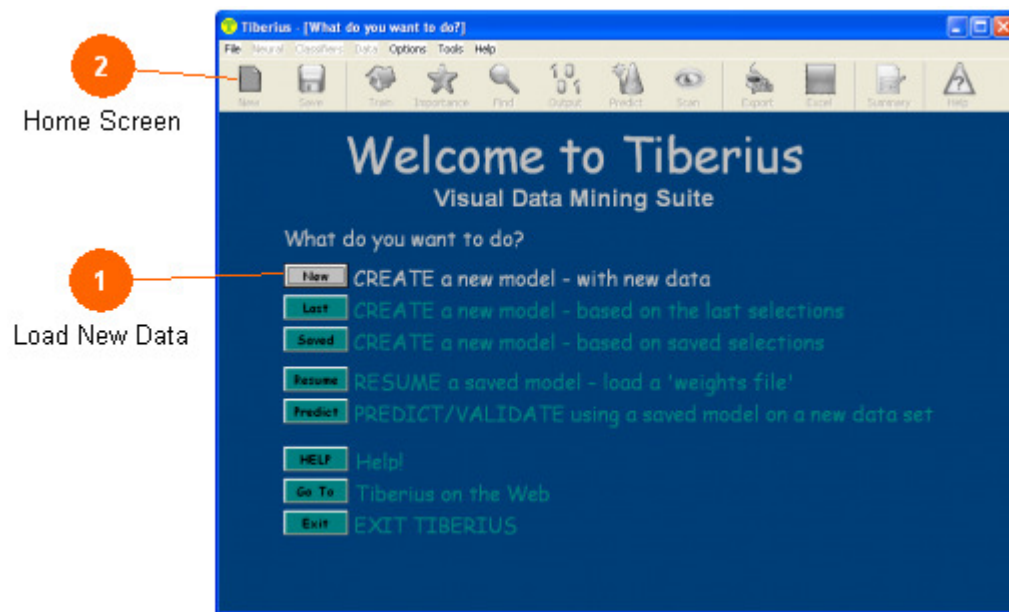
- After selected and loaded the data, we are requested to select what is to be predicted as the 'output' and the variables to be used to make the prediction as the 'inputs'. Any variable not loaded in at this stage will be unavailable to the model. Variables that are selected at this stage can subsequently be removed if they are not required to be in the model.
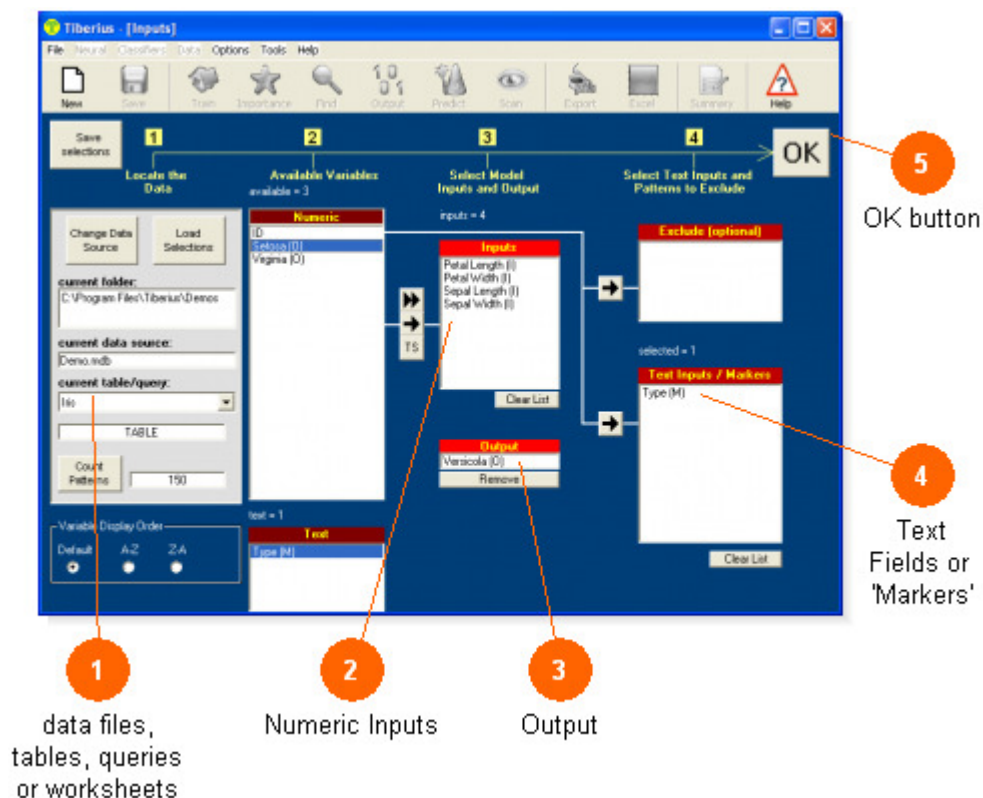
- We will now build our first neural network model: Press the 'Add Neuron' (1) button to add a neuron to the neural network. The diagram will change to represent the current network architecture as neurons are added or removed.

In order to start the learning process, press the 'Press to train' button (2). To stop the learning, press it again. Learning will only automatically stop once 100% correct classification has been achieved.

As the model is learning, the classification success rates are displayed (3).
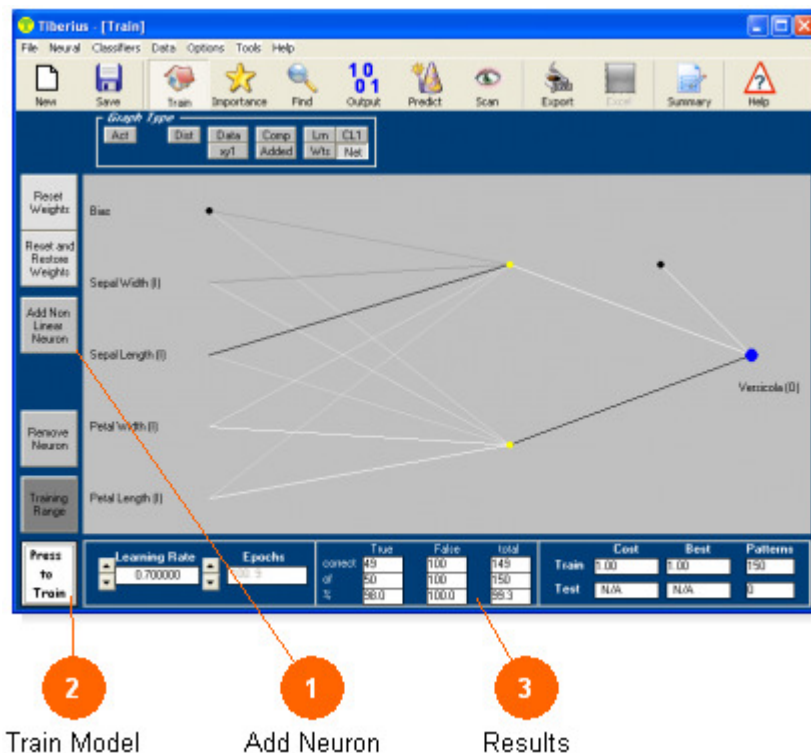
- An important step is good to determine which inputs are the important ones; some variables can be completely unimportant and be safely removed. This can be tested by adding randomly generated numbers as inputs and checking the importance of these variables once the model is built:

Variable Importance   Importance Grid
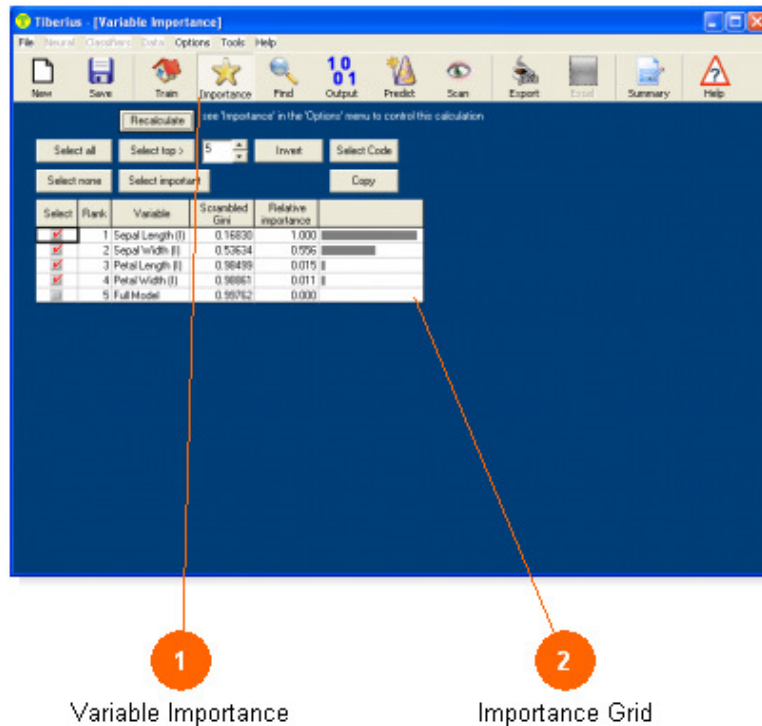
- For classification problems, the data summary form has a tab called 'Important Variables'. The 'information value' of a variable is a metric that indicates the ability of that variable to split the two classes. The higher the 'information value' the better.
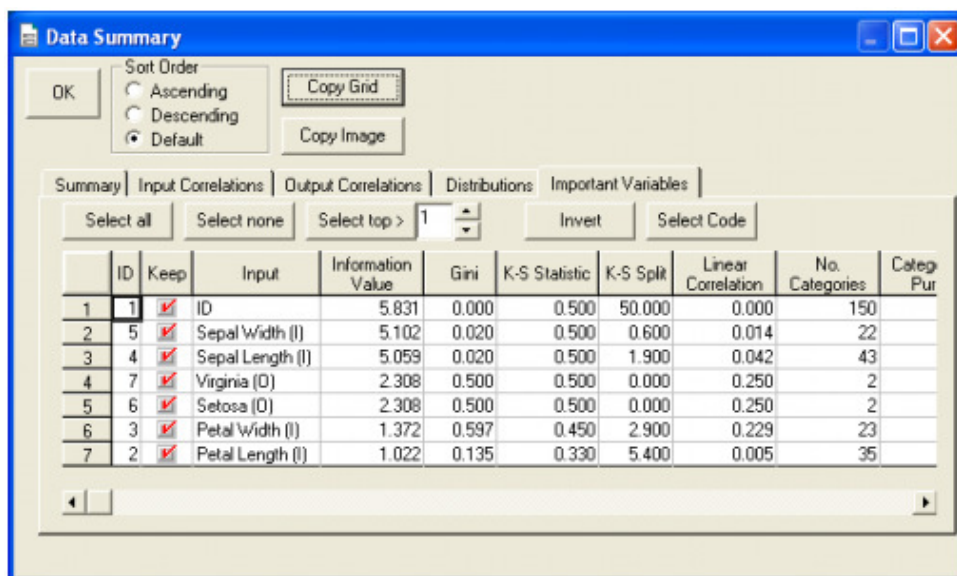
- Histograms (split by class) of the raw data, final model scores and model errors can be viewed. These histograms should give a graphic demonstration of why certain variables are important and why some are not. The red and blue bars indicate the class distribution. Separation of the two colours should be more evident for the more important variables in the model.
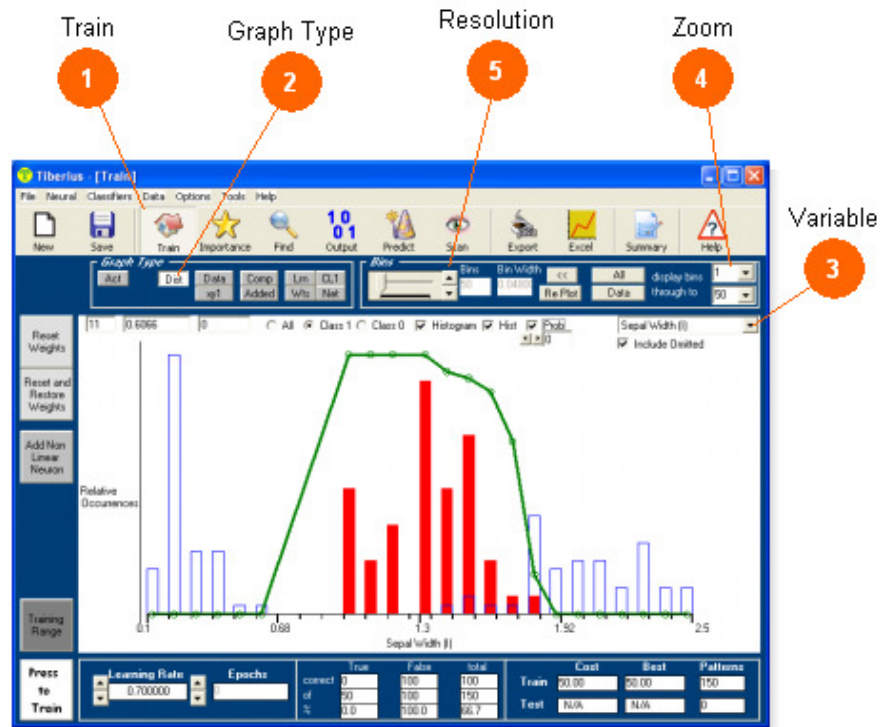
- To visualise relationships between the inputs and the output, a 3D viewing tool is available. The 3D Viewer allows visualisation of the raw data. There are numerous controls to drill down on the data of specific interest:
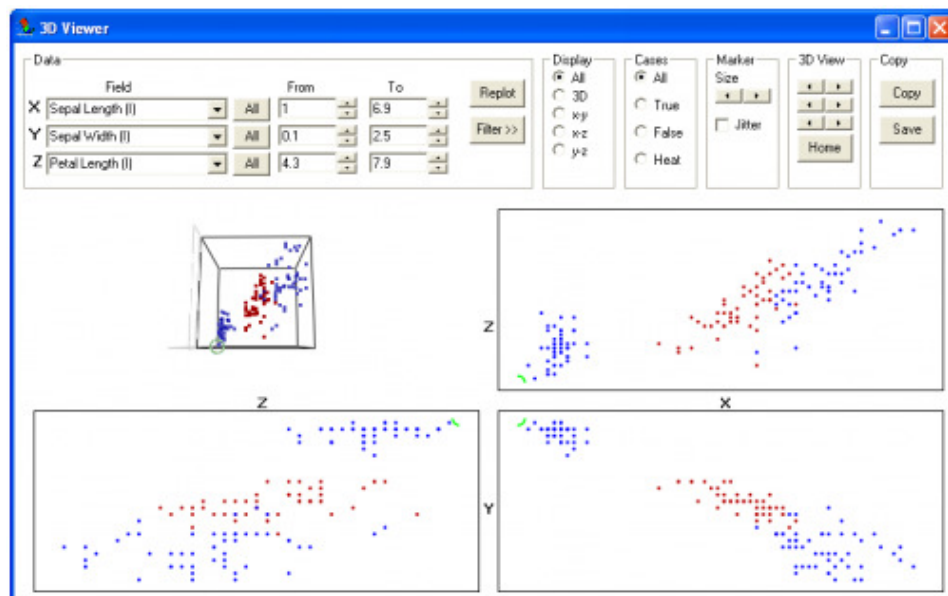
1.4 Spectral Mixture Analysis

The linear SMA approach assumes that the spectrum measured by a sensor is a linear combination of the spectra of all components within the pixel (Adams, *et al.*, 1995; Roberts, *et al.*, 1998a). The mathematical model can be expressed as

$$R_i = \sum_{K=1}^{n} fkR_{ik} + \varepsilon_i$$

where *i* is the number of spectral bands used; k _ 1, . . . , *n* (number of endmembers); *Ri* is the spectral reflectance of band *i* of a pixel, which contains one or more endmembers; *fk* is the proportion of endmember *k* within the pixel; *Rik* is known as the spectral reflectance of endmember *k* within the pixel on band *i*, and _*i* is the error for band *i*. To solve *fk*, the following conditions must be satisfied: (1) selected endmembers should be independent of each other, (2) the number of endmembers should be less than or equal to the spectral bands used, and (3) selected spectral bands should not be highly correlated.

It is well recognized that remotely sensed data, such as visible bands in Landsat TM/ETM+ data, are highly correlated between the adjacent spectral wavebands (Barnsley, 1999). Several techniques have been used to transform the data from highly correlated bands to an orthogonal subset.

Principal component analysis (PCA) and minimum noise fraction (MNF) are the two most common transformations (Green, *et al.*, 1988; Boardman and Kruse, 1994; Jensen, 1996). The MNF transform contains two steps (ENVI, 2000): (1) de-correlation and rescaling of the noise in the data based on an estimated noise covariance matrix, producing transformed data in which the noise has unit variance and no band-to-band correlations; and (2) implementation of a standard PCA of the noise-whitened data.

The result of MNF is a two-part dataset, one part associated with large eigenvalues and coherent eigenimages, and a complementary part with near-unity eigenvalues and noisedominated images (ENVI, 2000). In the MNF transform, the noise is separated from the data by using only the coherent portions, thus improving spectral processing results. Previous studies have shown that use of MNF transform can improve the quality of fraction images (van der Meer and de Jong, 2000; Small, 2001; Lu, *et al.*, 2002; Small, 2002; Wu and Murray, 2003), and thus the MNF transform was used in this study.

Development of high-quality fraction images depends greatly on the selection of suitable endmembers. A variety of methods have been developed to determine endmembers. For example, endmembers can be obtained from (1) a spectral library, or field reflectance measurements; (2) the image itself (Quarmby, *et al*., 1992; Settle and Drake, 1993) or high-order PCA eigenvectors (Boardman, 1993); (3) spectrally pure pixels identified using the Pixel Purity Index (PPI) (Boardman, *et al*., 1995), which are selected manually by visualizing the PPI results in an N-dimensional visualizer with ENVI (ENVI, 2000); (4) manual endmember selection (Bateson and Curtiss, 1996), which is a multidimensional visualization technique for interactivelyexploring the mixing space in search of spectra to designate as endmembers; and (5) the combination of image and reference endmember selection methods. The combination approach involves a spectral alignment between image endmembers and reference endmembers, and a calibration to relate image endmembers to reference endmembers (Smith,*et al*., 1990; Roberts, *et al*., 1993). For most SMA applications, image endmembers are utilized because they can be easily obtained and can represent spectra measured at the same scale as the image data (Roberts, *et al*., 1998a). The endmembers are regarded as the extremes in the triangles of an image scattergram. Hence, the image endmembers can be identified from the scatterplots of two spectral bands.

Urban landscapes are typically composed of features that are smaller than the spatial resolution of the sensors, a complex combination of buildings, roads, grass, trees, soil, water, and so on. Strahler, *et al.* (1986) described H- and L-resolution scene models based on the relationships between the size of the scene elements and the resolution cell of the sensor. The scene elements in the H-resolution model are larger than the resolution cell and can, therefore, be directly detected. In contrast, the elements in the L-resolution model are smaller than the resolution cells, and are not detectable. When the objects in the scene become increasingly smaller relative to the resolution cell size, they may be no longer regarded as objects individually. Hence, the reflectance measured by the sensor can be treated as a sum of interactions among various classes of scene elements as weighted by their relative proportions (Strahler, *et al*., 1986).

Landsat Thematic Mapper (TM) or Enhanced Thematic Mapper Plus (ETM+) images with a nominal 30 meter spatial resolution are attributed to L-resolution model. These data are often considered too coarse for mapping the components of urban environments. As the spatial resolution interacts with the fabric of urban landscapes, a special problem of mixed pixels is created, where several landuse and land-cover

(LULC) types are contained in one pixel. Such a mixture becomes especially prevalent in residential areas where buildings, trees, lawns, concrete, and asphalt can all occur within a pixel.

Mixed pixels have been recognized as a problem affecting the effective use of remotely sensed data in LULC classification and change detection (Fisher, 1997; Cracknell, 1998). Fisher (1997) summarized four causes of the mixed pixel problem, i.e., (1) boundaries between two or more mapping units, (2) the intergrade between central concepts of mappable phenomena, (3) linear sub-pixel objects, and (4) small sub-pixel objects.

When mixed pixels occur, pure spectral responses of specific features are confused with the pure responses of other features, leading to the problem of composite signatures (Campbell, 2002). The low accuracy of LULC classification in urban areas is largely attributed to the mixed pixel problem. For example, the traditional per-pixel classifiers, such as maximum-likelihood classifier (MLC), cannot effectively handle complex urban landscapes and the mixed pixel problem. When unsupervised classification is applied to densely populated suburban metropolitan areas, the mixed pixel problem becomes exaggerated.

Trees on lawns are confused with forest classes. Lawns are similar to pasture and recreation, and pavement is common in high-density residential and commercial/industrial areas (Epstein, *et al.*, 2002). In practice, accurate classification results are a prerequisite for many environmental and socioeconomic applications, such as urban change detection (Chen, *et al.*, 2000; Ward, *et al.*, 2000), urban heat islands (Lo, *et al.*, 1997; Quattrochi, *et al.*, 2000; Weng, 2001), and estimation of biophysical, demographic, and socioeconomic variables (Lo, 1995; Thomson and Hardin, 2000). Improving LULC classification accuracy has been an important theme in remote sensing literature.

Different approaches have been used to improve urban LULC classification or change detection accuracies. These approaches include incorporation of geographic data (Harris and Ventura, 1995), census data (Mesev, 1998), texture features (Myint, 2001; Shaban and Dikshit, 2001), and structure or contextual information (Gong and Howarth, 1990; Stuckens, *et al.*, 2000) into remote sensing spectral data, use of expert systems (Stefanov, *et al.*, 2001; Hung and Ridd, 2002) and fuzzy classification (Zhang and Foody, 2001), use of multisensor data such as merged radar and TM data (Haack, *et al.*, 2002), merged SPOT and TM data (Gluch, 2002), and merged Airborne

Visible/Infrared Imaging Spectrometer (AVIRIS) and radar data (Chen, *et al.*, 2003). One of the major advances in urban LULC analysis is Ridd's (1995) vegetation—impervious surface—soil (V-I-S) model (Figure 24):
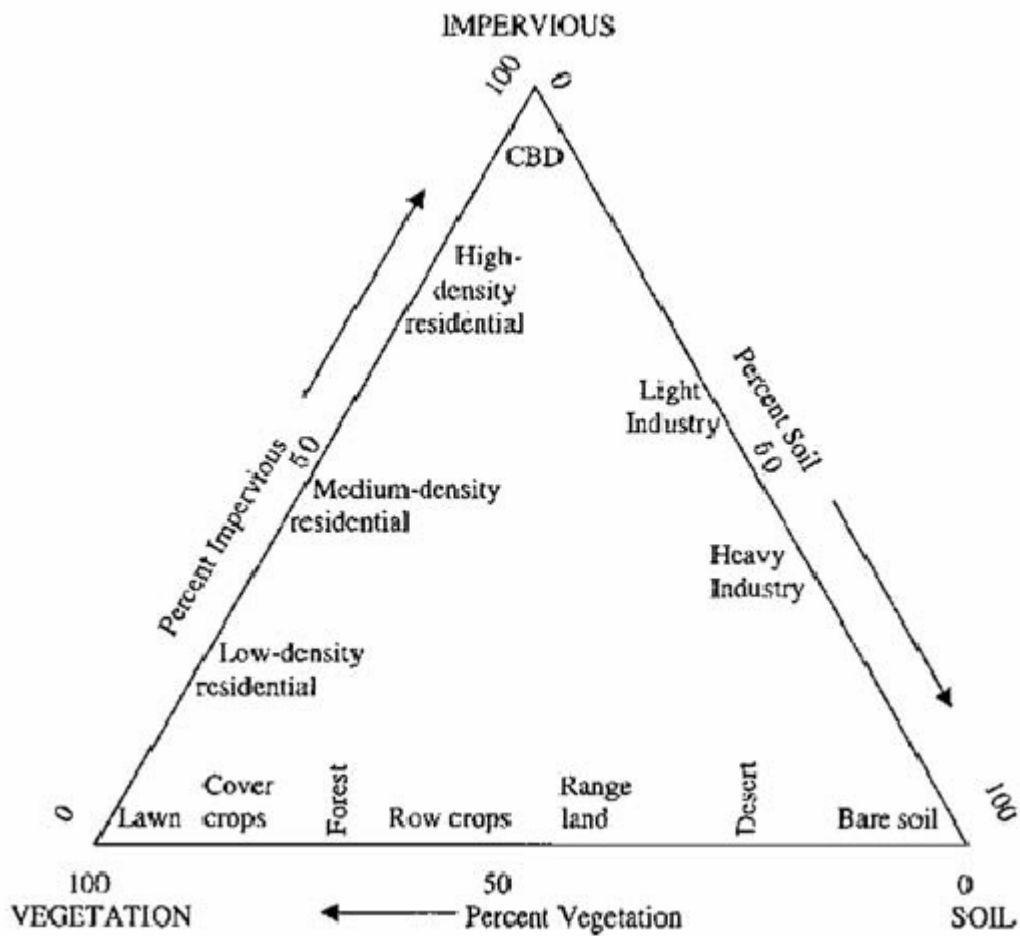
Figure 24. The V-I-S (Vegetation—Impervious surface—Soil) model illustrating the characteristics of urban landscapes (Ridd, 1995).

It assumes that land cover in urban environments is a linear combination of three components: vegetation, impervious surface, and soil. This model provides a guideline for decomposing urban landscapes and a link for these components to remote sensing spectral characteristics.

Several studies have adopted this model as a basis for understanding the urban environment. Ward, *et al.* (2000) used a hierarchical unsupervised classification scheme to classify four classes (water, forest, cleared, and urban) on a per-pixel basis and applied the approach to a TM image in southeast Queensland, Australia, based on the V-I-S model.

An adjusted overall accuracy of 83 percent was achieved. Madhavan, *et al.* (2001) used an unsupervised classifier (ISODATA) to classify TM images into seven classes in the Bangkok Metropolitan area, Thailand.

The V-I-S model proved to be useful for the classifi- cation, although the classification accuracy was not as high as expected due to the complexity of the study area. Rashed, *et al.* (2001) conducted spectral mixture analysis (SMA) of IRS- 1C multispectral image to describe the anatomy of the Greater Cairo Region, Egypt, based on four image endmembers: vegetation, impervious surface, soil, and shade. A decision tree classifier (DTC) was then applied to the fraction images.

The classification accuracy was found to be higher than the accuracy achieved using MLC and minimum distance classifiers. Phinn, *et al.* (2002) compared traditional image classification, interpretation of aerial photographs, and constrained linear SMA using a TM image in southeast Queensland, Australia, and found that the V-I-S fraction images derived from SMA provided better classification results than per-pixel classification and aggregated aerial photo interpretation.

Wu and Murray (2003) used SMA to analyze impervious surface distribution in the metropolitan area of Columbus, Ohio, USA, and found that impervious surface can be estimated using a linear regression model of low and high albedo endmember fractions.

Although the V-I-S model has demonstrated usefulness for identifying and characterizing urban land cover patterns, its use in practice is constrained due to the following factors. First, the V-I-S model cannot explain all land cover types such as water and wetlands. Second, impervious surface in the V-I-S model cannot be easily identified as an endmember based on remote sensing images (Wu and Murray, 2003) because impervious surface is a complex mixture of different materials, including concrete, asphalt, metals, plastic, and soils (Jensen, 2000). Finally, the V-I-S model excludes an important component in the mixed pixels, i.e., the shade. Shade, caused by tall buildings or trees, is an important factor affecting the spectral response patterns of urban landscapes and should be an essential consideration in analyzing urban landscapes.

For medium-spatial resolution remotely sensed data, such as TM/ETM+, the central business district, light/heavy industry, high/medium density residential, and bare soils are difficult to differentiate using traditional digital image processing techniques. Recently SMA has attracted increasing interests in urban studies and has shown the

potential for estimating impervious surface and vegetation abundance, and for improving urban land-cover classification (Rashed, *et al*., 2001; Small, 2001; Phinn, *et al*., 2002; Small, 2002; Wu and Murray, 2003).

1.5 Data

1.5.1 LIDAR Data

- 2007 Digital Surface Model (DSM): 48 tiles of 1SqKm area each, pixel size 1m (Figure 25 a)

- 2007 Digital Terrain Model (DTM): 48 tiles of 1SqKm area each, pixel size 1m (Figure 25 b)

- 2007 48 tiles of LAS point clouds (area: 1SqKm each) over the Comune of Avellino entire area, range point density: 4/m (Fig. 26).
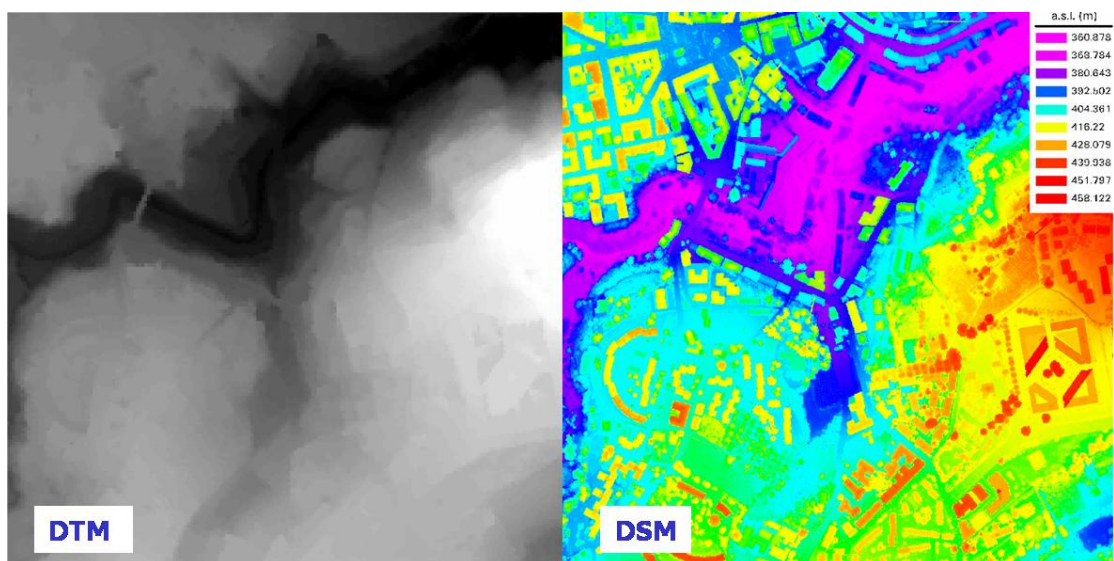
Figure 25 a and b. Avellino's DTM vs DSM (Detail)
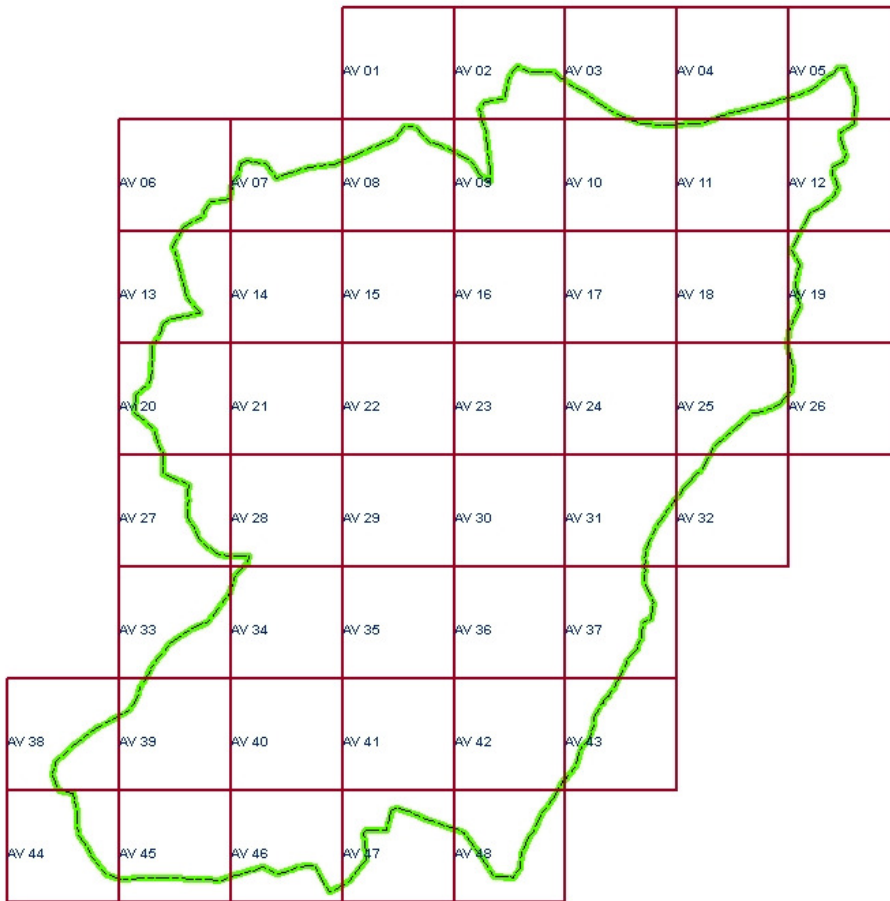
Figure 26. LIDAR collection cover area

1.5.2 Hyperspectral Data

- 2007 50 VNIR images at 31 bands ranging from 0.4 to 0.9 nm, pixel size 1m (Fig. 27)
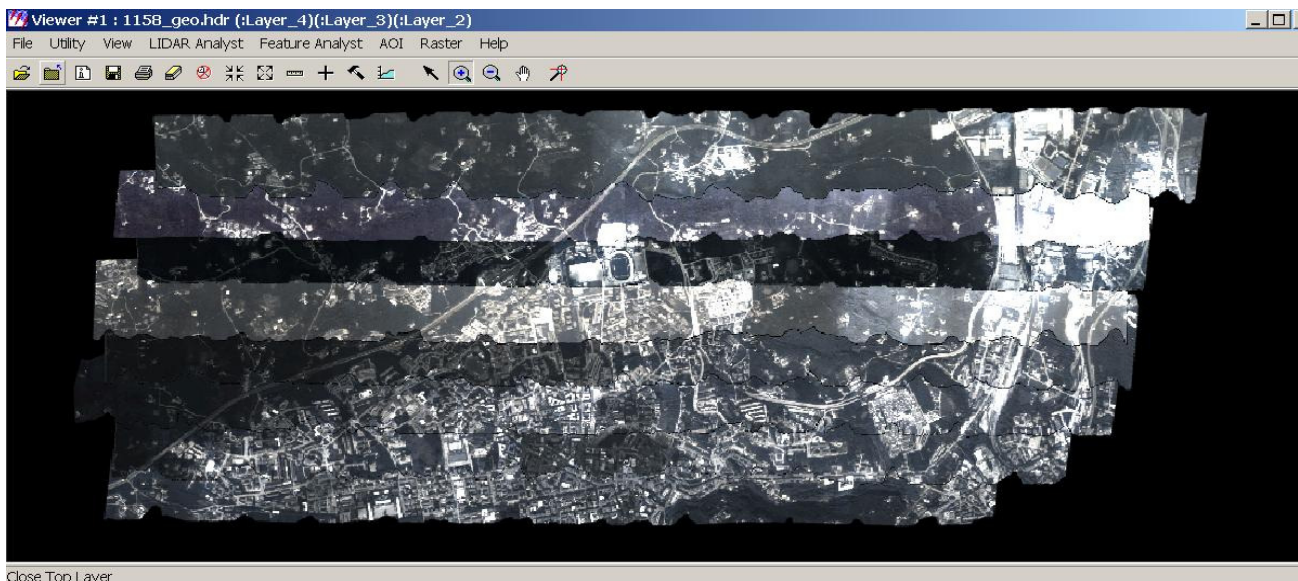
Figure 27. Hyperspectral Images Mosaic

1.5.3 Multispectral Data

- 1975 Landsat MSS quarter scene, pixel size

- 1993 Landsat TM quarter scene, pixel size

- 2000 Landsat ETM+ quarter scene, pixel size 30m

- 2005 and 2006 QuickBird MS Images, pixel size 3m

1.5.4 High-Resolution Image Data

- 1997 Aerial Panchromatic Photogrammetry Stereo Couples over the Comune

of Avellino entire area. Pixel size: 10cm (Figure 28)
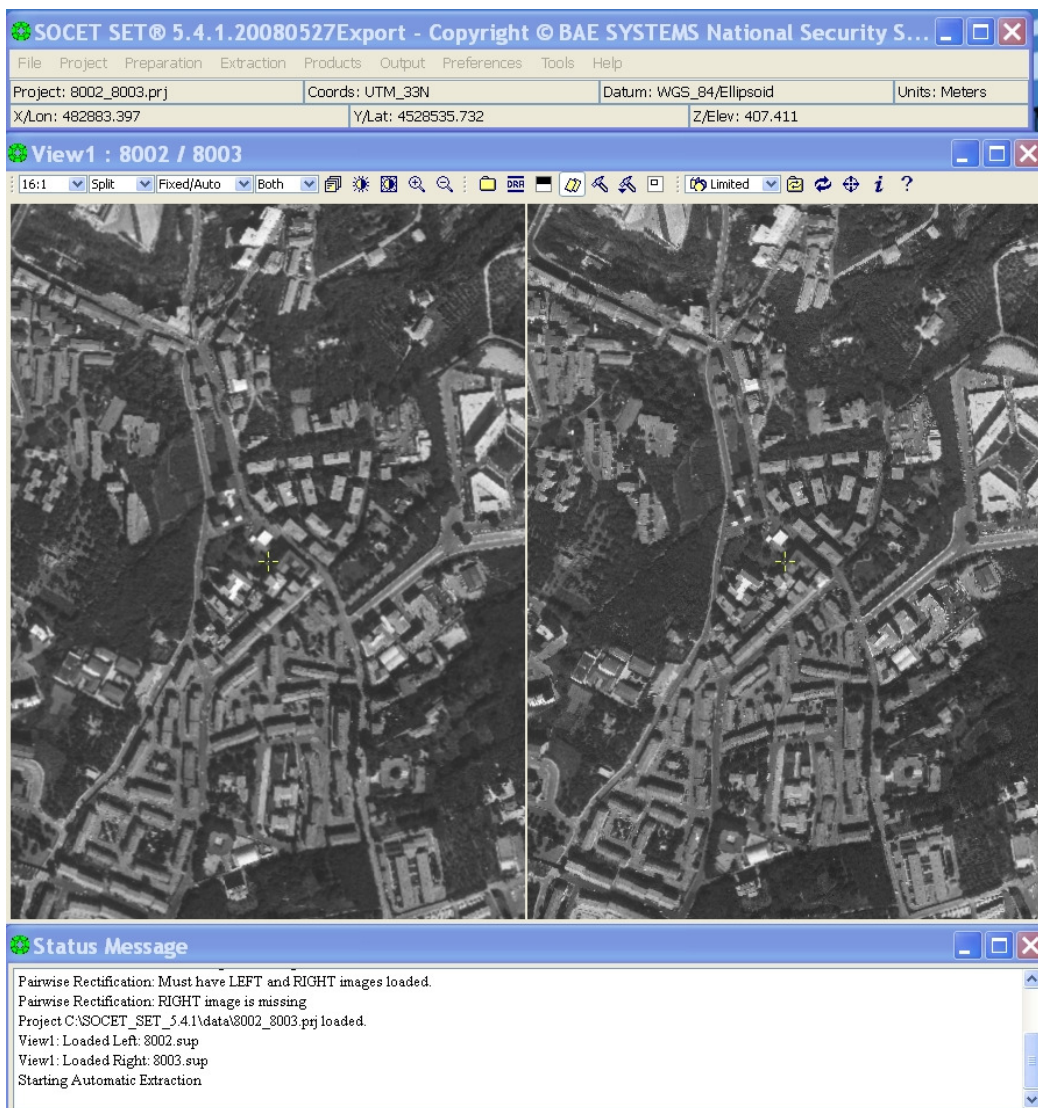
Figure 28.Aerial photogrammetric Stereo couple

- 2007 Panchromatic 'Intensity' Image over the Comune of Avellino entire area from LIDAR survey

- 1998 RGB Ortophoto over the Comune of Avellino entire area. Pixel size: 2m (Figure 29)

- 2007 RGB Orthophoto over the Comune of Avellino entire area. Pixel size 1m

Figure 29. Comune of Avellino RGB Ortophoto

• 2005 and 2006 QuickBird Panchromatic Images, pixel size 70cm

1.5.5 Cartographic (Vector and Raster) Data

• 1997 Comune of Avellino Cadastral Digital Map 1:2000 scale (source: Comune of Avellino)

• 2003 Comune of Avellino Digital Cartography 1:1000 scale (source: Comune of Avellino)

•

Chapter 2 – Methodology

2.1 Test areas

First of all, in order to reduce the computational times due to the huge amount of data availables, two test areas were identified within the whole area (Figure 30): the first one laying in the NE part of the town, near the railway station, while the other one in the southern part, in the so called San Tommaso district.

The San Tommaso district area, from now on called 30_36 (from the LIDAR survey tiles number) was specifically devoted to the test of the whole on-purpose developed chain (Figure 31).
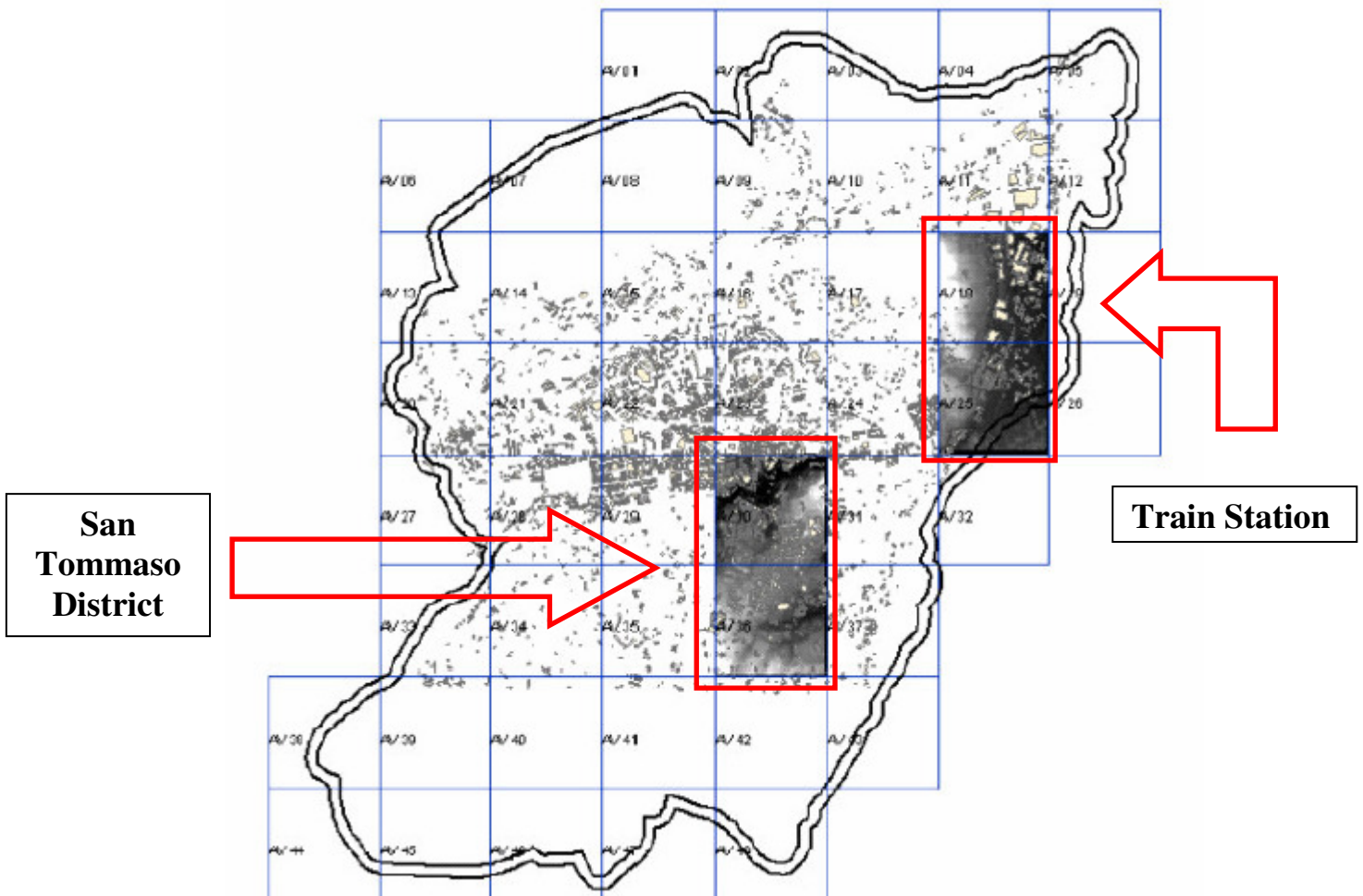
Figure 30. Test areas
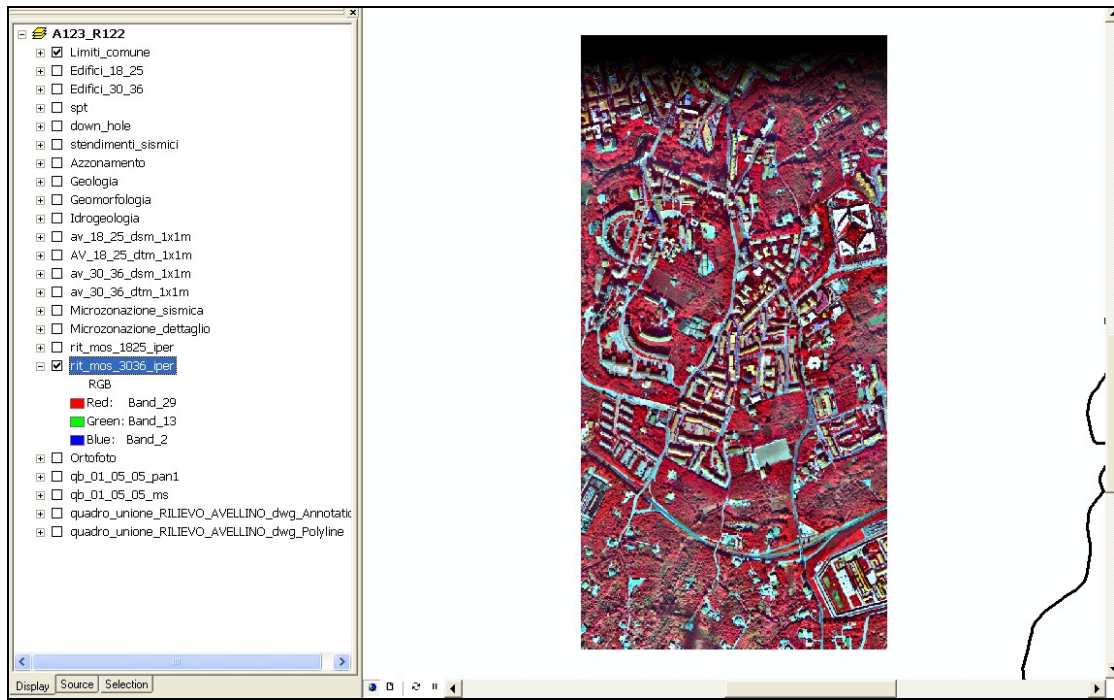
Figure 31. San Tommaso district Hyperspectral image

2.2 The vulnerability index

Iron concrete buildings represent the majority of the housing patrimony present on the Italian territory: for this construction typology, according to a more rigorous approach, the vulnerability can be defined as probability of damaging (derived from the related fragility analytical trends calculated for standard structures).

On the other hand, the relevant presence of masonry constructions, especially within the historical centres of Italian municipalities (pertaining to the large historical patrimony, often with remarkable cultural features), justifies the simplified approach here followed and mainly based on the index of vulnerability I_v.

| Typology | Code | Construction age | I_v | Floors | | | Agglomerate |
				1-2-3	4-5-6	>6	
Masonry	M6	1946 to 1971	30		5	10	6
		> 1971	20		5	10	6
Reinforced (iron) concrete	PC1	Before seismic classification (<2000)	20	-6	0	6	6
	RC2	After seismic classification (>2000)	0	-6	0	6	6

Table 1 - Vulnerability indices and modifiers for building typologies over the study area (adapted, from Giovinazzi and Lagomarsino, 2001)

The I_v index is defined through the statistical analysis of the damages on the build patrimony inventoried as a result of the seismic events happened [Giovinazzi and Lagomarsino, 2001] in the past on a regional basis. Such index is based firstly on the typology of the constructions which identifies macro-groups with those more representative in our test areas constituted by the reinforced concrete and masonry. Referring to this work, if we take in mind only the buildings in masonry they turn out more important those realized in full fire-bricks and those in masonry not armed with reinforced concrete floors, while for those completely in iron concrete it is necessary to distinguish from buildings constructed with required anti-seismic features after the year 2000 from the others built before.

The index I_v gets greater for the weaker structures more susceptible to be damaged and it has an interval going from -50 to 60. In addition to the buildings typologies, I_v is related also to other parameters and above all to the geometric ones which determine the modalities of response to the seismic wave in terms of displacement

For the three above described prevailing typologies in the zone of interest indicated by related codes (Cod.), in Table 1 are shown the indices of means vulnerabilities (I_v) with typical age of construction and the respective modifiers, depending on the level of maintenance, the height (expressed in number of floors) and from the belongings to agglomerates [Giovinazzi and Lagomarsino, 2001].

Besides these parameters, other proposed modifiers include the building's symmetry in elevation and planimetric and the geological/geotechnical characteristics of the soils beneath. Therefore, in general, besides relative information related to typology and state of the construction, it's important to have also information on height, surface and shape of the buildings standing in the urban area of interest, from which to derive the geometric parameters modifiers of Table 1.

2.3 Gathering required informations

According to Giovinazzi and Lagomarsino, in order to assign the proper I_v to buildings one have to know essentially:

- Floors number
- Whether to belong to an agglomerate or not
- Construction age

- Construction material

The floors number and the belonging to an agglomerate characteristics are related to geometrical factors, while the construction age and materials can be relatied mainly with the so called 'typology'.

In this work was developed an operational chain devoted to extract this kind of informations from remote sensed data, joined with some ancillary data.

In particular:

- the height of a building (and hence its floors number) and its belonging to an agglomerate can be calculated/evaluated through softcopy photogrammetry and/or LIDAR surveys, coupled with some cadastral maps;
- the construction age can be estimated via multitemporal image analysis;
- finally, the construction material can be inferred through hyperspectral remote sensing .

In the following pages will be presented this operational chain and its outcomes.

2.3.1 Three dimensional buildings extraction

A LIDAR airborne remote sensing mission was planned and carried out in 2007 over the entire municipality of Avellino, using an Optech ALTM 3100 system and acquiring range point clouds data with a density of 4 points for square meter. The flight plan has been designed to optimize the 3D restitution of the buildings in the urbanized areas.

The LIDAR raw data, once preliminary filtered and georeferenced, were processed through customised methodologies implemented and calibrated on the areas of interest [Ma, 2005; Borfecchia et al., 2007] (Figure 32) to obtain the DSM (Digital Surface Models) which was used to properly identify the ground points for extracting the DTM (Digital Terrain Model – Step 1) through interpolation; objects like buildings have been extracted from non-ground points (Step 2), so that it has been

possible to derive extensively height and floors number for each building within test area.

Given that the Optech ALTM 3100 is able to handle the laser multi-returns from semitransparent tree canopies, more reliable estimates were carried out also in urbanised areas where the shape of edifices is partially occluded by trees or vegetation (Step 3).

The LIDAR data, opportunely processed, besides to concur to a better planimetric and altimetric definition of the buildings, were used also for the geometric characterization of buildings roofs in term of their shape (in 4 classes: Flat Simple, Flat Multi-level, Pitched, Complex) and for the location of the distribution of the vegetation in the study areas (Figures 33 and 34).

Figure 32. Step-by-step LIDAR post processing chain
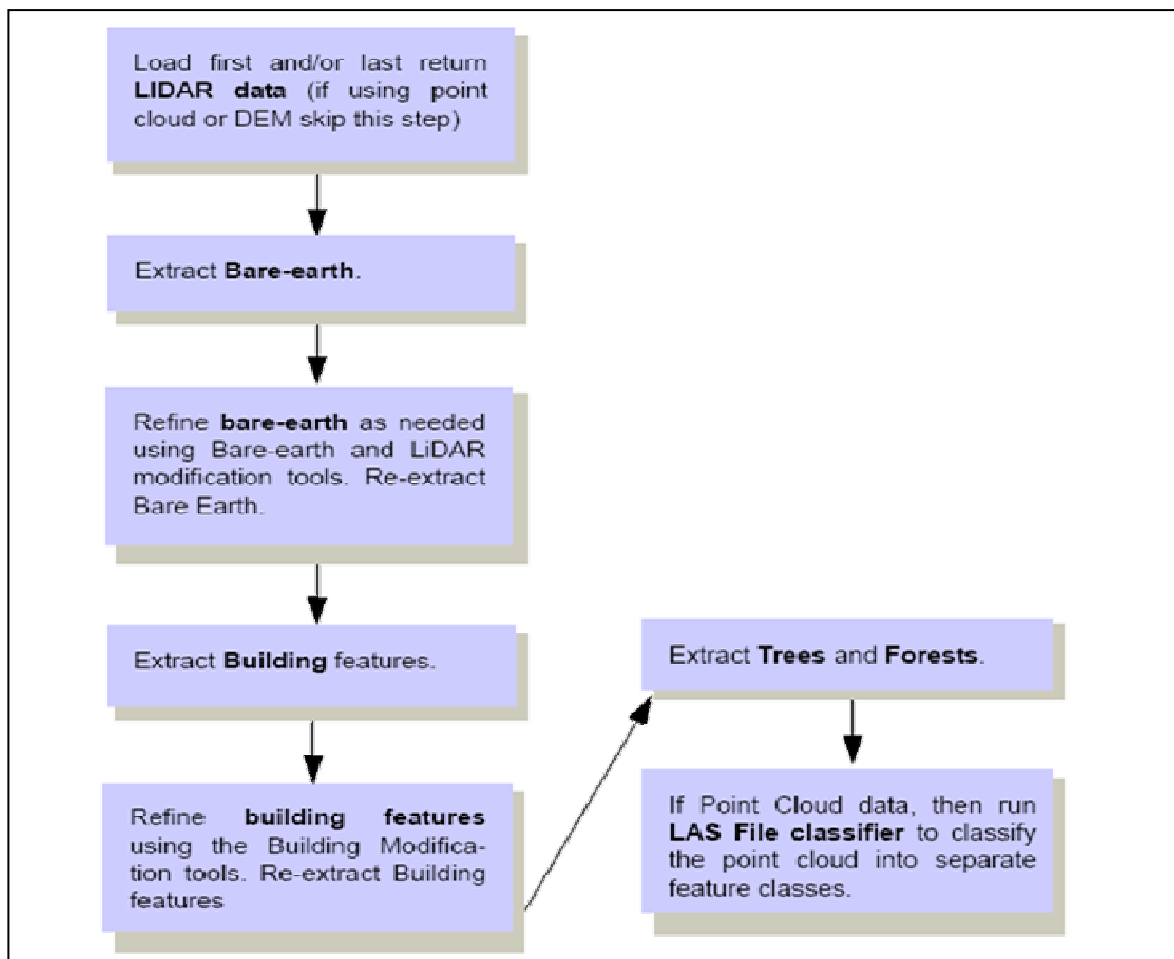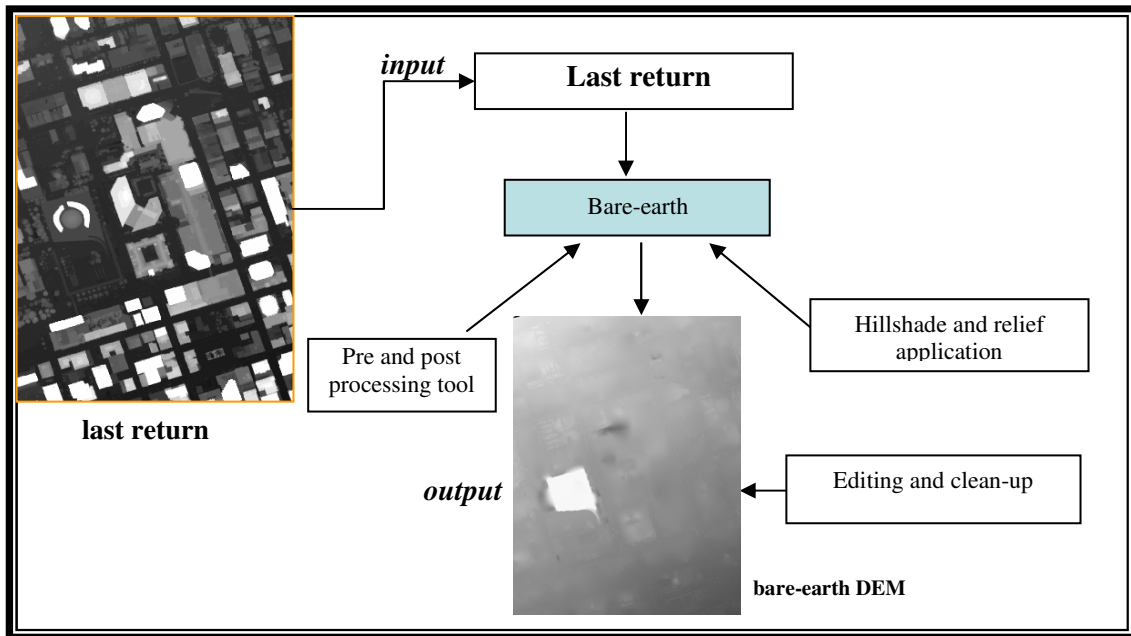
Step1. Point cloud bare-earth extraction
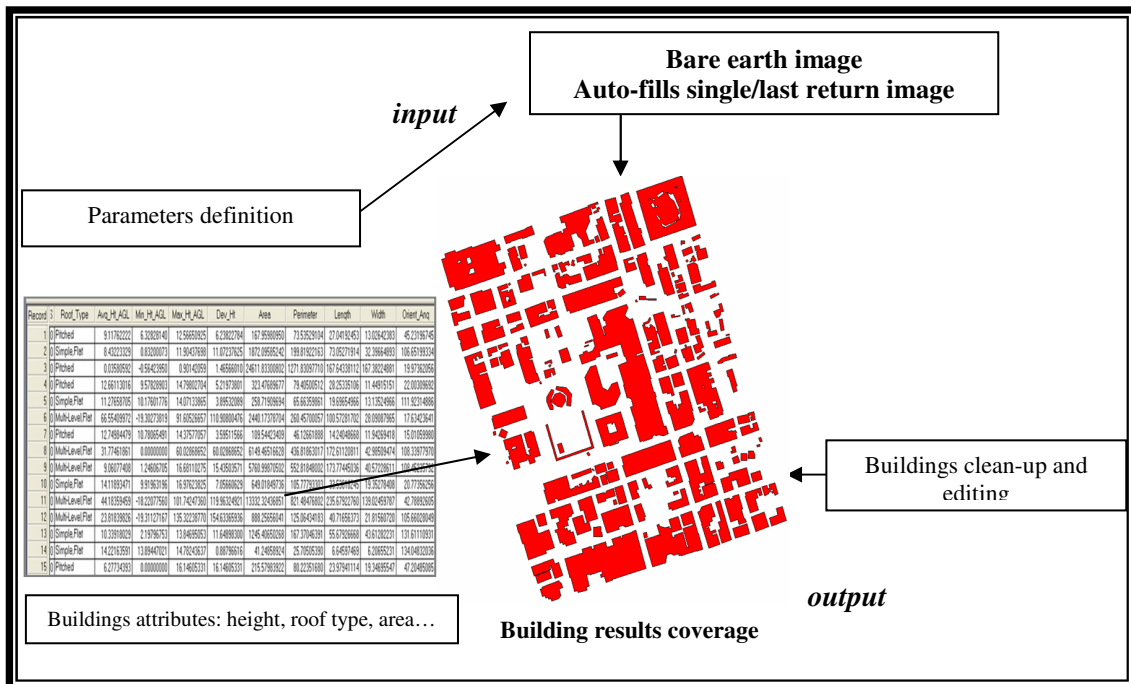
Step2. Point cloud building extraction
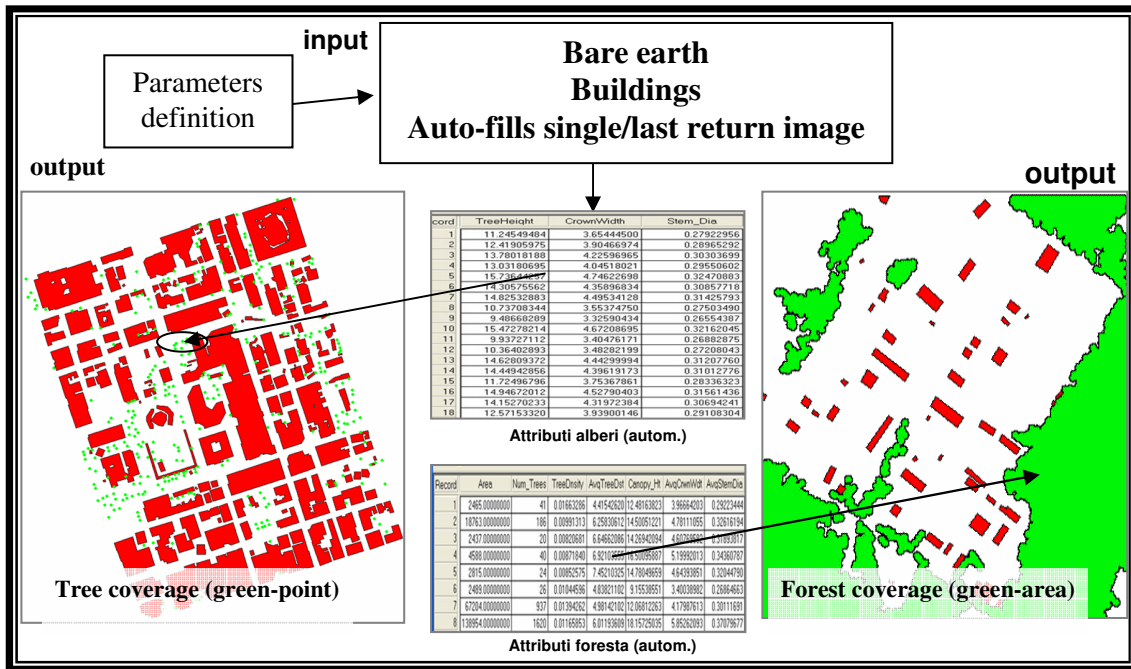
Step3. Point cloud tree and forest extraction
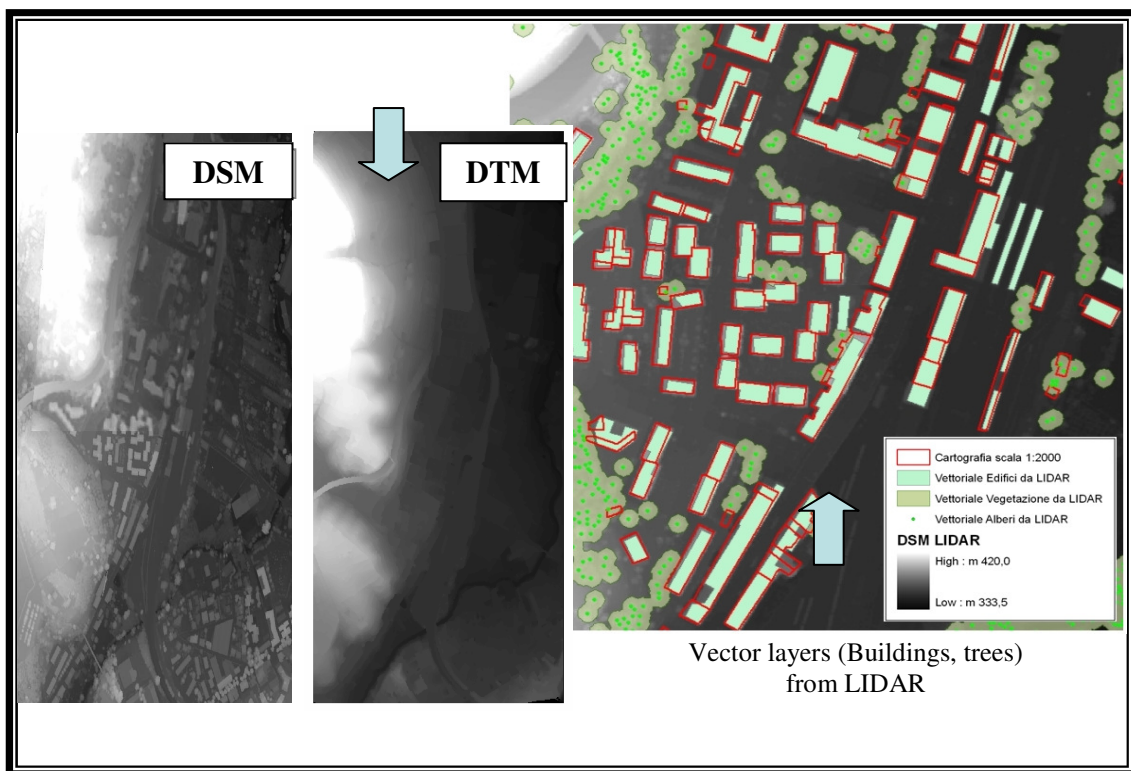
Figure 33. LIDAR elaboration chain results
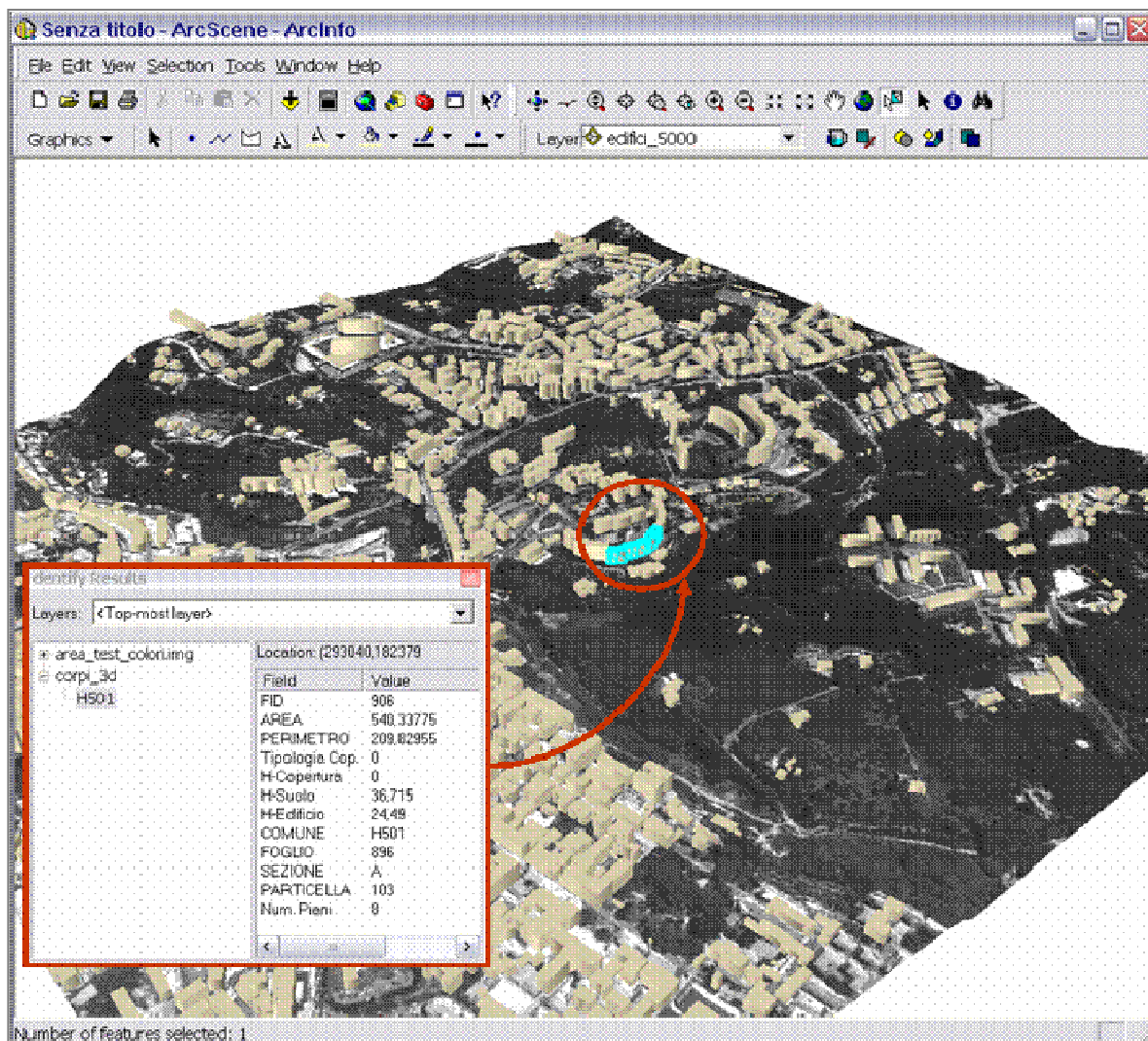
Figure 34. 3D buildings and terrain reconstruction

2.3.2 Estimating the construction age: Multitemporal analysis of the Urban Sprawl

In order to estimate the construction age of each building and keeping in mind the image data availables (three Landsat MS images dating fron 1975 to 2000 and a QuickBird MS image dating 2006), a multitemporal approach was followed.

The idea was actually quite simple: to give a construction time according with the change detected through Urban Sprawl, as follows:

- All the buildings in the MSS image were (obviously) already built in 1975 (Figure 35)

- All the buildings in the TM image that were not present in 1975 were built from 1975 and 1993 (Figure 36)

- All the buildings in the ETM+ image that were not present in 1993 were built from 1993 and 2000 (Figure 37 and 38)

- All the buildings in the QuickBird image that were not present in 2000 were build from 2000 and 2006 (thus following anti-seismic rules, Figure 39)

At the same time of the LIDAR data collection, a photographic RGB digital cover of the whole area was acquired by means of a digital camera in order to produce an orthophoto of the entire territory of Avellino, with a ground pixel size of 20 cm (used for accuracy assessment).

Taking into account the different ground resolution of sensors (60-30m Landsat scenes and 2.8m QuickBird) and the typical surface of building in the test areas, a spectral mixture analysis (SMA) approach was utilized for Landsat images while QuickBird data was processed according to more usual pixel/object classification schemas (Maximum Likelihood parametric, ML) to produce maps of built-up at the different dates.

Instead of pixel labeling, the output of SMA is conceived in terms of spectrally pure covers (*endemembers*) percentages which were preliminary verified on the Avellino municipality urban sprawl starting from 1975.

The high probability to be "mixed" for the MSS, TM and ETM+ 30x30m sized pixel data makes the application of the SMA more attractive than the standard classification methods which were used for the QuickBird data.

Via Sequential Maximum Angle Convex Cone algorithm [Gruninger et al., 2004], six endemembers were extracted from each Landsat imagery sub-areas referred mainly to different kind of built-up and infrastructures.

Considering the introduction of anti-seismic rules for new constructions (Tab. x), the change detection step to identify the buildings in reinforced concrete made before 2000 (without antiseismic features) was accomplished using a Landsat ETM+ scene and a QuickBird multispectral image, respectively acquired on August 2000 and October 2006.

The final classification was accomplished using different thresholds for the endemembers abundance validated by means of high resolution aerial photos taken at time of satellite overpass and applied to the entire area of interest.

It has been carried out an accuracy assessment for both classification typologies, according with the following methodology: in order to evaluate the pre and post 2000 classifications (ETM+, SMA), it has been decided that the single pixel identified as building should have been correctly labelled if its surface was covered at least by a 50% of buildings at the ground.

For the 2006 classification (QuickBird, ML) instead, it has been decided to assign the status of correctly classified not to the single pixel but to *clumps* with a minimum surface of 48 sqm (i.e. 3 pixels).

Ground truth data were derived from suitable aerial photos (1998, 2003 and 2007 surveys) at appropriate scales and used by a photointerpretation approach with QuickBird 2006 panchromatic image integration for the accuracy assessments needs.

The results are summarized in the following Table 2.

Year	Total Pixels/Clump	Buildings	%	Other	%
2000	226	191	84.5	35	15.5
2006	244	172	70.5	72	29.5

Table 2 - Classification Accuracy assessment
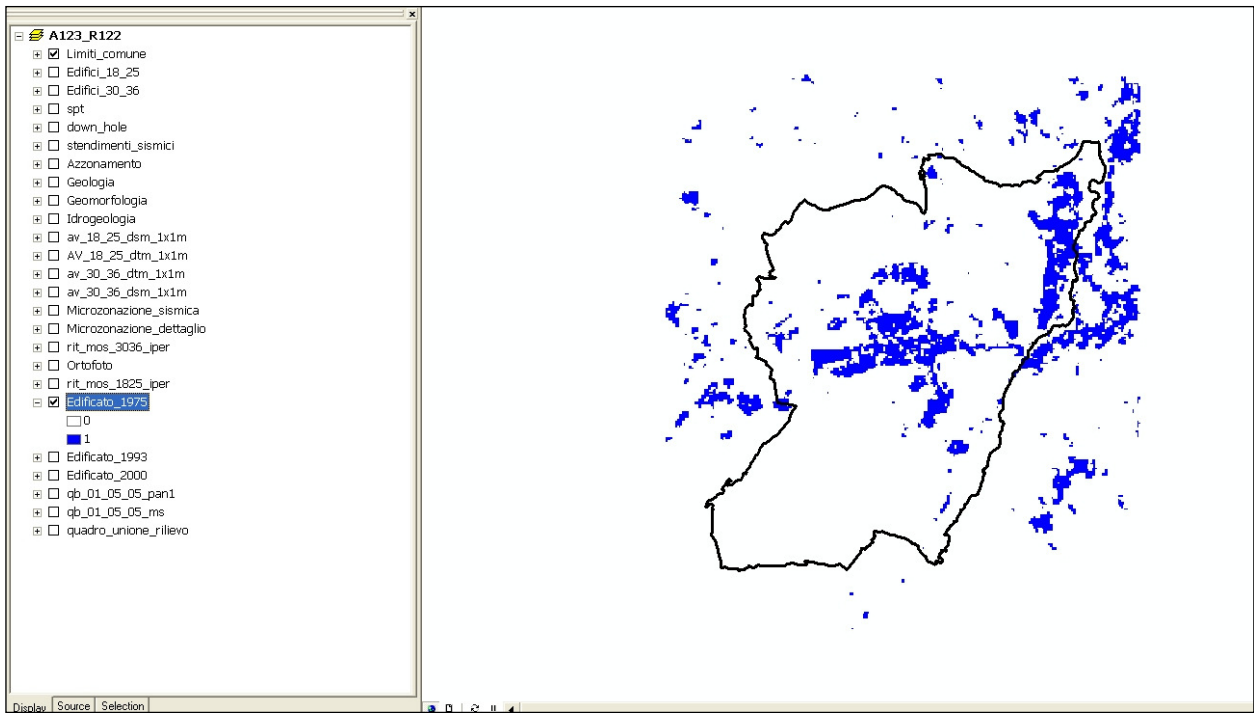
Figure 35. Built-up from 1975 Landsat MSS image
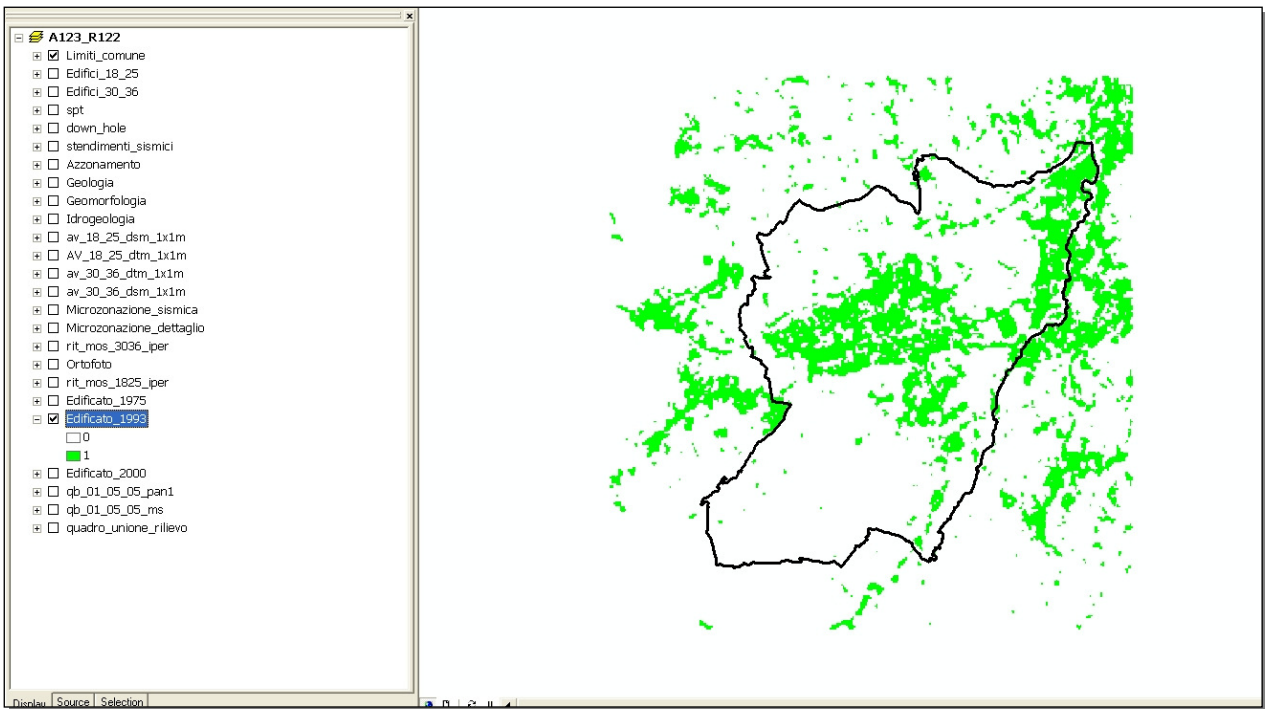
Figure 36. Built-up from 1993 Landsat TM image
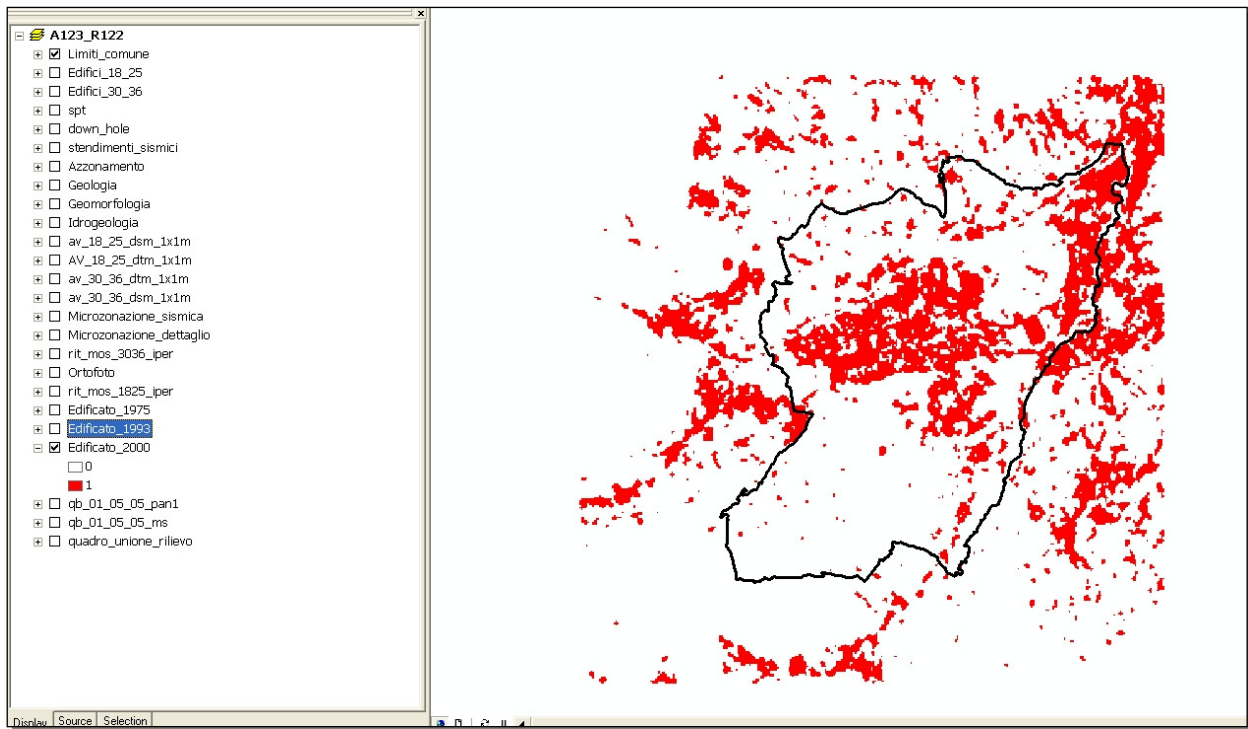
Figure 37. Built-up from 2000 Landsat ETM+ image
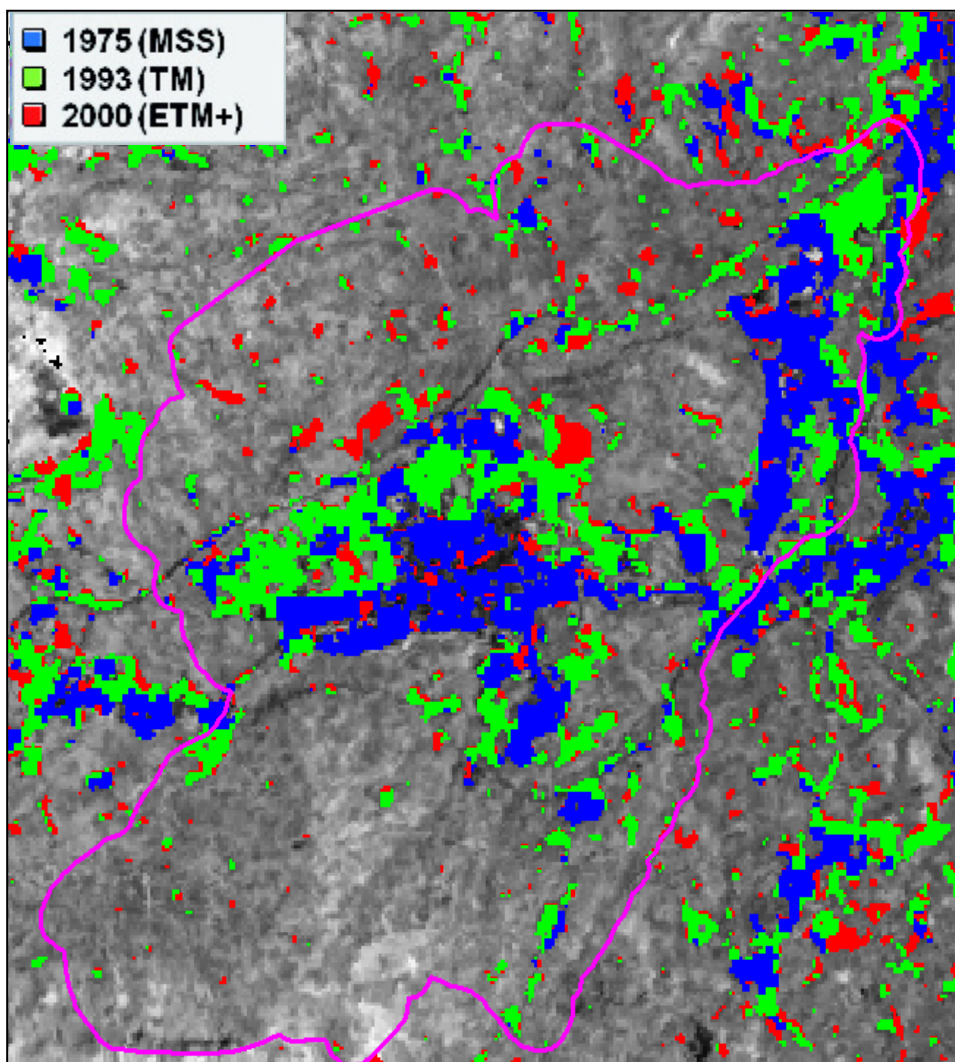
Figure 38. Avellino's Urban sprawl 1973-2000 (from Landsat images)
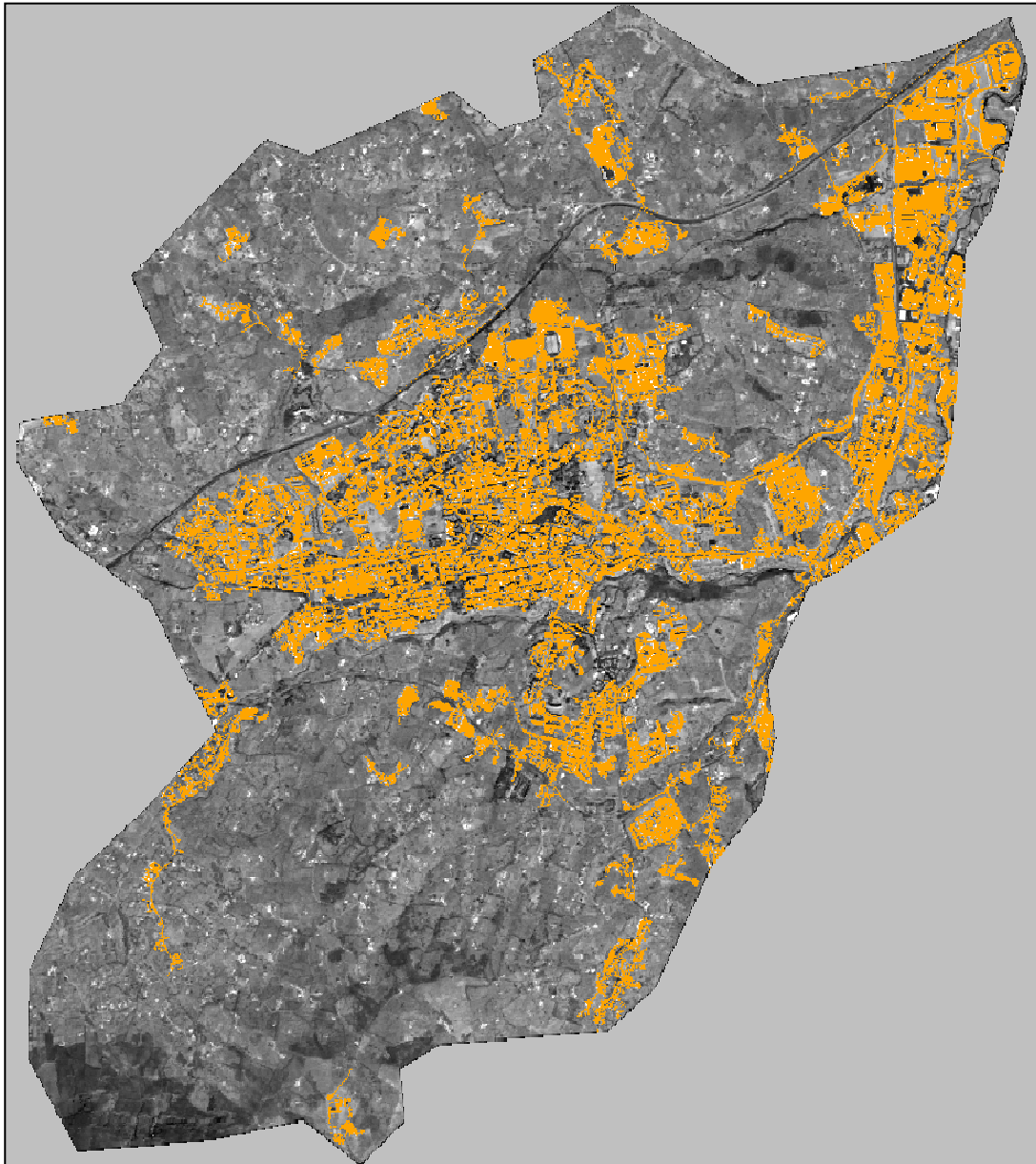
Figure 39. Avellino's built-up in 2006 from QuickBird data

2.3.3 Finding the construction material: ANN

Once obtained the geometrical (height, area, belonging to an agglomerate) data and assessed the consdtruction age, only the construction material has to find out in order to correctly assign the I_v to buildings, thus obtaining a Vulnerability Index Map.
For this kind of endeavour, Artificial Neural Networks were chosen, amongst other data mining techniques. In particular, Tiberius data mining software was used.

The input data were:

- Hyperpectral data from AISA Eagle (31 bands, mean and StDev)
- Geometrical parameters (Area, Perimeter, Height, Floors number, Roof Tipology)
- Construction time
- Census data from Italian Statistics Institute

Following is shown the logical schema adopted:
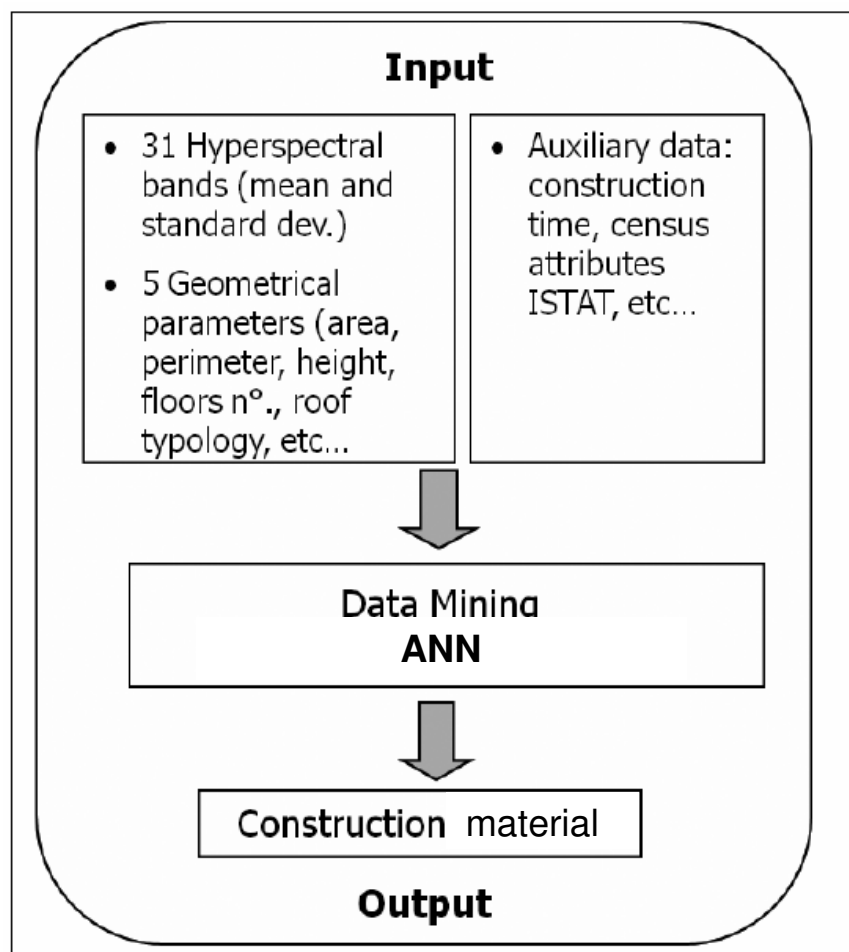
Artificial Neural Network were calibrated and validated through ground surveys data collection acquired at the same time of the LIDAR flight, according to the general schema reported in Figure x: 38 buildings for PC1 typology, 189 for RC2 and 6 for M6 (Test area San Tommaso district).

In table 3 is reported a sample of the data availables for each building (total: 233), except for the HSI data, showed in the following page:

ID	AREA	PERIMETER	EDIF	Height	Roof	MEAN_1	MEAN_DTM	floors	Tipology	tip_num
1	3092,81	242,60	188	10,42	Simple,Flat	345,267	334,843	3	PC1	2
2	2450,25	201,40	189	9,49	Simple,Flat	349,557	340,068	3	PC1	2
3	834,31	180,14	191	6,48	Simple,Flat	346,290	339,808	2	PC1	2
4	2176,94	187,87	196	11,44	Simple,Flat	351,504	340,063	4	PC1	2
5	916,25	123,30	197	6,87	Simple,Flat	339,075	332,201	2	PC1	2
6	344,88	76,75	198	11,74	Pitched	383,059	371,324	4	RC2	1
7	343,81	83,24	200	8,38	Pitched	366,428	358,049	3	RC2	1
8	315,94	86,42	201	8,34	Simple,Flat	344,663	336,319	3	PC1	2
9	3947,06	308,97	207	11,10	Multi-Level,Flat	347,334	336,230	4	PC1	2
10	117,88	60,88	209	6,78		378,635	371,859	2	RC2	1
11	1264,69	166,39	212	11,00	Simple,Flat	361,754	350,750	4	PC1	2
12	825,81	133,25	215	7,86	Simple,Flat	341,949	334,094	3	PC1	2
13	133,56	48,03	218	5,59	Pitched	355,681	350,092	2	PC1	2
14	1235,25	165,63	223	10,90	Simple,Flat	361,704	350,805	4	PC1	2
15	1594,25	164,36	228	14,10	Multi-Level,Flat	352,147	338,051	5	PC1	2
16	169,88	53,89	229	7,13	Pitched	385,205	378,073	2	RC2	1
17	361,31	104,07	230	10,34	Multi-Level,Flat	348,299	337,957	3	PC1	2
18	3297,94	260,11	231	8,00	Simple,Flat	341,326	333,323	3	PC1	2
19	174,63	62,64	232	9,96	Pitched	342,228	332,264	3	RC2	1
20	214,25	60,25	233	6,36	Pitched	339,770	333,412	2	RC2	1

Table 3. Sample Buildings data

In figure 40 are shown the mean spectral signatures of these three kind of buildings:
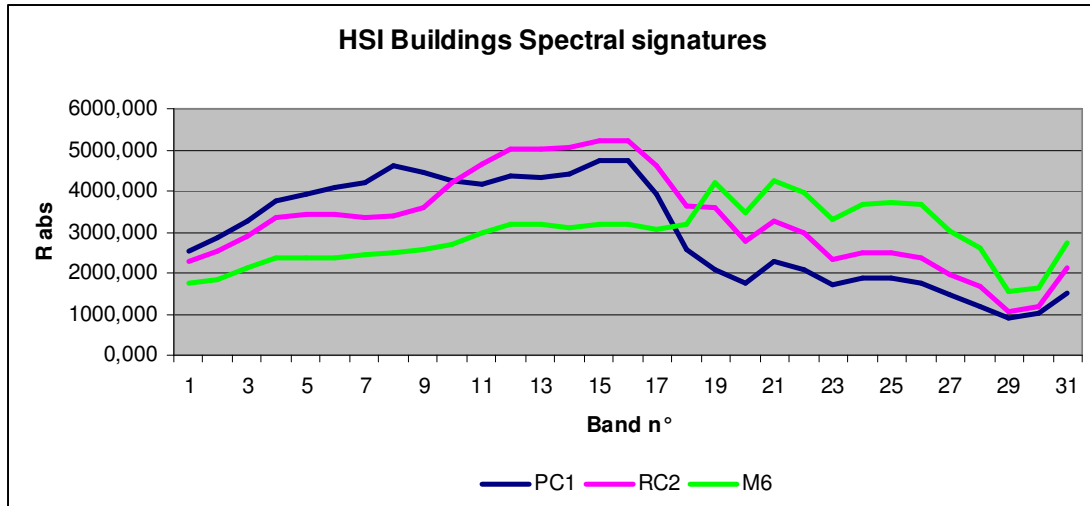
Figure 40. Sample buildings spectral signatures

As we can see there is a pretty good separation for all typologies, even if the relative values for PC1 and M6 inverts starting from Band 18 (721 nm, NIR region).

In figure 41 the Standard Deviations for each Band for the three same buildings are shown:
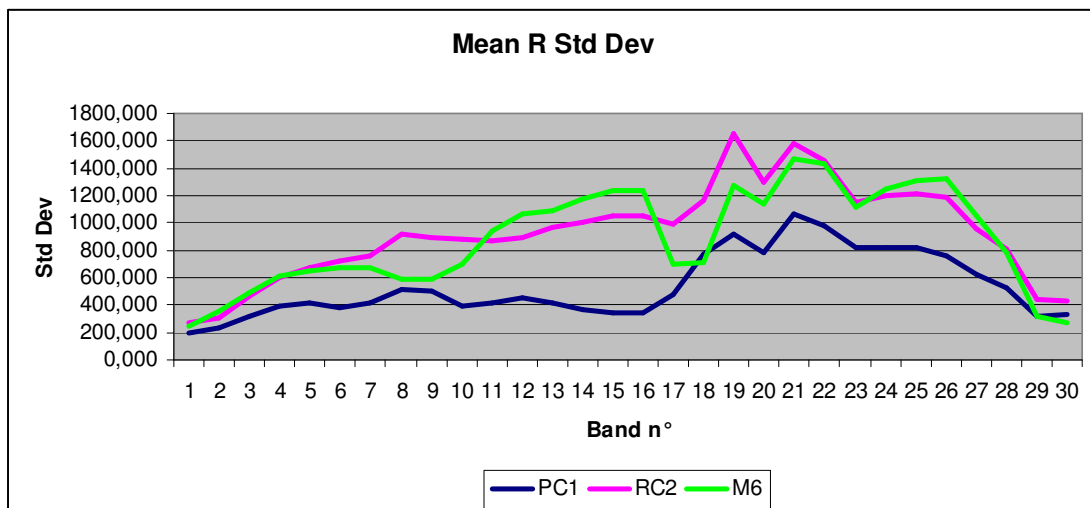
Figure 41. Sample buildings Reflectance Standard Deviations

In the Figure 42 is depicted the schema of the ANN network utilized [Brierley and Batty, 1999] with related accuracy matrix obtained for the in situ data-set.

In this case, 60 randomly selected occurrences of the in situ survey data were used for training, while the remaining provided the validation of the network.

Taking particular care to avoid overtraining, an accuracy greater than 85% was achieved.
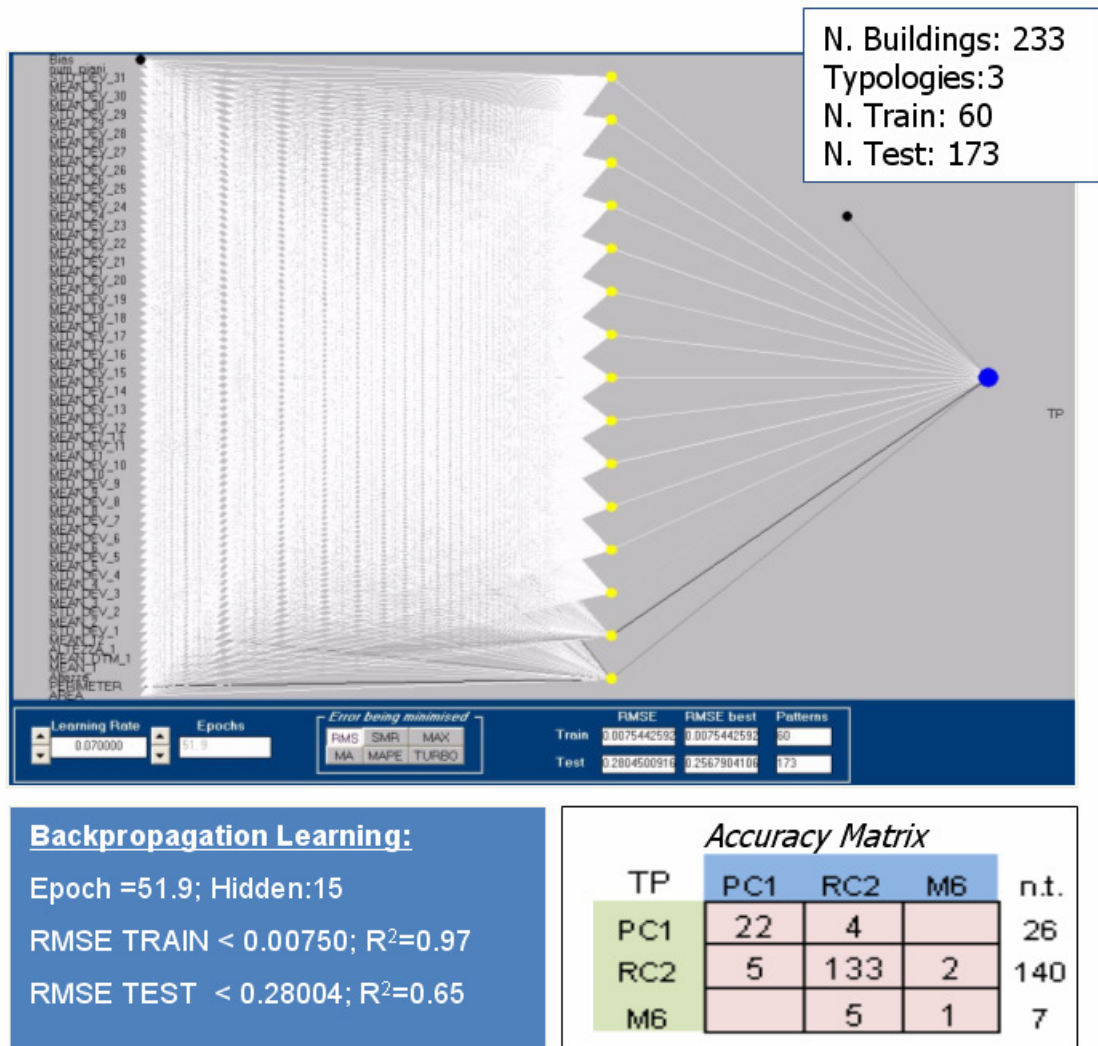
Figure 42. The ANN Network

Chapter 3 – Results and discussion

3.1 The Vulnerability Index Map

Finally, after gathering all the information needed, a Vulnerability Index Map can be drawn (Figure 43):
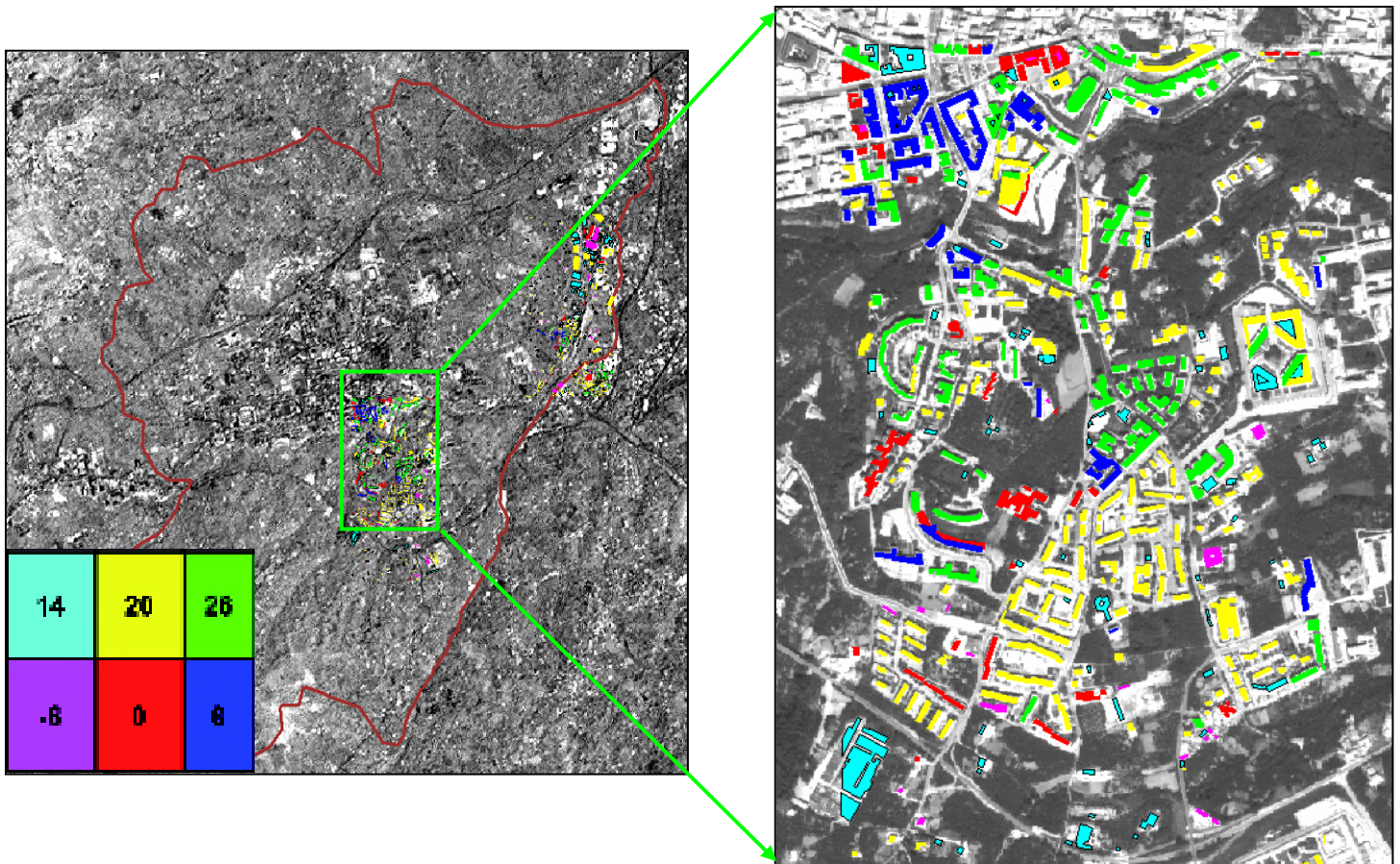
Figure 43: The Vunerability Index Map (Test Area)

3.2 Generalization of the test case

In order to evaluate the methodology here developed, a generalization of the case study was carried out. An higher number of buildings was gathered (1294, none of them previously utilyzed), picked up from other Avellino districts.

Then a new ANN was launched, with the parameters stated above.

In the following tables the results are shown, compared with the test case ones:

Test area: 233 buildings

48 PC1 <2000

172 RC2 >2000

13 Masonry

Train: 60

Test: 173

	PC1	RC2	M	TOT
PC1	22	4	0	26
RC2	5	133	2	140
M	0	6	1	7
%	85	95	14	

General.: 1294 buildings

776 PC1 <2000

264 RC2 > 2000

254 Masonry

Train: 400

Test: 894

	PC1	RC2	M	TOT
PC1	408	100	4	512
RC2	26	207	15	248
M	20	98	16	134
%	80	83	12	

Also in the general case incouraging result were achieved, even if with a slightly worst accuracy, especially with regard to RC2 typology buildings.

Figure 44 depict the generalyzed Vulnerability Index Map, showing I$_v$ ranging from -6 to 52

Figure 44. Vulnerability Index Map generalyzed

Furthermore, the question if there was some kind of data, amongst those availabled and utilyzed, that was of major importance in discriminating the buildings tipologies within the ANN network was taken into account.

Tiberius sw offer the opportunity to show the 10 most important input parameters ingested, and here's the result:

1.	Area		
2.	Floors Number		
3.	ST_DEV 24	NIR2	835,61nm
4.	Mean 7	GREEN	512,61nm
5.	Mean 18	NIR1	721,61nm
6.	Mean 8	GREEN	531,61nm
7.	Mean 5	BLUE	474,61nm
8.	Mean 19	NIR1	740,61nm
9.	Mean 1	BLUE	402,01nm
10.	Mean 13	RED	626,61nm

Table 4. First 10 data in order of importance

In Figure 45 a plot of those data is shown, calculated as follows: every plotted value is

a mean of each of all the accounted building tipologies, for the Generalized case.

ANN 10 most discriminating data

	Area	Piani	St_dev24	Mean7	Mean18	Mean8	Mean5	Mean19	Mean1	Mean13
PC1	2110	3	929	5490	3744	5490	5274	3945	3073	5753
RC2	272	4	1048	4310	4530	4557	4243	5298	2826	5749
M6	73	2	995	3177	3458	3494	3100	4403	2085	3896
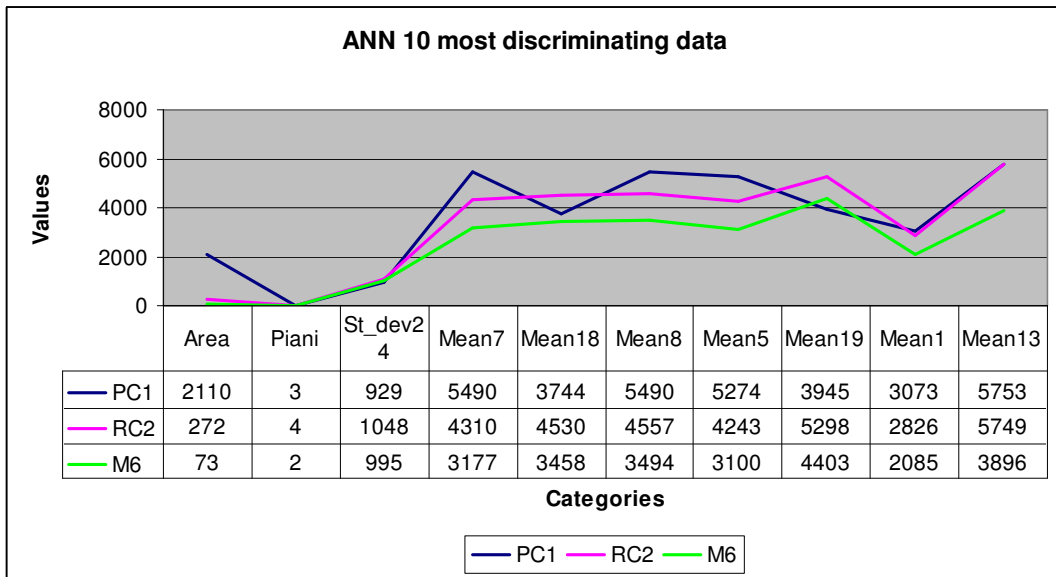
Figure 45. 10 most discriminating data plot

In the following Figure 46 the Mean, min and MAX Reflectance values for every

building tipology are shown.

Total R

	MEAN	min	MAX
M6	1914	1299	5609
PC1	2271	417	9056
RC2	2438	556	13425
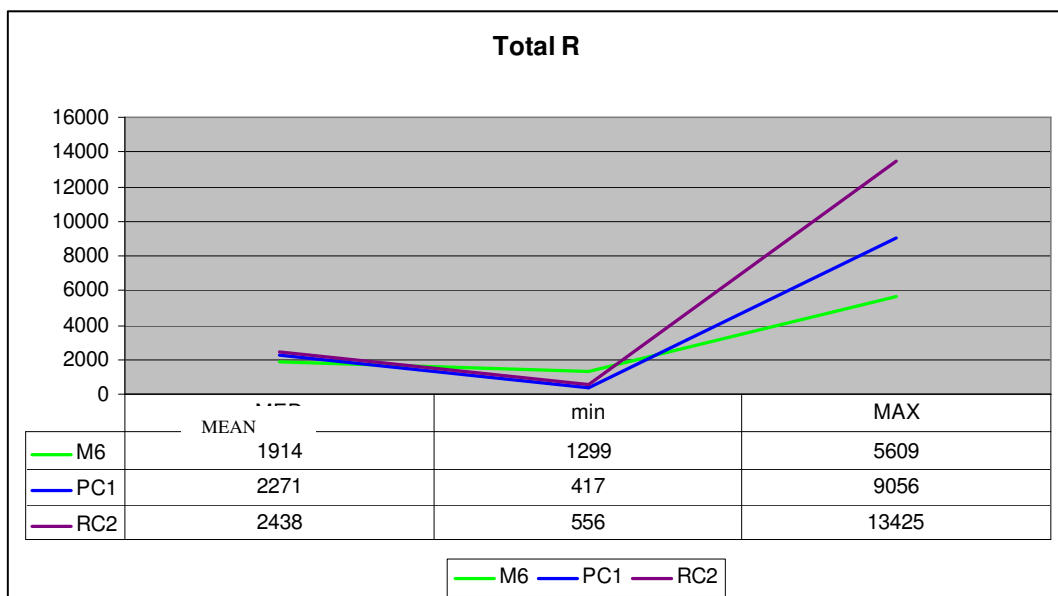
Figure 46. Mean, min and MAX R for HSI data

- The M6 min R value was in band 29 while the MAX was in band 21;

- the PC1 min Rvalue was in band 28 while the MAX was in band 12;

- the RC2 min R value was in band 29 while the MAX was in band 9.

In the following Figure 47, the mean PC1, RC2 and M6 reflectances (Test Area versus General Case) are shown:

Figure 47. Mean Reflectances General Case vs Test Area

3.3 Discussion

The ANN configured to estimate the buildings typologies in the test area, starting from the known in situ data of 233 buildings and making use of both the hyperspectral signatures and the previously estimated buildings geometric parameters, got an overall final accuracy of 68% (85% PC1, 95% RC2 and just 14% M6).

The ANN multilayer perceptron network was trained via back-propagation using a sample of 60 buildings data, while its validation has been carried out on the remaining 173 field data records.

Attention was paid to the learning phase tuning in order to avoid overtraining and consequent generality loss of the trained system.

With regard to the General Case, 1.233 building where taken into account; the training set counted 400 of them, driving to an overall accuracy of 58,3% (80% PC1, 83% RC2 and 12% M6).

A good agreement between Test Area and General Case is evident, the slight difference possibly due to the non correspondence shown in Band 15 reflectance (Fig. 47) and to the inverse proportion between PC1 and RC2 building typologies (48 vs 172 in TA and 776 vs 264 in GC).

Masonry typology had proved hard to discriminate with the proposed methodology, while PC1 and RC2 typologies seems to be more easy to correctly identify and separate.

With regard to discriminating data (Tab. 3), Area and Floors number constitute a valuable information, according with the differences shown in Tab 4.

Building Typ.	Mean Area, sqm	Mean Floors N°
PC1	440	5
RC2	431	6
M6	285	4

Table 5. Buildings mean areas and floors number

As for the Hyperspectral data, they show a good separation (See figure 47) for the three typologies in almost the whole spectral range 0.4-0.9 nm (except for Band 15, as already mentioned, in which PC1 and M6 shown no separation at all with regard for the whole area), and the most discriminating bands are equally distributed across the spectrum (two blue bands, two Green bands, one Red band and two InfraRed bands).

Finally, the Vulnerability Index Map for the General Case ranges from -6 for most recent, reinforced concrete-made buildings up to 52, for ancient masonry-made buildings.

In order to strenghten the results with regard to a better I_v determination, it could be advisable to design an enhanced metodology, taking into account other kinds of ancillary data also, like –but not limited to- seismic micro-zoning, geophisycal surveys, soil and subsoil geotechnical parameters and hydrogeological informations.

A future interesting research line, finally, could be to insert within the remote sensing phase also the exploitation of SAR data, unfortunately not in possession of the partners for the study area at the time of the research.

References

James D. Giglierano, Lidar Basics for Mapping Applications

Baltsavias, E.P., 1999, Airborne laser scanning: basic relations and formulas: SPRS Journal of Photogrammetry and Remote Sensing, no. 54, p. 199-214.

EXELIS Inc., An introduction to hyperspectral imaging technology. 2014

Adams, J. B., M. O. Smith, and P. E. Johnson. 1986. Spectral mixture modeling: a new analysis of rock and soil types at the Viking Lander 1 site. Journal of Geophysical Research 91, no. B8:8098-8112.

Adler-Golden, S., A. Berk, L. S. Bernstein, S. Richtsmeier, P. K. Acharya, M. W. Matthew, G. P. Anderson, C. L. Allred, L. S. Jeong, and J. H. Chetwynd. 1998. FLAASH, A MODTRAN 4 Atmospheric Correction Package for Hyperspectral Data

Retrievals and Simulations. Jet Propulsion Laboratory Publication 97-21.

Clark, R. N., G. A. Swayze, and A. J. Gallagher. 1993a. Mapping Minerals with Imaging Spectroscopy. Retrieved November 19, 2001, from http://speclab.cr.usgs.gov/PAPERS/cuprite.clark.93/mineral. map.html.

Clark, R. N., G. A. Swayze, A. J. Gallagher, T. V. V. King, and W. M. Clavin. 1993b. The U.S. Geological Survey, Digital Spectral Library: Version 1: 0.2 to 3.0 microns, U.S. Geological Survey Open File Report 93-592, 1340 pages, http://speclab.cr.usgs.gov.

Clark, R. N., G. A. Swayze, K. Heidebrecht, A. F. H. Goetz, and 224 Bibliography

R. O. Green. 1993c. Comparison of Methods for Calibrating AVIRIS Data to Ground Reflectance. Jet Propulsion Laboratory 93-26:35-36.

Clark, R. N., and G. A. Swayze. 1998. Imaging Spectroscopy Material Maps: Cuprite Introduction. Retrieved November 30, 2001, from http://speclab.cr.usgs.gov/map.intro.html.

Clark, R. N., G. A. Swayze, T. V. V. King, K. E. Livo, R. F. Kokaly, J. B. Dalton, J. S. Vance, B. W. Rockwell, and R. R. McDougal. 2000. Surface Reflectance Calibration of Terrestrial Imaging Spectroscopy Data: a Tutorial Using AVIRIS. Retrieved December 19, 2001, from http://speclab.cr.usus.gov/PAPERS.calibration.tutorial.

Crist, E. P., R. Laurin, and R. C. Cicone. 1986. Vegetation and Soils Information Contained in Transformed Thematic Mapper Data. Paper presented at International Geosciences and Remote Sensing Symposium (IGARSS)' 86 Symposium, ESA Publications Division, ESA SP-254.

Farrand, W. H., and J. C. Harsanyi. 1995. Discrimination of Poorly Exposed Lithologies in Imaging Spectrometer Data. Journal of Geophysical Research 100, no. E1:1565-1578.

Fraser, S. J., et al. 1986. "Targeting Epithermal Alteration and Gossans in Weathered and Vegetated Terrains Using Aircraft Scanners: Successful Australian Case Histories." Paper presented at the fifth Thematic Conference: Remote Sensing for Exploration Geology, Reno, Nevada.

Gao, B. C., K. B. Heidebrecht, and A. F. H. Geotz. 1996. Atmosphere Removal Program (ATREM) Users Guide Version 2.0. Centre for the Study of Earth from Space, Cooperative Institute for Research in Environmental Science. Boulder: University of Colorado.

Gao, B. C., A. F. H. Goetz, and W. J. Wiscombe. 1993. Cirrus Cloud Detection from Airborne Imaging Spectrometer Data using the 1.38 micron water vapor band. Geophysical Research Letters 20, no. 4:301-304.

Kruse, F. A. 1988. Use of Airborne Imaging Spectrometer Data to Map Minerals Associated with Hydrothermally Altered Rocks in the Northern Grapevine Mountains, Nevada. Remote Sensing of the Environment, 24:31-51.

Olsen, R. C., S. Bergman, and R. G. Resmini. 1997. Target detection in a forest environment using spectral imagery. SPIE 3118:46.

Ramsey, M.S., and P. R. Christensen. 1998. Mineral Abundance Determination: Quantitative Deconvolution of Thermal Emission Spectra. Journal of Geophysical Research 103, no. B1:577-596.

Richter, R. 1996. Atmospheric Correction of DAIS Hyperspectral Image Data, Paper read at SPIE AEROSENSE Conference, 8-12 April, at Orlando, FL. SPIE 2758.

Resmini, R. G., M. E. Kappus, W. S. Aldrich, J. C. Harsanyi, and M. Anderson. 1997. "Mineral Mapping with Hyperspectral Digital Imagery Collection Experiment (HYDICE) sensor data at Cuprite, Nevada, U.S.A.", International Journal of Remote

Sensing, 18 (7):1553-1570.

Sabins, F. F., Jr. 1987. Remote Sensing Principles and Interpretation. 2d ed. New York: W. H. Freeman & Co. Shipman, H., and J. Adams. 1987. Detectability of Minerals on Desert Alluvial Fans using Reflectance Spectra. Journal of Geophysical Research 92, no. B10:391-402.

AAVV, ERDAS IMAGINE Spectral Analysis™ User's Guide 15 October 2007

Adams, J.B., D.E. Sabol, V. Kapos, R.A. Filho, D.A. Roberts, M.O. mith, and A.R. Gillespie, 1995. Classification of multispectral mages based on fractions of endmembers: Application to land over change in the Brazilian Amazon, Remote Sensing of Environment,52:137–154.

Barnsley, M.J., and S.L. Barr, 1996. Inferring urban land use from atellite sensor images using kernel-based spatial reclassification, hotogrammetric Engineering & Remote Sensing, 62:949–958.

Barnsley, M.J., 1999. Digital remote sensing data and their characteristics, eographical Information Systems: Principles, Techniques, pplications, and Management (Second Edition) (P. Longley, M. oodchild, D.J. Maguire and D.W. Rhind, editors), John Wiley & ons, New York, N.Y., pp. 451–466.

Bateson, A., and B. Curtiss, 1996. A method for manual endmember election and spectral unmixing, emote Sensing of Environment, 5:229–243.

Boardman, J.W., 1993. Automated spectral unmixing of AVIRIS data sing convex geometry concepts, Summaries of the Fourth JPL irborne Geoscience Workshop, JPL Publication 93-26, NASA Jet

ropulsion Laboratory, Pasadena, Calif., pp. 11–14.

Boardman, J.W., and F.A. Kruse, 1994. Automated spectral analysis: A geological example using AVIRIS data, north Grapevine Mountains, Nevada, Proceedings, ERIM Tenth Thematic Conference on Geologic Remote Sensing, Ann Arbor, MI, pp. 407–418.

Boardman, J.M., F.A. Kruse, and R.O. Green, 1995. Mapping target signature via partial unmixing of AVIRIS data, Summaries of the Fifth JPL Airborne Earth Science Workshop, JPL Publication 95–1, NASA Jet Propulsion Laboratory, Pasadena, Calif., pp. 23–26.

Campbell, J.B., 2002. Introduction to Remote Sensing (3rd Edition), The Guilford Press, New York, N.Y., 621 p.

Cao, C., and N.S.N. Lam, 1997. Understanding the scale and resolution effects in remote sensing and GIS, Scale in Remote Sensing and GIS, (D.A. Quattrochi and M.F. Goodchild, editors), Lewis Publishers, Boca Raton, FL, pp. 57–72.

Chen, C.-M., G.F. Hepner, and R.R. Forster, 2003. Fusion of hyperspectral and radar data using the IHS transformation to enhance urban surface features, ISPRS Journal of Photogrammetry and Remote Sensing, 58:19–30.

Chen, S., S. Zheng, and C. Xie, 2000. Remote sensing and GIS for urban growth in China, Photogrammetric Engineering & Remote Sensing, 66:593–598.

Congalton, R.G., 1991. A review of assessing the accuracy of classifi- cation of remotely sensed data, Remote Sensing of Environment, 37:35–46.

Congalton, R.G., and R.A. Mead, 1983. A quantitative method to test for consistency and correctness in photo interpretation, Photogrammetric Engineering & Remote Sensing, 49:69–74.

Cracknell, A.P., 1998. Synergy in remote sensing—what's in a pixel? International Journal of Remote Sensing, 19:2025–2047.

Del Frate, Applications of Neural Networks to Remote Sensing, TOR VERGATA UNIVERSITY, DISP Dept, 2008

Del Frate F., Pacifici F., Schiavon G., and Solimini C., Use of Neural Networks for Automatic Classification From High-Resolution Images IEEE TRANSACTIONS ON GEOSCIENCE AND REMOTE SENSING, VOL. 45, NO. 4, APRIL 2007

Dengsheng Lu and Qihao Weng Spectral Mixture Analysis of the Urban Landscape in Indianapolis with Landsat ETM+ Imagery Photogrammetric Engineering & Remote Sensing Vol. 70, No. 9, September 2004, pp. 1053–1062.

ENVI, 2000. ENVI User's Guide. Research Systems Inc., Boulder, Colorado, 930 p.

Epstein, J., K. Payne, and E. Kramer, 2002. Techniques for mapping suburban sprawl, Photogrammetric Engineering & Remote Sensing, 63:913–918.

Fisher, P., 1997. The pixel: A snare and a delusion, International Journal of Remote Sensing, 18:679–685.

Foody, G.M., 2002. Status of land cover classification accuracy assessment, Remote Sensing of Environment, 80:185–201.

Gong, P., and P.J. Howarth, 1990. The use of structure information for improving land-cover classification accuracies at the rural-urban fringe, Photogrammetric Engineering & Remote Sensing, 56:67–73.

Gluch, R., 2002. Urban growth detection using texture analysis on merged Landsat TM and SPOT-P data, Photogrammetric Engineering & Remote Sensing, 68:1283–1288.

Green, A.A., M. Berman, P. Switzer, and M.D. Craig, 1988. A transformation for ordering multispectral data in terms of image quality with implications for noise removal, IEEE Transactions on Geoscience and Remote Sensing, 26:65–74.

Haack, B.N., E.K. Solomon, M.A. Bechdol, and N.D. Herold, 2002. Radar and optical data comparison/integration for urban delineation: A case study, Photogrammetric Engineering & Remote Sensing, 68:1289–1296.

Harris, P.M., and S.J. Ventura, 1995. The integration of geographic data with remotely sensed imagery to improve classification in an urban area, Photogrammetric Engineering & Remote Sensing, 61:993–998.

Hudson, W.D., and C.W. Ramm, 1987. Correct formulation of the Kappa coefficient of agreement, Photogrammetric Engineering & Remote Sensing, 53:421–422.

Hung, M., and M.K. Ridd, 2002. A subpixel classifier for urban landcover mapping based on a maximum-likelihood approach and expert system rules, Photogrammetric Engineering & Remote Sensing, 68:1173–1180.

Janssen, L.F.J., and F.J.M. van der Wel, 1994. Accuracy assessment of satellite derived land-cover data: A review, Photogrammetric Engineering & Remote Sensing, 60:419–426.

Jensen, J.R., 1996. Introductory Digital Image Processing: A Remote Sensing Perspective (2nd Edition), Prentice Hall, Upper Saddle River, New Jersey, 318 p.

Jensen, J.R., 2000. Remote Sensing of the Environment: An Earth Resource Perspective, Prentice Hall, Upper Saddle River, New Jersey, 544 p.

Kalkhan, M.A., R.M. Reich, and R.L. Czaplewski, 1997. Variance estimates and confidence intervals for the Kappa measure of classification accuracy, Canadian Journal of Remote Sensing, 23:210–216.

Lo, C.P., 1995. Automated population and dwelling unit estimation from high-resolution satellite images: A GIS approach, International Journal of Remote Sensing, 16:17–34.

Lo, C.P., D. Quattrochi, and J. Luvall, 1997. Application of highresolution thermal infrared remote sensing and GIS to assess the urban heat island effect, International Journal of Remote Sensing, 18:287–304.

Lu, D., M. Batistella, and E. Moran, 2002. Linear Spectral Mixture Analysis of TM Data for Land-use and Land-Cover Classification in Rondonia, Brazilian Amazon, Proceedings of the ISPRS Commission IV Symposium: Geospatial Theory, Processing and Applications, (C. Armenakis and Y.C. Lee, editors), Published by Center for Topographic Information Mapping Services Branch, Geomatics Canada, Department of Natural Resources Canada, Ottawa, Canada, pp. 557–562.

Lu, D., E. Moran, and M. Batistella, 2003. Linear mixture model applied to Amazonian vegetation classification, Remote Sensing of Environment, 87:456–469.

Madhavan, B.B., S. Kubo, N. Kurisaki, and T.V.L.N. Sivakumar, 2001. Appraising the anatomy and spatial growth of the Bangkok Metropolitan area using a vegetation-impervious-soil model through remote sensing, International Journal of Remote Sensing, 22:789–806.

Markham, B.L., and J.L. Barker, 1987. Thematic Mapper bandpass solar exoatmospheric irradiances, International Journal of Remote Sensing, 8:517–523.

Mesev, V., 1998. The use of census data in urban image classification, Photogrammetric Engineering & Remote Sensing, 64:431–438.

Myint, S.W., 2001. A robust texture analysis and classification approach for urban land-use and land-cover feature discrimination, Geocarto International, 16:27–38.

Okin, G.S., D.A. Roberts, B. Murray, and W.J. Okin, 2001. Practical limits on hyperspectral vegetation discrimination in arid and semiarid environments, Remote Sensing of Environment, 77: 212–225.

Painter, T.H., D.A. Roberts, R.O. Green, and J. Dozier, 1998. The effects of grain size on spectral mixture analysis of snow-covered area from AVIRIS data, Remote Sensing of Environment, 65: 320–332.

Phinn, S., M. Stanford, P. Scarth, A.T. Murray, and P.T. Shyy, 2002. Monitoring the composition of urban environments based on the vegetation-impervious surface-soil (VIS) model by subpixel analysis techniques, International Journal of Remote Sensing, 23:4131–4153.

Quarmby, N.A., J.R.G. Townshend, J.J. Settle, and K.H. White, 1992. Linear mixture modeling applied to AVHRR data for crop area estimation, International Journal of Remote Sensing, 13:415–425.

Quattrochi, D.A., J.C. Luvall, D.L. Rickman, M.G. Estes, C.A. Laymon, and B.F. Howell, 2000. A decision support information system for urban landscape management using thermal infrared data, Photogrammetric Engineering & Remote Sensing, 66:1195–1207.

Rashed, T., J.R. Weeks, M.S. Gadalla, and A.G. Hill, 2001. Revealing the anatomy of cities through spectral mixture analysis of multisepctral satellite imagery: A case study of the Greater Cairo region, Egypt, Geocarto International, 16:5–15.

Ridd, M.K., 1995. Exploring a V-I-S (Vegetation-Impervious Surface- Soil) model for urban ecosystem analysis through remote sensing: Comparative anatomy for cities, International Journal of Remote Sensing, 16:2165–2185.

Roberts, D.A., M.O. Smith, and J.B. Adams, 1993. Green vegetation, non-photosynthetic vegetation, and soils in AVIRIS data, Remote Sensing of Environment, 44:255–269.

Roberts, D.A., G.T. Batista, J.L.G. Pereira, E.K.Waller, and B.W. Nelson, 1998a. Change identification using multitemporal spectral mixture analysis: Applications in eastern Amazônia, Remote Sensing Change Detection: Environmental Monitoring Methods and Applications (R.S. Lunetta and C.D. Elvidge, editors), Ann Arbor Press, Ann Arbor, Mich., pp. 137–161.

Roberts, D.A., M. Gardner, R. Church, S. Ustin, G. Scheer, and R.O. Green, 1998b, Mapping chaparral in the Santa Monica mountains using multiple endmember spectral mixture models, Remote Sensing of Environment, 65:267–279.

Settle, J.J., and N.A. Drake, 1993. Linear mixing and the estimation of ground cover proportions, International Journal of Remote Sensing, 14:1159–1177.

Shaban, M.A., and O. Dikshit, 2001. Improvement of classification in urban areas by the use of textural features: The case study of Lucknow city, Uttar Pradesh, International Journal of Remote Sensing, 22:565–593.

Small, C., 2001. Estimation of urban vegetation abundance by spectral mixture analysis, International Journal of Remote Sensing, 22:1305–1334.

Small, C., 2002. Multitemporal analysis of urban reflectance, Remote Sensing of Environment, 81:427–442.

Smith, M.O., S.L. Ustin, J.B. Adams, and A.R. Gillespie, 1990. Vegetation in Deserts: I. A regional measure of abundance from multispectral images, Remote Sensing of Environment, 31:1–26.

Smits, P.C., S.G. Dellepiane, and R.A. Schowengerdt, 1999. Quality assessment of image classification algorithms for land-cover mapping: A review and a proposal for a cost-based approach, International Journal of Remote Sensing, 20:1461–1486.

Stefanov, W.L., M.S. Ramsey, and P.R. Christensen, 2001. Monitoring urban land cover change: An expert system approach to land cover classification of semiarid to arid urban centers, Remote Sensing of Environment, 77:173–185.

Strahler, A.H., C.E. Woodcock, and J.A. Smith, 1986. On the nature of models in remote sensing, Remote Sensing of Environment, 70:121–139.

Stuckens, J., P.R. Coppin, and M.E. Bauer, 2000. Integrating contextual information with per-pixel classification for improved land cover classification, Remote Sensing of Environment, 71:282–296.

Thomson, C.N., and P. Hardin, 2000. Remote sensing/GIS integration to identify potential low-income housing sites, Cities, 17:97–109.

Van der Meer, F., and S.M. de Jong, 2000. Improving the results of spectral unmixing of Landsat Thematic Mapper imagery by enhancing the orthogonality of end-members, International Journal of Remote Sensing, 21:2781–97.

Ward, D., S.R. Phinn, and A.L. Murray, 2000. Monitoring growth in rapidly urbanizing areas using remotely sensed data, Professional Geographer, 53:371–386.

Weng, Q., 2001. A remote sensing-GIS evaluation of urban expansion and its impact on surface temperature in the Zhujiang Delta, China, International Journal of Remote Sensing, 22:1999–2014.

Wu, C., and A.T. Murray, 2003. Estimating impervious surface distribution by spectral mixture analysis, Remote Sensing of Environment, 84:493–505.

Zha, Y., J. Gao, and S. Ni, 2003. Use of normalized difference built-up index in automatically mapping urban areas from TM imagery, International Journal of Remote Sensing, 24:583–594.

Zhang, J., and G.M. Foody, 2001. Fully-fuzzy supervised classification of sub-urban land cover from remotely sensed imagery: Statistical neural network approaches, International Journal of Remote Sensing, 22:615–628.

Zhang, Q., J. Wang, X. Peng, P. Gong, and P. Shi, 2002. Urban built-up land change detection with road density and spectral information from multitemporal Landsat TM data, International Journal of Remote Sensing, 23:3057–3078.

Zhu, G., and D.G. Blumberg, 2002. Classification using ASTER data and SVM algorithms: The case study of Beer Sheva, Israel, Remote Sensing of Environment, 80:233–240.

Annexes

Annex 1 Publications

I. *Flavio Borfecchia, Maurizio Pollino, Luigi De Cecco, Alessandro Lugari, Sandro Martini, Luigi La Porta, Elisabetta Ristoratore, Carmine Pascale Active and passive remote sensing for supporting the evaluation of the urban seismic vulnerability, Italian Journal of Remote Sensing, 2010, 42 (3):129-141 - ISSN 1129-8596*

II. *F. Borfecchia, A. B. Della Rocca, M. Pollino, A. Lugari, L. De Cecco, S. Martini, L. La Porta Active (LIDAR) and passive (multi/hyperspectral) remote sensing techniques for supporting the evaluation of the urban seismic vulnerability, Proceedings of the G4DM 2010 Conference, Turin, February 2010*

III. *Lugari, M. Pollino, F. Borfecchia, S. Martini, L. De Cecco, "Un SIT a supporto della protezione dell'ambiente costruito", proceedings of the 12th Italian ESRI User Conference, Rome, Italy, 27-29 May 2009*

IV. *F. Borfecchia, A. Lugari, M. Pollino, "Aerospatial remote sensing techniques to support seismic vulnerability assessment at urban level", Workshop "PRISMA: Verso le Applicazioni della missione iperspettrale nazionale", Centro di Geodesia Spaziale "G. Colombo", Matera, Italy, 31 March – April the 1st, 2009*

V. *F. Borfecchia, A. B. Della Rocca, M. Pollino, A. Lugari, L. De Cecco, S. Martini, L. La Porta "Tecniche aerospaziali attive e passive nella stima della vulnerabilità del tessuto urbano", proceedings of the 13th ASITA Conference, Bari, Italy, December 2009*

VI. *Flavio Borfecchia, Maurizio Pollino, Alessandro Lugari Progetto TELLUS STABILITA, "SPERIMENTAZIONE DI PRODOTTI E TECNICHE INNOVATIVE E SVILUPPO DI NUOVE METODOLOGIE PER LA PROTEZIONE DELL'AMBIENTE COSTRUITO CIVILE DAL DANNO LEGATO A SOLLECITAZIONI DINAMICHE AMBIENTALI E IN PARTICOLARE SISMICHE" Obiettivo Realizzativo OR1, Metodologie digitali per l'estrazione automatica dei parametri 3D degli edifici in aree urbane Attività A1.1 Progettazione generale del sistema, individuazione dell'area test e acquisizione delle immagini e delle informazioni territoriali Sotto-Attività A1.1.1 Studi teorici e stato dell'arte su metodologie digitali per l'estrazione automatica di parametri 3D di edifici in aree urbane Rapporto Tecnico Risultato R 1.1.1, Rapporto sullo stato dell'arte Stato dell'arte su tecnologie digitali di restituzione tridimensionale 31/10/07*

VII. *Flavio Borfecchia, Maurizio Pollino, Alessandro Lugari, Luigi De Cecco, Sandro Martini Progetto TELLUS STABILITA, "SPERIMENTAZIONE DI PRODOTTI E*

TECNICHE INNOVATIVE E SVILUPPO DI NUOVE METODOLOGIE PER LA PROTEZIONE DELL'AMBIENTE COSTRUITO CIVILE DAL DANNO LEGATO A SOLLECITAZIONI DINAMICHE AMBIENTALI E IN PARTICOLARE SISMICHE"
Obiettivo Realizzativo OR1, Metodologie digitali per l'estrazione automatica dei parametri 3D degli edifici in aree urbane
Sotto-Attività A1.1.2 Progettazione del rilievo e valutazione del suo livello di automatismo
Sotto-Attività A1.1.3 Ricerca di siti significativi su cui effettuare le sperimentazioni e reperimento diretto di tutto il relativo materiale informativo già esistente
Rapporto Tecnico Risultato R 1.1.2
Progettazione del rilievo e raccolta materiale informativo relativo al sito
31/10/07

VIII. *Flavio Borfecchia, Maurizio Pollino, Alessandro Lugari*
Progetto TELLUS STABILITA, "SPERIMENTAZIONE DI PRODOTTI E TECNICHE INNOVATIVE E SVILUPPO DI NUOVE METODOLOGIE PER LA PROTEZIONE DELL'AMBIENTE COSTRUITO CIVILE DAL DANNO LEGATO A SOLLECITAZIONI DINAMICHE AMBIENTALI E IN PARTICOLARE SISMICHE"
Obiettivo Realizzativo OR1, Metodologie digitali per l'estrazione automatica dei parametri 3D degli edifici in aree urbane
Attività A1.1 Progettazione generale del sistema, individuazione dell'area test e acquisizione delle immagini e delle informazioni territoriali
Sotto-Attività A1.1.4 Progettazione generale del sistema Rapporto Tecnico Risultato R 1.1.3 Definizione delle specifiche di massima del sistema
31/03/08

IX. *Flavio Borfecchia, Maurizio Pollino, Sandro Martini, Luigi De Cecco, Alessandro Lugari*
Progetto TELLUS STABILITA, "SPERIMENTAZIONE DI PRODOTTI E TECNICHE INNOVATIVE E SVILUPPO DI NUOVE METODOLOGIE PER LA PROTEZIONE DELL'AMBIENTE COSTRUITO CIVILE DAL DANNO LEGATO A SOLLECITAZIONI DINAMICHE AMBIENTALI E IN PARTICOLARE SISMICHE"
Obiettivo Realizzativo OR1 Metodologie digitali per l'estrazione automatica dei parametri 3D degli edifici in aree urbane
Attività A1.3 Zonizzazione delle aree urbane e tipizzazione degli edifici
Sotto-Attività A1.3.1 Sviluppo di algoritmi di image processing per l'estrazione di parametri territoriali
Rapporto Tecnico Risultato R 1.3.1 Procedure per l'estrazione di parametri territoriali
30/09/08

Annex 2 Mean buildings Geometric and Reflectance data

In the following pages the Buildings data values are shown, according with the legend below:

General Case Buildings: *GC*
Test Area Buildings: *TA*
Reinforced concrete before 2000: *PC1*
Reinforced concrete after 2000: *RC2*
Masonry: *M6*

- N° of edifices (*N° Edif*)

- Mean Area (*AREA*)

- min Area

- MAX Area

- N° of floors (*PIANI*)

- Structure Tipology (*TIP_STRUTT*)

- Mean Reflectance values for each of the 31 AISA Eagle Bands (*MEAN_1*, *MEAN_2*, ..., *MEAN_31*)

	N° Edif	AREA	Piani	TIP_STRUTT	MEAN_1	MEAN_2	MEAN_3	MEAN_4
Med	**776**	**440**	**5**	**PC1 GC**	**2028,5**	**2200,0**	**2539,4**	**2856,0**
min		35	1		767,3	813,1	886,7	946,8
MAX		2522	13		5684,3	7613,4	9466,3	11043,2
Med	**48**	**2110**	**3**	**PC1 TA**	**3072,7**	**3553,1**	**4333,4**	**5094,8**
min		92	2		2217,5	2422,7	2828,5	3299,0
MAX		10193	5		4516,5	5357,9	6786,0	8055,5
Med	**264**	**431**	**6**	**RC2 GC**	**1852,8**	**1993,0**	**2286,6**	**2559,6**
min		46	1		580,1	642,7	723,3	781,8
MAX		1353	15		6723.8	8378,4	10564.2	12754,6
Med	**172**	**262**	**4**	**RC2 TA**	**2825,0**	**3069,0**	**3604,3**	**4140,4**
min		28	1		1630,6	1678,0	1955,4	2185,4
MAX		1880	8		6593,0	8075,9	10103,6	12033,3
Med	**254**	**285**	**4**	**M6 GC**	**1966,0**	**2073,3**	**2352,7**	**2615,8**
min		28	1		748,0	790,2	882,4	951,6
MAX		1331	10		6620,0	8260,9	10226,4	11990,9
Med	**13**	**73**	**2**	**M6 TA**	**2084,6**	**2237,5**	**2661,2**	**3030,9**
min		47	1		1746,1	1842,1	2123,3	2367,9
MAX		131	3		2593,0	2837,2	3429,2	3969,0

MEAN_5	MEAN_6	MEAN_7	MEAN_8	MEAN_9	MEAN_10	MEAN_11	MEAN_12	MEAN_13
2905,5	**2907,9**	**2929,8**	**3134,2**	**3296,9**	**3483,5**	**3688,7**	**3917,4**	**3898,1**
912,5	885,3	891,5	924,6	953,8	954,9	939,0	945,3	900,1
11352,8	11253,1	11127,9	11505,9	11447,0	11158,5	10814,8	10768,8	10281,9
5274,5	**5297,9**	**5295,9**	**5489,6**	**5565,7**	**5657,7**	**5725,5**	**5897,9**	**5752,5**
3423,7	3412,5	3353,1	3262,3	3198,7	3391,1	3665,8	3813,6	3662,9
8375,8	8351,0	8327,7	8697,6	8912,1	8926,3	8866,2	9056,5	8800,0
2595,7	**2589,7**	**2603,7**	**2781,7**	**2915,4**	**3070,5**	**3254,5**	**3465,3**	**3451,8**
758,8	730,5	714,5	751,7	768,7	779,7	818,8	866,7	849,9
13419,3	13511,6	13512,5	14119,1	14230,0	14090.0	13839,2	13858,6	13459,5
4243,1	**4284,7**	**4335,0**	**4560,7**	**4779,6**	**5081,3**	**5420,3**	**5776,3**	**5754,5**
2165,2	2152,6	2162,8	2288,2	2328,6	2355,9	2327,1	2367,6	2216,5
12575,1	12657,1	12692,5	13282,2	13424,9	13407,9	13173,1	13294,3	12876,3
2649,4	**2652,7**	**2682,1**	**2893,3**	**3093,2**	**3339,5**	**3608,1**	**3884,3**	**3896,9**
917,2	878,0	882,5	944,5	925,9	910,6	907,2	914,9	866,9
12376,2	12209,3	11957,0	12316,6	12260,0	11990,5	11619,6	11611,1	11114,3
3099,7	**3096,6**	**3176,5**	**3345,3**	**3494,1**	**3623,3**	**3780,5**	**3927,8**	**3896,0**
2356,0	2291,8	2386,6	2485,6	2539,9	2566,6	2576,5	2621,0	2606,0
4154,9	4251,7	4395,0	4787,6	5011,1	5190,8	5308,6	5487,3	5391,6

MEAN_14	MEAN_15	MEAN_16	MEAN_17	MEAN_18	MEAN_19	MEAN_20	MEAN_21	MEAN_22
3876,6	**2028,5**	**3863,5**	**3871,5**	**3420,0**	**4158,4**	**3391,0**	**4126,4**	**3820,8**
865,3	767,3	812,3	811,0	722,3	886,0	721,5	841,4	782,8
9957,0	5684,3	9354,9	8830,0	7329,9	8439,0	6824,6	8369,6	7754,5
5715,3	**5805,4**	**5805,4**	**5031,2**	**3744,4**	**3945,4**	**3062,9**	**3606,9**	**3311,8**
3609,0	3655,2	3655,2	2212,3	673,6	660,5	516,5	551,2	527,9
8644,8	8717,6	8717,6	8229,1	6775,9	8230,7	6791,1	8340,6	7704,3
3435,2	**1852,8**	**3432,1**	**3462,7**	**3091,3**	**3793,7**	**3105,3**	**3783,6**	**3508,2**
831,7	580,1	812,4	769,4	657,3	775,4	628,8	749,6	693,3
13188,4	6723,8	12683,8	12205,6	10202,0	11881,9	9376,0	11240,4	10247,6
5762,4	**5906,9**	**5906,9**	**5568,8**	**4563,6**	**5313,2**	**4287,3**	**5221,3**	**4836,5**
2161,3	2208,3	2208,3	2050,5	1229,0	1019,2	770,8	935,7	889,5
12590,7	12653,2	12653,2	11592,1	9469,3	10659,6	8391,1	10053,7	9207,9
3898,2	**1966,0**	**3934,1**	**3982,7**	**3555,6**	**4344,6**	**3556,4**	**4338,6**	**4027,2**
826,2	748,0	761,2	730,5	626,3	746,2	607,0	724,1	672,3
10714,6	6620,0	10114,7	9570,7	7928,3	9018,4	7089,5	8483,6	7876,6
3853,5	**3907,8**	**3907,8**	**3765,4**	**3457,9**	**4402,9**	**3620,2**	**4418,4**	**4140,1**
2569,8	2601,2	2601,2	2665,3	2600,3	3387,8	2803,7	3447,3	3296,3
5323,6	5385,1	5385,1	5353,8	4510,9	5542,9	4560,6	5608,7	5242,6

MEAN_23	MEAN_24	MEAN_25	MEAN_26	MEAN_27	MEAN_28	MEAN_29	MEAN_30	MEAN_31
3109,1	**3436,8**	**3492,2**	**3469,5**	**2833,7**	**2382,8**	**1386,9**	**1434,8**	**2484,8**
666,4	740,0	750,2	745,1	638,6	578,0	374,2	404,8	659,6
6272,8	6870,2	6939,8	6853,9	5574,8	4643,5	2614,3	2637,4	4826,4
2687,3	**2976,7**	**3006,6**	**2983,1**	**2493,8**	**2163,9**	**1467,8**	**1587,0**	**2516,0**
467,0	444,9	434,2	519,1	442,6	417,2	468,2	605,5	707,3
6253,6	6927,2	7037,0	6975,0	5634,9	4610,1	2485,6	2461,4	4434,6
2860,4	**3167,1**	**3222,0**	**3203,7**	**2620,1**	**2206,3**	**1290,2**	**1336,4**	**2307,7**
577,6	644,7	662,3	653,7	551,3	484,1	350,3	367,5	595,9
8181,4	9017,3	9153,3	9170,1	7472,6	6276,2	3300,9	3382,2	6254,5
3942,0	**4370,7**	**4447,3**	**4424,4**	**3626,9**	**3043,8**	**1787,5**	**1842,1**	**3221,1**
622,7	856,4	873,1	808,1	686,1	703,6	555,7	674,5	908,0
7353,5	8108,5	8160,3	8018,3	6414,2	5220,7	2850,6	2857,2	5344,7
3286,1	**3633,1**	**3694,6**	**3674,4**	**3009,2**	**2537,1**	**1480,2**	**1532,3**	**2661,9**
568,0	633,5	652,3	641,4	546,4	494,5	399,8	438,4	611,9
6382,5	7004,3	7102,1	7035,8	5710,8	4758,0	2650,1	2668,3	4761,0
3402,4	**3780,7**	**3818,4**	**3812,8**	**3120,4**	**2628,0**	**1543,8**	**1585,3**	**2742,7**
2756,3	3029,8	2959,7	2936,1	2394,8	2075,3	1299,3	1420,6	2373,8
4276,4	4804,5	4896,4	4910,9	4011,1	3325,2	1847,7	1825,7	3315,4